2013

Three-phase Contact Line Phenomena In Droplets On Solid And Liquid Surfaces: Electrocapillary, Pinning, Wetting Line Velocity Effect, And Free Liquid Surface Deformation

Roxana Shabani
University of Central Florida

THREE-PHASE CONTACT LINE PHENOMENA IN DROPLETS ON SOLID AND LIQUID SURFACES: ELECTROCAPILLARY, PINNING, WETTING LINE VELOCITY EFFECT, AND FREE LIQUID SURFACE DEFORMATION

by

ROXANA SHABANI

B.S. University of Tehran, 2007
M.Sc. University of Central Florida, 2011

A dissertation submitted in partial fulfillment of the requirements
for the degree of Doctor of Philosophy
in the Department of Mechanical and Aerospace Engineering
in the College of Engineering and Computer Science
at the University of Central Florida
Orlando, Florida

Summer Term
2013

Major Professor: Hyoung Jin Cho

ABSTRACT

In this dissertation physical phenomena relevant to (i) an interface formed between two fluids and a solid phase (wetting line) and (ii) an interface between three fluids (triple contact line) were investigated. In the former case, the wetting line (WL) phenomena which encompass the wetting line energy (WLE) or pinning, the wetting line velocity (WLV), and the contact angle hysteresis, were studied using a micropump based on electrowetting on dielectric (EWOD). In the latter case, the interfacial phenomena such as the air film lubrication effect and the liquid free surface deformation were taken into account to explain the dual equilibrium states of water droplets on liquid free surfaces.

EWOD was implemented to devise a pumping method for a continuous flow in a microchannel. An active micropump with a simple layout and no moving parts is designed and fabricated which has on demand flow on/off capability. The micropump is based on droplet/meniscus pressure gradient generated by EWOD. By altering the contact angle between liquid and solid using an electric field a pressure gradient was induced and a small droplet was pumped into the channel via a uniform flow rate. A surface tension based propellant method was introduced as a low power consumption actuation method in microfluidic devices. For an initial droplet volume of 0.3μL and a power of 12nW a constant flow rate of 0.02μL/sec was demonstrated. Sample loading on-demand could be achieved by regulating an electric potential. Unexpectedly, the flow rate of the pump was found to be constant in spite of the changes in the droplet's radius, which directly affects the pump's driving pressure.

The WL phenomena were studied in details to unravel the physical concept behind the micropump constant flow rate during the operation. An interesting observation was that the shrinking input droplet changes its shape in two modes in time sequence: (i) in the first mode its contact angle decreases while its wetting area remains constant due to the pinning, (ii) in the second mode the droplet's WL starts to move while its contact angle changes as a function of its velocity. Contact angles were measured for the droplet advancing and receding WLs at different velocities to capture a full picture of contact angle behavior due to pinning and WLV effects. These results are also relevant to the meniscus inside the channel. The changes on the contact angle caused by the presence of EWOD at the bottom of the channel were studied in detail.

The EWOD based micropump was used as a platform to study the contribution of the pinning and WLV effects on its constant flow rate. The effects of the WLE on the static contact angle and the WLV on the dynamic contact angle in the pump operation were investigated. Also the effect of EWOD voltage on the magnitude and uniformity of the micropump flow rate was studied.

Dynamic contact angles (as a function of pinning and WLV) were used to accurately calculate the pressure gradient between the droplet and the meniscus and estimate the flow rate. It was shown that neglecting either of these effects not only results in a considerable gap between the predicted and the measured flow rates but also in an unphysical instability in the flow rate analysis. However, when the WLE and WLV effects were fully taken into account, an excellent agreement between the predicted and the measured flow rates was obtained.

For the study of the TCL between three fluids, aqueous droplets were formed at oil-air interface and two stable configurations of (i) non-coalescent droplet and (ii) cap/bead droplet were observed. General solutions for energy and force analysis were obtained and were shown to be in good agreement with the experimental observations. Further the energy barrier obtained for transition from configuration (i) to (ii), was correlated to the droplet release height and the probability of non-coalescent droplet formation. Droplets formed on the solid surfaces and on the free surface of immiscible liquids have various applications in droplet-based microfluidic devices. This research provides an insight into their formation and manipulation.

To my husband, Farzad.

ACKNOWLEDGMENTS

I would like to thank my supervisor and mentor, Prof. Hyoung Jin Cho for his unwavering support and insightful guidance throughout my endeavor as a PhD candidate, and for giving me numerous research opportunities that have allowed me to achieve my goals as a researcher. His enthusiasm and hard work, and his honest pursuit of scientific knowledge, have set a great example for me as a successful scientist. I feel lucky to be among his students and I am hopeful that our scientific collaborations will be continued in my entire professional carrier, in the same way that I am confident our friendship will be lasting through my personal life.

I want to also thank my lab members, Dr. Ganashyam Londe, Dr. Peng Zhang, Dr. Ehsan Yakhshi-Tafti, Dr, In-Sung Hwang, Dr. Sanghoon Park, Andrea Wesser, David Summerlot, and H. M. Iftekhar Jaim for continuous scientific discussions and collaborations and above all for their life lasting friendship. Thanks also to our collaborators, Prof. Ranganathan Kumar and Prof. Jong-Hyun Ahn, for providing me with their support and scientific insight.

Thanks also to my committee members Prof. Ranganathan Kumar, Prof. Jayanta Kapat, Prof. Louis Chow, and Prof. Lei Zhai, for taking time to evaluate my work and for their constructive comments and discussions.

Special thanks to my husband and my best friend Farzad, who has been a great source of hope, joy and support, without whom this work would not have been accomplished.

Some of the materials used in this dissertation are previously published by The Royal Society of Chemistry, Elsevier, Springer and American Institute of Physics, in the format of journal articles in which I have been the first author.

TABLE OF CONTENTS

LIST OF FIGURES

LIST OF TABLES

LIST OF ACRONYMS

EW	Electrowetting
EWOD	Electrowetting on dielectric
PDMS	Polydimethylsiloxane
SOG	Spin-on glass
WL	Wetting line
WLE	Wetting line energy
WLV	Wetting line velocity

CHAPTER 1: INTRODUCTION

Micropumps and microvalves are the key components in handling small amount of aqueous samples [1-3]. Their importance is recognized, especially, in the field of analytical chemistry, biology and medicine in which massive and parallel screening of aliquots with the limited amount of usable samples is to be performed or a limited amount of dose needs to be supplied with good accuracy. In such applications, small amounts of biological samples or chemical reagents are introduced and transferred by means of micropumps and microvalves, followed by chemical reactions and biochemical processes such as immobilization, labeling and detection [4, 5]. Micropumps have been categorized by means of actuation methods applied to drive the flow rate. The electrostatic, piezoelectric, bimetallic, electroosmotic and electrowetting (EW) actuation methods have been reported [6].

The performance characteristics of micropumps for biological and chemical applications depend on critical parameters such as power consumption, flow rate, biocompatibility, disposability and durability of mechanical moving parts. Micropumps consisting of moving parts such as mechanical valves and membranes for controlling or actuating the liquid may be prone to mechanical failure, and their complicated structure often results in prohibitive fabrication cost [7]. Micropumps with low fabrication cost and minimal mechanical complexity are highly desirable for designing disposable biochips which could be easily replaced once the sample analysis is completed [8]. Therefore design and fabrication methods of micropumps with no moving parts are one of the central points of research in the field.

Among various actuation techniques, the surface tension-driven method was shown to be well suited for droplet based transport devices due to its favorable scaling effect [8-10]. The surface tension force is linearly proportional to the length of the interfacial line between the liquid, air and the solid (WL) in which a droplet forms the boundaries of the wetting area on the solid surface. By scaling down the size of the system homogenously, the surface to volume ratio of the system increases and the surface forces which are negligible on macroscale become dominant on the microscale.

Although passive surface tension based micropumps are shown to be suitable for many applications [8, 9], the ability to control the surface wettability to induce and stop the flow on demand would be highly desirable. The control of surface tension, by a temperature gradient in thermocapillary and by an electric potential gradient in electrocapillary, is implemented for micropumping [2, 3]. However, electrocapillary in the forms of EW and EWOD are considered more power efficient than the thermocapillary [4]. EWOD is the most promising method due to the electrochemical inertness of the substrate and the ability to work with the non-electrolyte aqueous solutions. In EWOD phenomenon, the wetting properties of a hydrophobic surface could be modified by applying an electric field without changing the chemical composition of the surface.

The simplest EWOD comprises a water droplet resting on a conducting layer covered with an dielectric layer (Fig. 1). A water droplet resting on a solid surface has a contact angle, θ_D which is defined clockwise, inside the liquid phase, from the solid surface to the tangent line to the liquid at the point of the contact with solid. θ_D depends on the surface tensions of the three phases of liquid, air, and solid and is equal to Young's equilibrium contact angle. By applying the voltage between the liquid and the

conductor of the EWOD substrate, an electrical double layer is formed at the liquid-substrate interface. The EWOD substrate which is in contact with the liquid, works similar to a capacitor. The fringing electric field, at the edge of the double layer, is formed at the substrate-liquid-air interface. The electric force parallel component to the surface, F_E, pulls the double layer forward. This helps liquid to wet the surface and move forward and therefore θ_D is reduced.

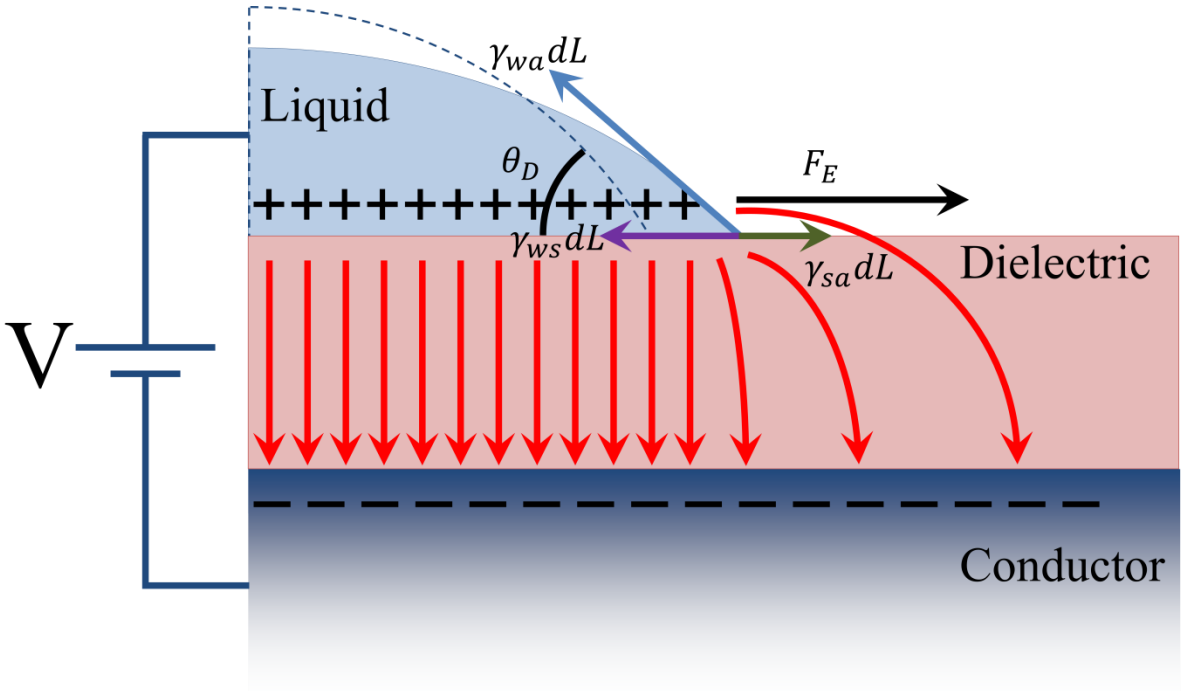

Fig. 1 Electrowetting on dielectric (EWOD): a voltage is applied between the water droplet and the conductor of the EWOD substrate. An electrical bi-layer is formed which generates a fringing electric field at the interface of liquid-air and solid surface. The electric force parallel component to the surface, F_E, pulls the liquid forward, reducing θ_D. The surface tension forces at the three-phase interface are shown.

Although EW and EWOD have been actively studied for a discrete droplet manipulation [11-14], to our knowledge an active micropump for continuous flows which takes advantage of EWOD was first reported in this research. The alteration of

wettability as a propellant method could be combined with a valve to form a pump. However, the design and fabrication of a valve that could work with the actuating method and form a complete device remains challenging [1, 15]. Most of the developed active electrical microvalves are driven by mechanical actuators [16]. In the proposed micropump in chapter 2, the flow could be turned on and off by switching the voltage on and off. On contrary to the previous works which used active mechanical microvalves for pumping, the EWOD based micropump does not require any moving parts and is driven purely based on wettability of the surface which is altered by the electric potential. The micropump's design and performance are discussed in chapter 2.

The biocompatibility imposes a limit on the type of the liquids which could be used for actuation in biomedical devices or induced chemical reactions. Although secondary transport liquid has been suggested as a solution for pumping water based solutions [16], the prevention of two liquids from mixing has remained an issue. Using the proposed micropump in chapter 2, aqueous solutions can be driven without using any electrolyte or secondary medium.

In devices that are designed based on EWOD, a liquid meniscus is manipulated by an applied voltage which reduces the contact angle of the wetting line (WL) formed at the boundary between the liquid, air, and the solid surface. Chapter 3 is dedicated to the study of the complex nature of the behavior of the moving WL due to the WL pinning and WL velocity effects. These two effects alter the liquid contact angle on the solid surface from its equilibrium value obtained from Young's equation (Fig. 2a) [24, 25]. The WLE effect or pinning effect, is a result of the local microscopic defects on the solid surface [26], by which liquid is pinned to the surface. Therefore, different values for

contact angle are expected depending on whether the WL is in advancing or receding modes (Fig. 2b). This effect could be shown on a slightly tilted surface. The WL on the lower side of the droplet is forced to advance, but the droplet adjusts its contact angles to the advancing contact angle, θ_A, to resist motion. However the WL on the upper side of the droplet is forced to recede, but θ_D is reduced to a receding contact angle θ_R before the WL start to move. The droplet WL remains pinned to the substrate. This is in agreement with our daily observations of rain droplets on a tilted surface such as the car windshield. The contact angle is also changed when the WL is moving, depending on the magnitude and direction of the WL velocity (Fig. 2c) [27, 28]. The droplet will eventually slide down the surface, if the surface is further tilted. θ_A is further increased and θ_R is more decreased as the magnitude of the WL velocity, U, increases. Further the EWOD voltage effect on the WL pinning and the contact angle hysteresis is studied.

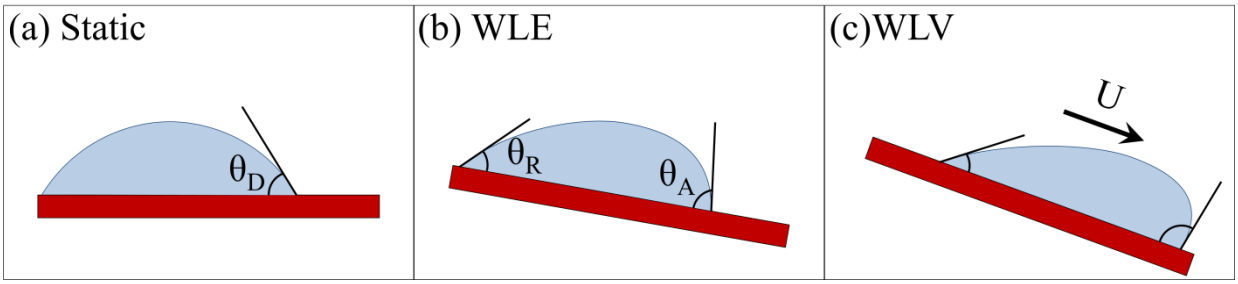

Fig. 2 WLE and WLV effects on Young's equilibrium droplet contact angle (a) A droplet resting on a horizontal surface has a static θ_D (b) Droplet adjusts its contact angles depending on the advancing or receding modes of WLs, θ_A and θ_R respectively, as the surface is slightly tilted. Droplet resists motion and its WL is pinned to the substrate (c) Droplet WL starts to move on the surface as it is further tilted. θ_A and θ_R are further changed as a function of droplet WL velocity, U.

Walker et al. reported that considering the effect of the WLE on contact angle is crucial to predicting the time scale of the liquid motion; otherwise the calculated flow

rate will be much higher than the experiments [29]. Dussan V. reported the relationship between dynamic contact angle and WL velocity in a forced wetting [27]. In chapter 4, the WLE effect on static contact angle and the WL velocity effect on dynamic contact angle in two different phases of the micropump operation are demonstrated for the first time.

In devices that are designed based on EWOD, a liquid meniscus is manipulated by an applied voltage which reduces the contact angle of the WL formed at the boundary between the liquid, air, and the solid surface. Theoretical and numerical models have been developed to describe the moving WL [30-33]. In devices based on EWOD the problem is more complicated due to the saturation of contact angle at higher voltages [34, 35]. The study of the moving WL in EW based devices, for discrete droplet manipulation, has also been the focus of many studies [12, 29, 36-46]. It has been shown that consideration of the pinning effect is essential to predict the accurate time scale of the droplet motion [29, 39]. The dynamics of the WL was also investigated to model the droplet motion on the electrodes [12, 42-44, 47, 48].

In chapter 5, a combined theoretical/experimental approach based on continuity and energy equations is developed to study a continuous flow induced by manipulating a meniscus on an EWOD substrate at the bottom of a microchannel. The WL pinning and the WL velocity effects need to be taken into account to describe the dynamic contact angles at the WLs: (i) the droplet's receding WL, (ii) the advancing WLs of the liquid meniscus on the upper and side walls of the channel, and (iii) the advancing WL at the bottom of the channel with a reduced contact angle due to EWOD. These two effects are crucial to developing a physically-relevant model for the flow rate analysis.

This is due to the fact that the accurate estimation of the contact angles is necessary to calculate the induced droplet/meniscus pressure gradient [37], and subsequently the micropump's flow rate.

The last chapter of this dissertation (chapter 6) investigates the important physical phenomena at the interface between three fluids. The similarities and the differences between the two setups used in the previous chapters and chapter 6 are tabulated in Table 1.

Table 1 Dynamics of three-phase interfaces and related physical phenomena

Phases	**Air, Water, Solid**	**Air, Water, oil**
3-phase Interface	Wetting line (WL)	Triple contact line (TCL)
Studied phenomena	Wetting line energy (pinning), Wetting line velocity effect	Air film lubrication effect, Free surface deformation
Actuation method	Electrocapillary (EWOD)	Thermocapillary convection
Substrate phase properties	Insulating, Hydrophobic	Low surface tension, High density

In chapters 3 to 5, the important wetting phenomena at a droplet moving WL on solid surface and a meniscus in a microchannel were investigated (Fig. 1 a, b). In chapter 6 two different interfaces between three fluids are studied and the relevant physical phenomena are described (Fig. 1 c, d). Further the stable equilibrium states of the floating droplets at the oil-air interface were predicted using energy analysis.

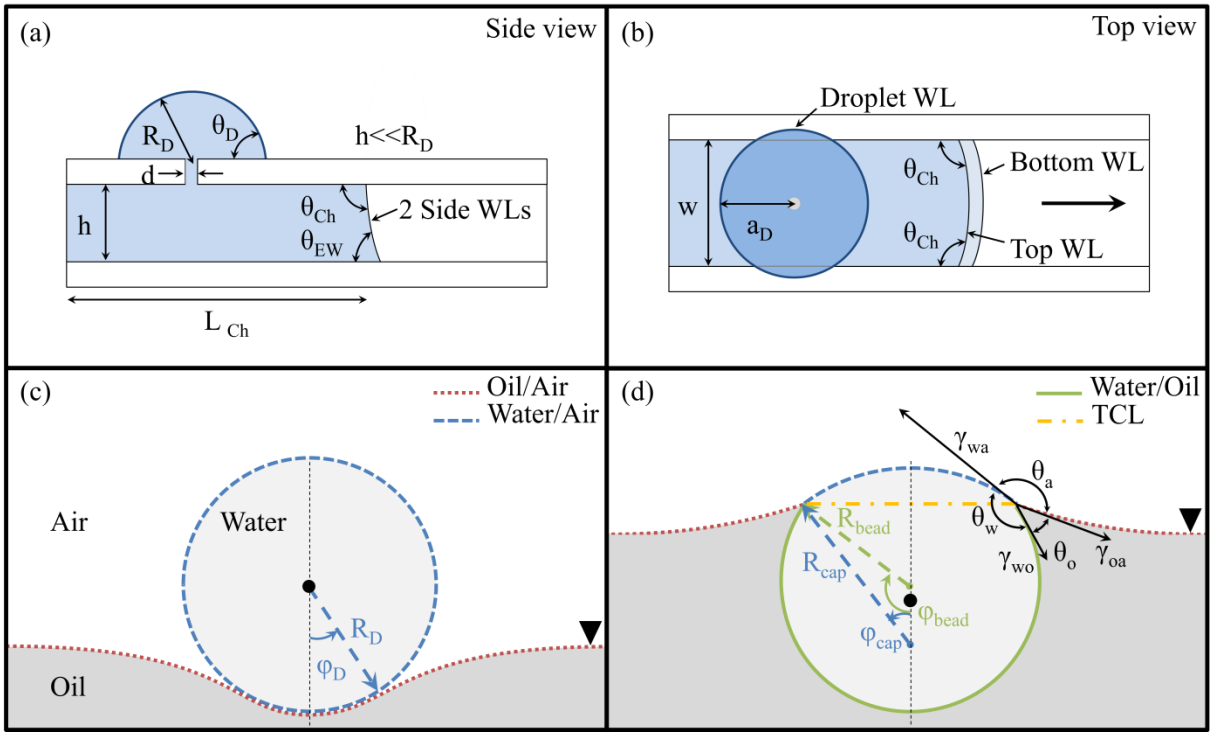

Fig. 3 Interfaces between three phases: (a, b) WLs formed between a solid and two fluids: a water droplet on PDMS surface and a meniscus in a microchannel. (c, d) floating water droplets on oil: Non-coalescent droplet and cap/bead droplet with a triple contact line (TCL).

The formation of floating aqueous droplets on the free surface of immiscible liquids has application in digital microfluidic devices [49], as well as material transportation and mixing in lab on a chip [50, 51]. The floating aqueous droplets serve as containers for encapsulating reagents in biochemical reactions [52]. They allow low consumption of the analytes and give direct access to reaction products [52]. The direct contact with the ambient air could be a benefit in sensor applications [53]. Moreover no material transfer between them and the liquid platform [54], results in reduced contamination compared to the solid counterparts. The sample evaporation could be reduced by encapsulating the device as well [53]. In such devices, thermocapillary was used for manipulating the floating droplets [50]. The floating non-coalescent (NC) water droplets were first

observed by Reynolds on the water's free surface [55]. Mahajan investigated the effect of the surrounding medium on the life of the floating droplets [56]. The droplet's non-coalescence caused by a surface tension gradient due to a temperature difference between the droplet and the pool liquid [51], a vertical oscillation of base liquid [57], and the non-wetting liquid droplet coated with a hydrophobic powder [58], has been reported. NC droplets formation on a liquid interface in isothermal condition has also been reported [59]. Although describing the floating droplets has been the interest of several studies, to our knowledge a general solution has not been provided for the dual equilibrium states [51, 59, 60]. Further, while the non-coalescence of a droplet on the free surface of the same liquid is widely investigated, the studies using immiscible liquids are scarce.

CHAPTER 2: EWOD BASED MICROPUMP

Some of the materials used in this chapter have been previously published by Elsevier and Springer: R. Shabani and H.J. Cho, “Active surface tension driven micropump using droplet/meniscus pressure gradient”, Sensors and Actuators B: Chemical, 180, 114–121, 2013.

R. Shabani and H. J. Cho, “Flow rate analysis of an EWOD based device: how important are wetting line pinning and velocity effects?”, Microfluidics and Nanofluidics, 2013, DOI: 10.1007/s10404-013-1184-y.

2.1 Introduction

Micropumps are the essential components for many integrated microfluidic systems [2, 3]. Micropumps have been used in biochemical analysis chips and micro chemical reactors [61]. Various methods have been reported for driving micropumps [3, 62]. A passive pumping method previously reported, which takes advantage of the droplet’s surface tension, shows that the Laplace pressure gradient obtained from a difference in surface curvatures is well suited for the microfluidic devices [9]. EWOD is a well-known method for altering the wettability of the surfaces by changing the electric potential [14, 35, 63]. In this chapter an on-demand micropump based on EWOD is proposed which utilizes a Laplace pressure gradient between a droplet and a liquid meniscus as a propellant source, and an alteration of the surface wettability as a valving method without using any moving parts. In contrast to the passive pumping methods in which a non-stopping flow is induced once initiated, in EWOD micropump the induced flow rate is controlled and could be stopped at any time by regulating the voltage. Using

the proposed micropump, aqueous solutions can be driven directly contrary to the micropump driven by continuous EW actuation [16]. The key concept in our device is the linkage of this wettability control and the droplet/meniscus pressure gradient as a propellant method for driving a liquid in a microchannel. The power consumption is expected to be very small due to a very small current (< 0.01mA) associated with EWOD.

2.2 **Materials, design and fabrication**

The idea of the micropump was developed by direct observation of alteration of a water droplet contact angle on hydrophilic surfaces, such as glass or a silicon wafer with a native oxide layer, and hydrophobic surfaces such as a bare silicon wafer, fluorinated surfaces, or Polydimethylsiloxane (PDMS) layers. The droplets with different contact angles would have different Laplace pressures due to the difference in their surface curvatures. A pressure gradient could be induced by altering the liquid contact angle on solid surface. As a low power consumption method for controlling the hydrophobicity of the solids and therefore inducing a pressure gradient, EWOD was employed. The EWOD-based micropump could be turned on and off on demand without any mechanical part and could work with non-electrolyte aqueous solutions.

In designing the micropump, it is assumed that the liquid of interest is applied in the form of a droplet using pipettes and syringes, which is a common protocol in chemistry. The size of the micropump is designed to work best with sample volumes on the microliter scale. The micropump chambers and channels are cast in biocompatible PDMS layer with low cost and simple fabrication process for disposability. PDMS is widely used in biological diagnosis lab on a chip in which transparency is required for

optical measurement [64]. A single PDMS film is used both as bonding layer to the PDMS layer with a microchannel and the hydrophobic layer of the EWOD substrate. There are also other novelties in the fabrication process such as using spin-on glass (SOG) as the insulating layer that could be applied in a very short time compared to normally used dielectric layers in EWOD devices such as silicon dioxide. The EWOD micropump was fabricated in a class 1000 cleanroom.

2.2.1 EWOD substrate

The EWOD substrate of the micropump consists of a conductive layer which is used as the bottom electrode and a dielectric layer which insulates the liquid from the bottom electrode. A hydrophobic layer is formed on top of the insulating layer to put the meniscus in a non-wetting state before applying the voltage. A silicon wafer was used as the conductive layer. Other conductive substrates such as indium tin oxide (ITO) coated glass slides may also be used as the bottom electrode when a direct optical observation through the substrates is needed.

The electrical insulation was tested with both non-electrolyte and electrolyte aqueous solutions. The PDMS layer alone could not completely insulate the electrolyte solutions from the bottom electrode but it could be used to form a defect free under layer for SOG film which could be used as a main electrical insulator. For instance, when a droplet of 1% KCl solution was used (instead of DI water), the generation of bubbles and the leaky current were observed on the single layer of PDMS or SOG, while those were not observed on the SOG/PDMS layer.

Prior to the deposition of the insulating layer the substrate was cleaned via AMD (acetone, methanol and DI water) or RCA cleaning step. In order to maximize the efficiency of the EWOD the insulating layer must be kept thin while maintaining the function of electrical insulator. The PDMS (monomer mixed with curing agent with a weight ratio of 10 to 1) was diluted in toluene (volume ratio of 1 to 3) and spin-coated at 6000 RPM for 10 minutes to suppress the effect of residual surface defects [65]. Then SOG was coated at 3000 RPM for 40 sec to form a leak-free electrical insulating layer which could withstand relatively high EWOD voltages (Fig. 4a). Direct EWOD in which the voltage is directly applied to a droplet on the substrate was used to test the insulating layer.

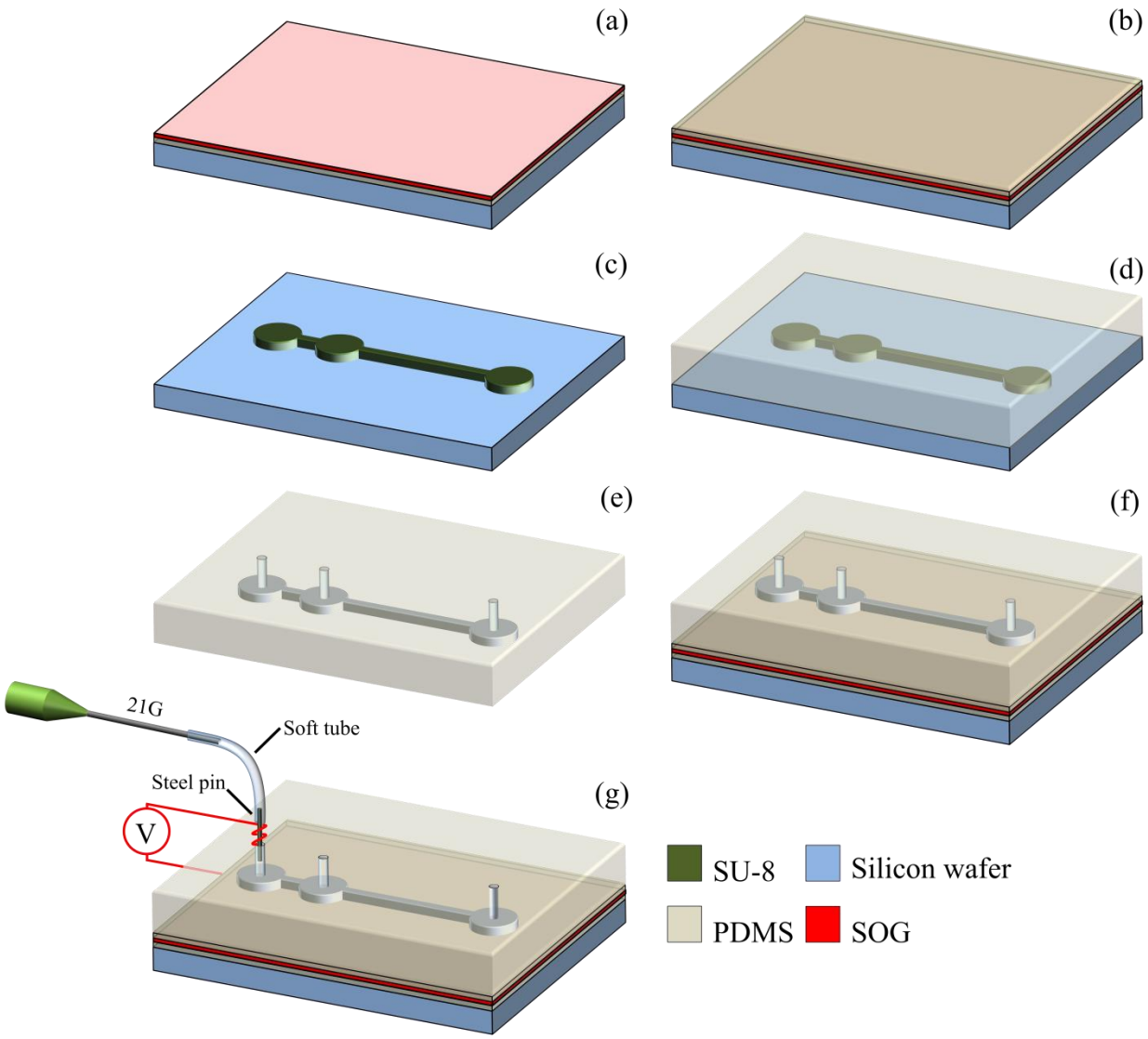

Fig. 4 Fabrication steps for the micropump: (a) Silicon wafer was used as the bottom electrode. Diluted PDMS was spin-coated to mask the defects. A SOG film was formed as an insulating layer (b) Diluted PDMS was spin-coated again to form a thin hydrophobic film (c) A SU-8 mold was fabricated on a separate silicon wafer using photolithography (d) A PDMS block was cast using the SU-8 mold to form microchannels (e) PDMS slab was peeled off the mold and liquid inlet, the air outlet and the drop formation hole were punched (f) PDMS slab with microchannels was bonded to the PDMS film (g) Microfluidic interconnection and the electrical contacts were made.

An ohmic resistor of 1MΩ was connected in series with the EWOD substrate. The large resistor protects the system against any short circuit and at the same time could

be used to measure the current. Since the resistance is large, any small leakage current due to the defects in the insulating layer will result in a large voltage drop in the resistor and could be easily detected.

The hydrophobic layer on top of the insulating layer increases the contact angle and therefore increases the pressure inside the liquid due to the increased liquid-air surface curvature. This is one of the major design considerations in our device in which the accessible range of contact angle is enhanced before applying the electric potential [34]. The hydrophobic layer from this point of view puts the meniscus in a non-wetting state ready to be relaxed and actuated by applying the voltage. In order to reduce the total material cost and simplify the fabrication steps, instead of commonly used hydrophobic materials in EWOD such as CYTOP (Asahi Glass Co.), or Teflon AF (DuPont), a second PDMS film was formed as both the hydrophobic and the bonding layer in our device (Fig. 4b).

2.2.2 Soft lithography and bonding

Su-8 photoresist was used to make a mold on a different silicon substrate using photolithography (Fig. 4c). A separate PDMS block was cast using the SU-8 mold to form a replica of the mold in PDMS (Fig. 4d). The PDMS slab was peeled off the mold and the silicon wafer (Fig. 4e). In addition to an inlet and an outlet (an escape route for air), an orifice for droplet formation was punched into the PDMS block before bonding. This slab was bonded to the EWOD substrate to form a closed microchannel (Fig. 4f). The fully cured PDMS thin film which was formed as the hydrophobic layer in previous step (Fig. 4b) was used as the bonding layer as well. A corona discharge method [66],

was used at room temperature and atmospheric pressure. A leak free bonding for fluids between the PDMS film and the microchannel block was ensured before testing.

This method is different from the other methods using partially cured or uncured PDMS adhesive or a variation of cross linker for bonding. This provides the uniformity of surface characteristic to all of the channel walls. It is worth mentioning that the PDMS thin film, initially becomes hydrophilic temporarily, due to the corona discharge process, but it eventually reverts to the original hydrophobic state [67, 68].

2.2.3 Microfluidic interconnections and electrical contacts

A metallic tube with a diameter of slightly larger than the size of the punched holes in the PDMS block was inserted into the liquid inlet. The PDMS is elastic and could easily hold the inserted tube in its place and make a leak free connection for fluid. A flexible polymer tube was connected to the steel tube (Fig. 4g). A stainless steel tube inserted in the inlet was used as the upper electrode (Fig. 4g). This ensures that electrical contact to the liquid is always maintained. The upper electrode was grounded and the voltage was applied to the conductive layer in the EWOD substrate.

2.3 Micropump operation

2.3.1 Characterization of EWOD substrate

The EWOD substrate was characterized by studying the effect of the electric potential on the droplet contact angle. The applied voltage to the liquid was varied from 0V to 120V and the droplet contact angle on the substrate was measured (Fig. 5). For voltages less than 34V the contact angle is at its highest value, θ_{max}, and remains

constant with an average value of 86º. As the voltage increases from 34V the contact angle decreases. Finally for voltages above 90V the contact angle saturates to its lowest value, θ_{min}, with an average value of 57º. In terms of operation, any applied voltage above 90V only increases the risk of dielectric break-down.

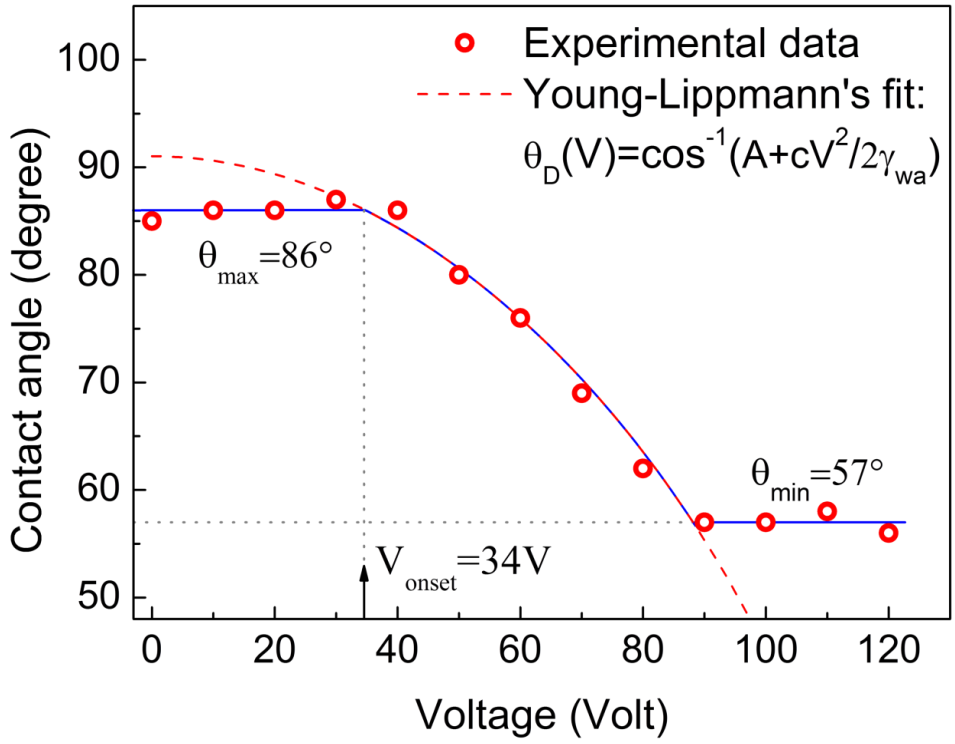

Fig. 5 Droplet contact angle on EWOD substrate vs. voltage: the dash line is the theoretical fit to the data. The hysteresis contact angle is shown as θ_{max}, the saturation contact angle is shown as θ_{min}, and the onset voltage is shown as V_{onset}. In the equation: A is a constant, c is the capacitance of the EWOD substrate.

A voltage of 100 Volts was selected (above 90V and below 120V) for the micropump operation to make sure that the device is working in the saturation region of the contact angle (Fig. 5). In other words increasing the voltage further will not improve the pump operation since the contact angle will not be reduced further. A working

voltage in the saturation region will guarantee that the contact angle is not sensitive to small voltage fluctuations of the device.

The observed plateau at higher voltages is associated with the saturation of the contact angle which prevents the full wetting (zero contact angle) and limits the variation of the surface tension force. The theoretical explanations behind this saturation are still under debate and not conclusive yet. Various explanations have been given, which try to find this phenomenon's origination from trapping of electric charge, ionization of gas close to the liquid-solid WL, WL instability, zero interfacial tension criterion and the droplet resistance [34, 69].

The constant value of the contact angle at lower voltages (< 34V in Fig. 5) is related to the hysteresis of the contact angle or the pinning effect [46, 69]. The pinning effect is the tendency of the liquid to preserve its wetting or non-wetting states on the solid surface. This effect plays an important role at lower voltages in which EWOD is not strong enough to force the liquid to wet the hydrophobic surface.

The pinning effect tends to pin the WL to the surface. When an external force (e.g. due to a pressure gradient) is exerted on a WL, the pinning effect makes the WL on the surface stationary and as a result the contact angle is increased or reduced without the movement of the WL depending on the direction of the external force [26]. The EWOD effect tends to increase the wetted area (the contact area between the droplet and the surface) and therefore tends to reduce the contact angle. The droplet volume is constant so an increase in the wetted area means a decrease in contact angle (Eq. (3)). However, the EWOD is too weak at lower voltages and it could not move the WL due to the pinning effect and therefore the contact angle does not change.

The application of silicone oil to the solid surface has proved to be effective in reducing the contact angle hysteresis and improving the liquid's reaction to the change in electric potential in EWOD setup. However such surface treatment is often not desirable due to the oil residues and non-uniformity of its effect.

It is apparent that there is an onset voltage, V_{onset}, in which the contact angle starts a transition from a higher constant value to a lower constant value. The transition region could be understood using the Young-Lippmann's equation [24, 70], which states that the contact angle is a function of the applied voltage and the surface tensions in an EW setup:

$$\theta_D = \cos^{-1}((\gamma_{sa} - \gamma_{ws} + cV^2/2)/\gamma_{wa}) \quad (1)$$

, where θ is water contact angle on the substrate, γ_{sa}, γ_{ws} and γ_{wa} are the substrate-air, water-substrate and water-air surface tensions respectively in the absence of electric potential, V is the voltage and c is the capacitance ($\mu F/m^2$) of the EWOD substrate. Since the surface tensions are constant in this experiment, and c is constant for a specific setup, we could simplify the Young-Lippmann's equation to:

$$\theta_D(V) = cos^{-1}(A + BV^2) \quad (2)$$

, where A and B are two constants. Equation **(2)** could be fitted to the experimental data using A and B as fitting parameters (dash line shown in Fig. 5). A good agreement was found between the EW experimental data and the theoretical Eq. (2) for voltages above 30V and less than 90V. The values obtained for A and B for the best fit are -1.8×10^{-2} and 7.2×10^{-5} ($1/V^2$) respectively. Using γ_{wa} of 72 mN/m, the capacitance of the micropump EWOD substrate, c, is obtained to be 10 ± 0.6 $\mu F/m^2$.

The capacitance, c, and the thickness of the insulation layer, t, are related as $c = (\varepsilon_0 \varepsilon_r)/t$, where ε_0 is the vacuum permittivity and ε_r is the relative permittivity of the insulating layer. The dielectric layer in the fabricated micropump consists of a thin SOG layer and two PDMS films. The thickness of the SOG formed at 3000 RPM for 40 seconds is 0.2 μm. Considering the known values of relative permittivity, ε_r, of SOG and PDMS (3.9 and 2.65) and the thickness of PDMS film (1.1 μm) [65], the capacitance is calculated to be 10 $\mu F/m^2$ which is in excellent agreement with the result obtained from the Young-Lippmann's equation.

The Young-Lippmann's fit to the contact angle vs. voltage could be utilized to demonstrate the efficiency of EWOD setup and used as comparative measure for evaluating the strength of EWOD in one device with that in other fabricated devices. For this purpose four parameters associated with Fig. 5 are utilized: the saturation contact angle, θ_{min}, the hysteresis contact angle, θ_{max}, the capacitance of the substrate, c, and the onset voltage, V_{onset}. EWOD setup, with a larger difference between the hysteresis contact angle and the saturation contact angle, is more efficient and for a higher capacitance, c, the switching from θ_{max} to θ_{min} occurs sharply and for less change in the applied voltage (Eqs. (1) and (2)). In addition, a lower onset voltage means a lower working voltage for the device. This gives an insight into the design guideline for energy-efficient EWOD devices.

2.3.2 Working principle

For priming, water was supplied in the channel to make contact with the hydrophobic surface of the EWOD substrate at the bottom of the channel and to form a

droplet as a positive pressure source on top of the channel (Fig. 6). A liquid meniscus is also formed inside the channel. The droplet and the meniscus contact angles are in a non-wetting state on the hydrophobic PDMS surface.

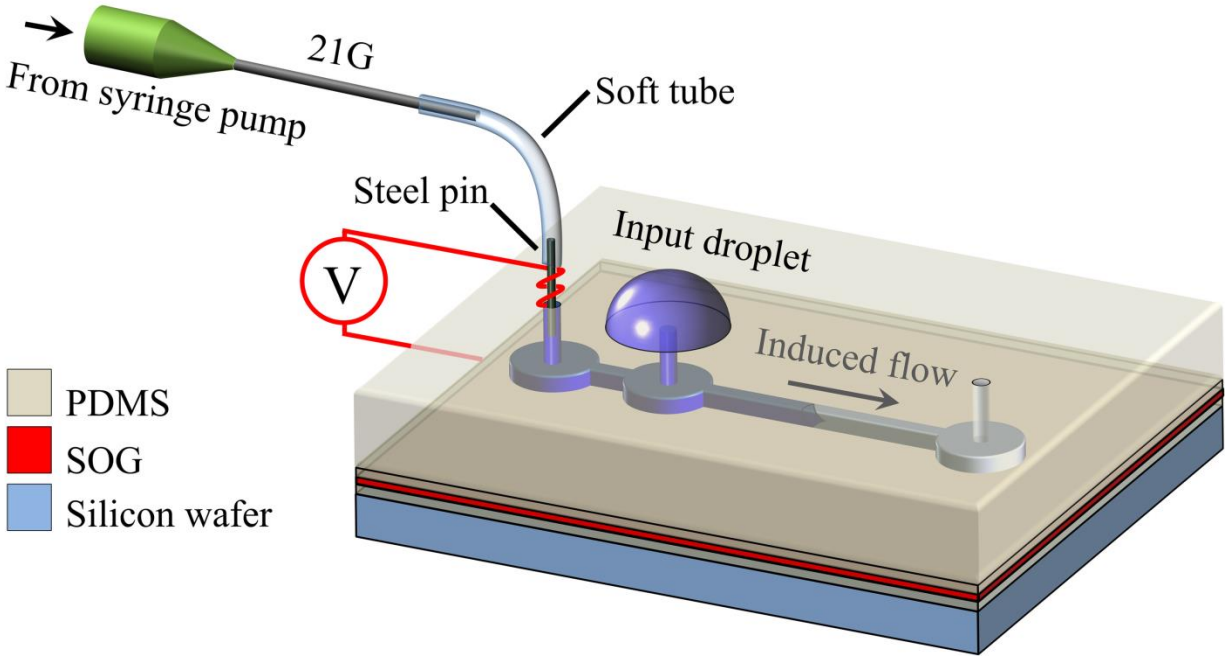

Fig. 6 EWOD based micropump: a microchannel cast in PDMS slab is bonded to the EWOD substrate (PDMS/SOG/PDMS/Si). An input droplet is driven into the channel and a continuous constant flow is induced upon turning on the voltage.

Prior to applying the voltage the droplet was stable and the liquid inside the channel was in the non-wetting state (Fig. 7a, b). Only, after applying the voltage (V=100V), the droplet starts flowing into the channel (Fig. 7c, d). The EWOD substrate which is in contact with the liquid, works similar to a capacitor. A fringing electric field, which is formed at the substrate-liquid-air interface, helps the liquid to wet the surface and move forward in the channel. In other words the decrease in the contact angle at the bottom of the channel reduces the liquid meniscus curvature inside the channel and

produces a positive pumping pressure. The droplet/meniscus pressure gradient is activated and the droplet is pumped into the channel with a uniform flow rate.

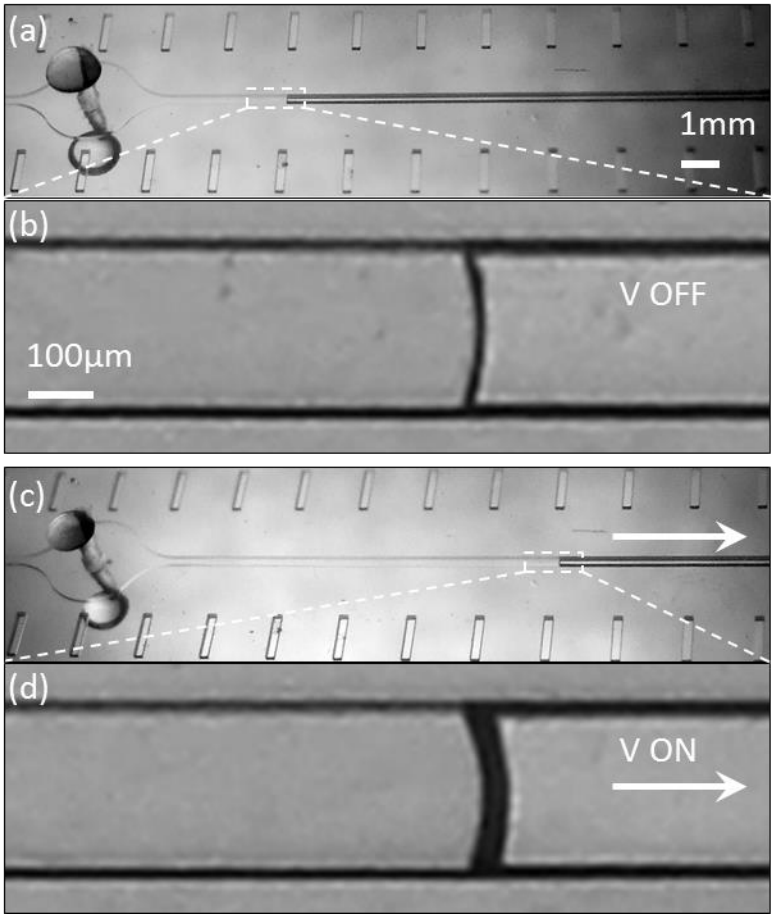

Fig. 7 The micropump in operation at 100 V (a) a slanted view of the input droplet and the meniscus before applying voltage, (b) a magnification of the same meniscus in a, observed from top, (c) a slanted view of the reduced input droplet and the advanced meniscus in the channel after applying voltage (d) the same meniscus in c, observed from top which shows the increased wetting area.

The micropump flow rate was measured to be uniform for different sizes of the droplet for the similar initial liquid length in the channel and a voltage of 100V. Since in microfluidic devices the flow is laminar, their performance in the laminar regime is enhanced by maintaining the flow at a constant rate [9]. The result shows that regardless of reduction in the droplet size during the operation, the flow rate remains

constant [71]. Nevertheless the flow rate is strongly dependent on the initial droplet size (Fig. 8a) and the higher flow rate is obtained from a smaller droplet. A smaller droplet has a higher Laplace pressure due to higher surface curvature and induces a higher flow rate inside the channel. Moreover the liquid flow rate in the channel is increased by increasing the micropump's working voltage (Fig. 8b). The meniscus contact angle on the bottom of the channel is reduced by increasing the voltage. The meniscus with lower contact angle implies a lower pressure in the channel and therefore a higher flow rate is induced.

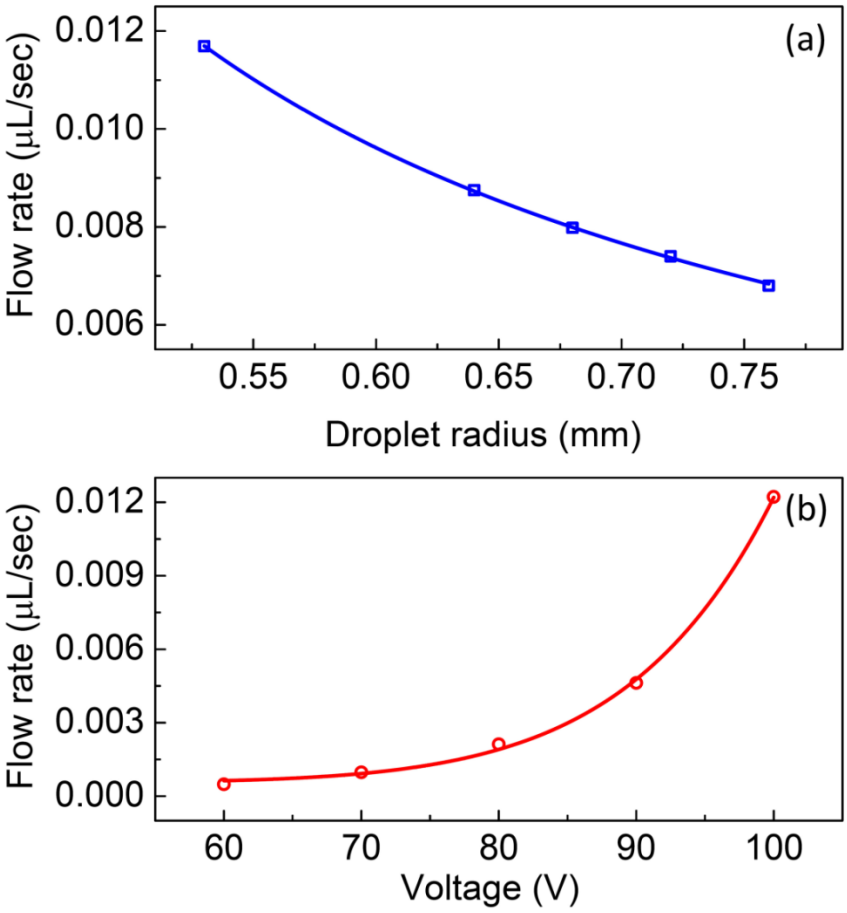

Fig. 8 The volumetric flow rate in the channel is shown as a function of (a) droplet radius at a constant voltage of 100 V and (b) voltage for a similar droplet radius of 0.5 mm.

The droplet volume vs. time could be found from the information given in Fig. 8, if the initial droplet volume is known. The change in droplet volume is equal to the change in liquid volume in the channel, which could be obtained by multiplying meniscus velocity in the channel from Fig. 8 by the channel cross section area ($250\times60\mu m^2$). Since the meniscus velocity in the channel is constant, the droplet volume decreases linearly with time. The micropump input droplet is assumed to be a spherical cap since its radius, R_D, is less than the capillary length for a droplet, $(\gamma_{wa}/4\rho_w\, g)^{1/2}$, where ρ_w is the density of water ($997\ kg/m^3$) and g is standard gravity. The droplet's initial volume, V_D could be calculated from:

$$V_D = \pi\left(\frac{a_D}{\sin\theta_D}\right)^3\left(\frac{2}{3}-\frac{\cos\theta_D}{3}(2+(\sin\theta_D)^2)\right) \quad (3)$$

, where a_D, is the initial droplet wetting radius and θ_D is the initial droplet contact angle (86°). Using the top view image of the droplet, the radius of wetting area, a_D, could be measured directly and is used in Eq. (3) instead of the droplet radius, R_D.

The electrical power, $\dot{W}$, required for the operation is estimated by:

$$\dot{W} = VI = V\frac{dQ}{dt} = V\frac{d(CV)}{dt} = V^2\frac{dC}{dt}$$

$$= V^2\frac{d(cA)}{dt} = cV^2\frac{d(A)}{dt} = cV^2\frac{d(\forall/h)}{dt} = \frac{c}{h}V^2\frac{d\forall}{dt} \quad (4)$$

,where V is the EWOD voltage, ∀ is the liquid volume in the channel and *h* is the height of the channel. The channel height, is 60 μm, c was calculated to be $10\mu F/m^2$ and V is 100 Volt. For the smallest droplet the liquid volumetric flow rate in the channel,

is the highest (Fig. 8). Thus, for a flow rate of 0.012 μL/sec, the maximum power consumption is extremely low, 12 nW.

2.3.3 EWOD microvalve

The key concept in the pump design is the utilization of the pressure gradient between the droplet and the liquid in the channel as the driving pressure of the micropump. The pressure gradient is generated by performing EWOD in the channel. A flow is induced/stopped in the channel by turning on/off the voltage (EWOD microvalve).

A numerical calculation was carried out using MATLAB to predict the switch on voltage of the EWOD microvalve for different sizes of the droplets. Some of the parameters used in the analysis are shown in the side and top views of the micropump schematic (Fig. 9a, and b). The size of the channel is exaggerated as compared to the orifice size, d, for clarity. The micropump channel has a rectangular cross section with a height, *h*, and a width, *w* (60μm × 250μm). Although the nominal depth of the channel is supposed to be 100 μm according to the data sheet provided by the SU-8 photoresist manufacturer (MicroChem Corp.), the channel thickness was measured at several different points using a surface profiler (Tencor Alpha-Step 200) to be 60μm. The input droplet has a radius of curvature of R_D and a contact angle of θ_D. The liquid meniscus contact angles on the channel sides and top, θ_{Ch}, are similar while the meniscus contact angle on the bottom of the channel, θ_{EW}, is smaller due to EWOD.

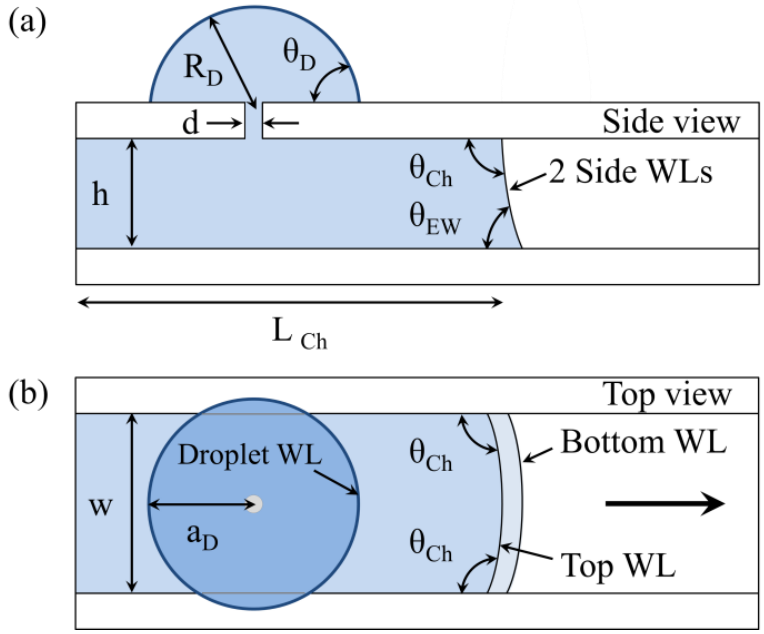

Fig. 9 Analytical model physical parameters defined on (a) side view of the micropump and (b) top view of the micropump.

Also the forces exerted on the meniscus WLs on the four walls of the channel are shown in Fig. 10. Unlike the spherical shape of the droplet, the meniscus inside the channel has a complicated shape since θ_{Ch} and θ_{EW} are not equal. Therefore to obtain the meniscus pressure, an analysis of the surface tension forces acting on the advancing WLs in the channel is utilized. The effect of the electrostatic force is taken to account by considering a reduced θ_{EW} at the bottom of the channel due to EWOD.

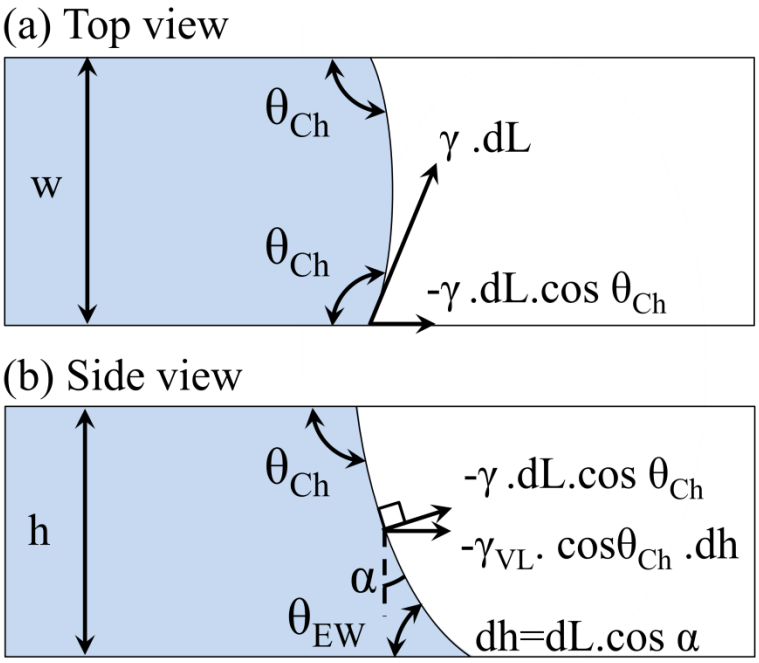

Fig. 10 Surface tension force exerted at the meniscus WL on the channel side wall (a) top view of the channel with the width of w. Differential length of the WL on the side wall is dL (b) side view of the channel with a height of h.

The liquid meniscus in the channel is not spherical, yet due to a uniform Laplace pressure in the liquid, the sum of the inverse of the two radii of curvatures ($1/R_1+1/R_2$) should be similar at all points on the meniscus. Except for the cases with a high symmetry, such as a square or rectangular channel with equal contact angles on all the channel walls [72], and a confined droplet at equilibrium between two plates with equal contact angles [73], computational methods have been used to find the meniscus pressure [36]. Nevertheless, it is possible to calculate the pressure of the meniscus inside a rectangular channel for a general case (different contact angles on the channel walls) without the need to calculate the surface curvature.

An expression was derived for liquid meniscus pressure, P_M, based on the forces exerted on the meniscus WLs on the four walls of the channel. The parallel component of the surface tension force exerted on the liquid WL on the channel's side wall (Fig.

10a, b) was found to be $\gamma h cos\theta_{Ch}$. Similarly the parallel components of the surface tension forces exerted on the wetting lines on the top and bottom walls of the channel were found to be $\gamma w cos\theta_{Ch}$, and $\gamma w cos\theta_{EW}$ respectively. The meniscus pressure, P_M, is derived by dividing the sum of the surface tension forces parallel to the channel by the channel area:

$$P_M = (-\gamma_{wa}/wh)[(2h + w)\cos\theta_{Ch} + w\cos\theta_{EW}] \quad (5)$$

The spherical droplet pressure, P_D, from Laplace pressure equation is $2\gamma_{wa}/R_D$. The micropump driving pressure, P_{MP}, is the difference between P_M and P_D:

$$P_{MP} = \gamma_{wa}\left(\frac{2}{R_D} + \frac{\left((2h + w)\cos\theta_{Ch} + w\cos\theta_{EW}\right)}{wh}\right) \quad (6)$$

The micropump pressure predicted by Eq. (6) depends on the accurate estimation of θ_{Ch} and θ_{EW}. When the EWOD valve is switching from off to on, θ_{Ch} is equal to the maximum advancing contact angle at zero velocity which was measured to be 100° [71]. θ_{EW} (Fig. 5) was scaled from 86° to 100° at zero voltage to account for the advancing contact angle. Eq. (6) and the voltage dependence of θ_{EW} were utilized to predict the micropump driving pressure at different voltages and for various droplet sizes (Fig. 11). The input droplet radius and the voltage are used to plot the driving pressure of the micropump in a 3D graph (Fig. 11). The constant pressure contours, including the zero pressure line, are shown on the surface. The EWOD valve will be opened and a flow will be induced in the channel for a combination of voltage and R_D for which the pressure is positive, (Red region in Fig. 11). The valve remains closed if the pressure is negative (Blue region in Fig. 11).

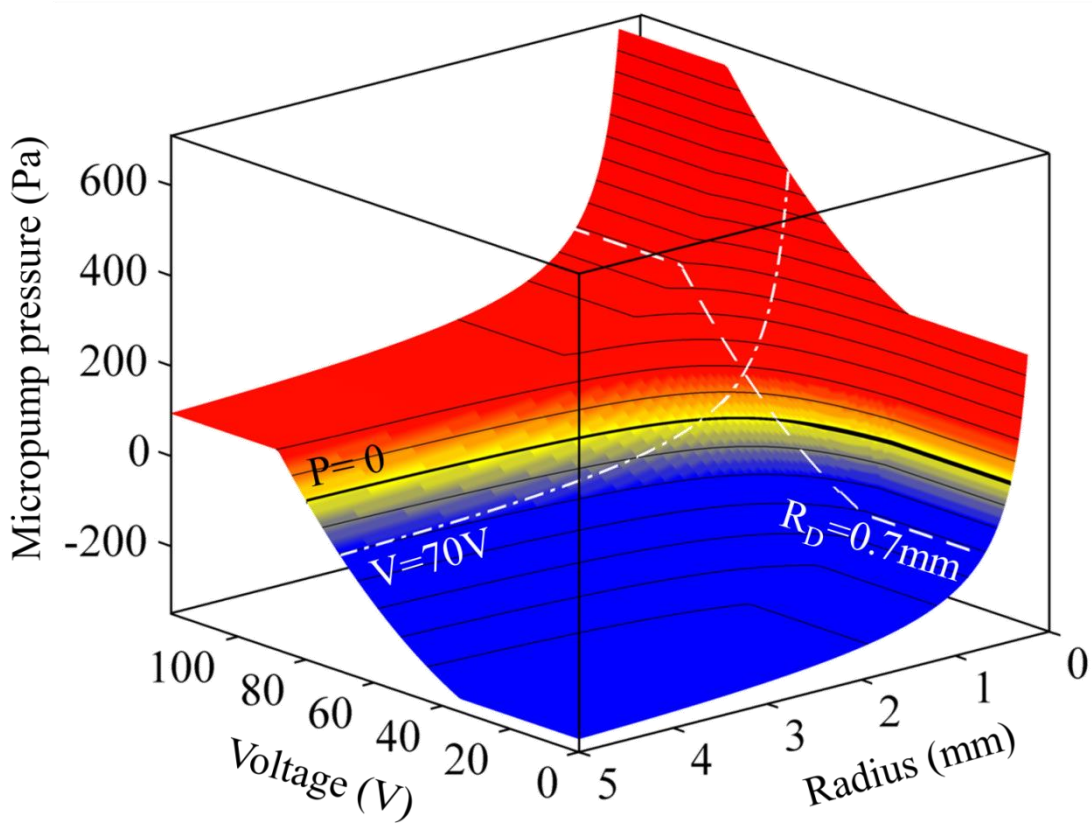

Fig. 11 The outputs of MATLAB code showing the micropump pressure as a function of voltage and droplet radius in a three dimensional representation.

For a constant R_D of 0.7 mm (white dashed line) the pump pressure crosses the zero value as the working voltage increases (Fig. 12a). It is shown that for a very small droplet radius, such as 0.2 mm, the pump pressure is always positive and valve is open, even without applying voltage. In other words the surface curvature of small droplets is high enough to drive the pump by means of a high Laplace pressure inside the droplet.

Also for a constant voltage (white dot-dashed line), the pump pressure crosses the zero value as the radius of the input droplet increases (Fig. 12b). For a range of droplet sizes in region I (Fig. 12b) the valve will be always open without applying voltage. In the

region II at zero voltage the valve is closed and by increasing the voltage it will switch to be open. Therefore region II represents the range of R_D for which the droplets are pumped on-demand. Further increasing the voltage will increase the pressure and induce a higher flow rate in the channel.

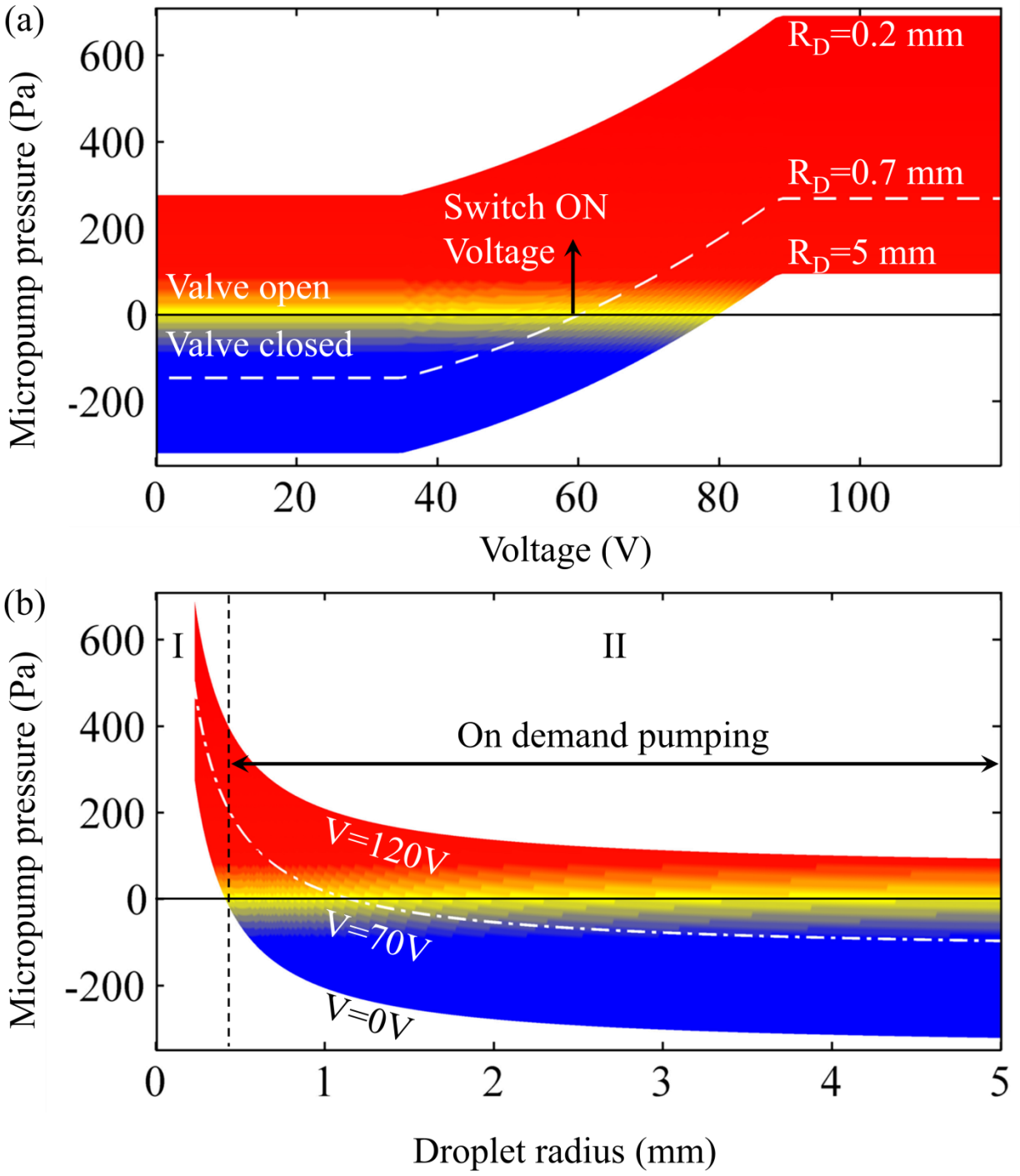

Fig. 12 (a) Voltage effect highlighted for R_D= 5, 0.7 and 0.2 mm and demonstration of switch in EWOD microvalve (b) droplet radius effect highlighted for V=0, 70 and 120V and presentation of on-demand pumping.

The micropump pressure gradient is proportional to the liquid flow rate in the channel:

$$P_D - P_M = K\mu_w L_{eff} Q \quad (7)$$

,where K, is a geometrical constant, μ_w is the water viscosity, Q is the volumetric flow rate and L_{eff} is the effective liquid length in the channel (the sum of the liquid length in the channel, L_{Ch}, orifice length, and other head losses). Equation **(7)** shows a direct relation between the micropump driving pressure, P_{MP} and the flow rate in the channel. The code outputs for micropump pressure, shown in Fig. 12a and b, strongly correlate with the flow rate data presented in Fig. 8a and b. The flow rate decreases by increasing the size of the input droplet and increases by increasing the voltage (Fig. 8). This observation correlates with the predicted micropump pressure (Eq. (7)), which shows the same trend by altering the input droplet size and the voltage.

2.3.4 Input droplet wetting modes

After the pump switches on by applying the voltage, droplet shrinks in two phases: in phase one, the droplet wetting area remains constant as the contact angle is reduced to 80° (Fig. 13a to b). In phase two, both the droplet wetting area and the contact angle decrease (Fig. 13b to c). Several models are proposed in the past to describe different phases of a shrinking droplet [74-77]. However, the comparison of the different models reveals that a generally accepted model has not been developed yet. In general, the different observations could be attributed to different experimental conditions.

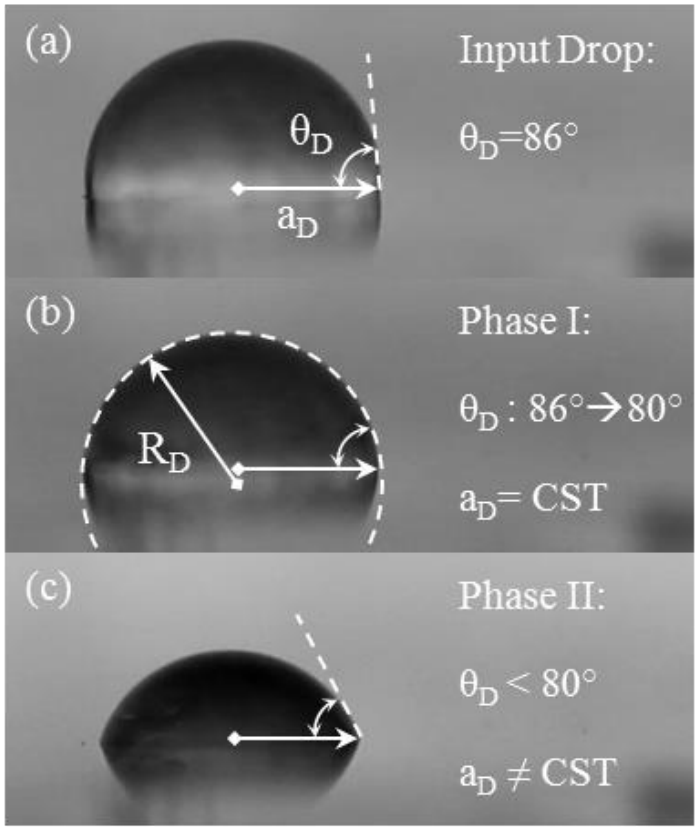

Fig. 13 Droplet pumping phases in which R_D is surface radius of curvature and a_D is droplet wetting radius (a) Stable droplet on top of the PDMS channel with an initial contact angle, θ_D, of 86º prior to applying voltage (b) phase I: a_D is constant while θ_D decreases. (c) phase II: both a_D and θ_D decrease.

By observing the gradually evaporating droplets on a solid surface, two modes are described [74]. In the first mode the contact angle is decreasing with a constant wetting area (CWA) and in the second mode the wetting area decreases with a constant contact angle (CCA). Birdi and Vu have described the shrinkage of the water drop as a single phase phenomenon (attributed to the pinning effect) [75], in which depending on the initial value of the contact angle, only one of the two modes mentioned above takes place: CWA for solid surfaces with wetting characteristics, such as glass (θ_D<90°) and CCA for surfaces with nonwetting characteristics such as Teflon (θ_D>90°).

McHale et al. suggested a two phases model [76]. The first phase is similar to the previous model [75], for both hydrophilic and hydrophobic surfaces. However in the second phase both the contact angle and the wetting area are changing though the evaporation time scale is dominated by the first phase. This is due to the increasing rate of reduction of the contact radius and the velocity dependence of the contact angle. Yu et al. also have reported a two phases model [77]. However their model does not depend on the initial contact angle. It always starts from CWA and switches to CCA. This model is identical to the model used to describe the shrinkage of a passively pumped droplet by a surface tension based pumping method [9].

Our observations are in relatively good agreement with McHale et al. [76], although due to the micropump's higher flow rate the second phase is much more pronounced. This is the major difference between our experiment and evaporating droplets. The concurrent decrease of the droplet's contact angle and wetting area is also observed in the forced wetting [78], in which the droplet wetting area is forced to move by application of an external effect, such as a pressure gradient in the micropump. In such case the contact angle depends on the velocity of the WL, and by changing the velocity the contact angle is changed [71].

CHAPTER 3: DROPLETS ON SOLID SURFACES AND WETTING LINE

Some of the materials used in this chapter have been previously published by Springer: R. Shabani and H. J. Cho, “Flow rate analysis of an EWOD based device: how important are wetting line pinning and velocity effects?”, Microfluidics and Nanofluidics, 2013, DOI: 10.1007/s10404-013-1184-y.

3.1 Introduction

In devices that are designed based on EWOD, a liquid meniscus is manipulated by an applied voltage which reduces the contact angle of the WL formed at the boundary between the liquid, air, and the solid surface. The behavior of the moving WL has a complex nature due to the WL pinning and WL velocity effects, which alter the liquid contact angle on the solid surface from its equilibrium value obtained from Young’s equation [24, 25]. The WLE effect or pinning effect, is a result of the local microscopic defects on the solid surface [26], by which liquid is pinned to the surface. Therefore, different values for contact angle are expected depending on whether the WL is in advancing or receding modes. The contact angle is also changed when the WL is moving, depending on the magnitude and direction of the WL velocity [27, 28].

3.2 Contact angle hysteresis

The EWOD substrate of the micropump consists of a silicon wafer, a SOG layer and a thin PDMS layer. Silicon wafer is a conductive layer and SOG is an insulating layer with a thickness of 0.2μm and a dielectric constant of 3.9. PDMS is a hydrophobic layer with a thickness of 1.1μm. The micropump’s input droplet is stable with a contact

angle of 86° before applying a DC voltage between the electrodes (Fig. 6). Upon applying the voltage, the droplet is driven into the channel in two phases, with a continuous flow. In phase I, the droplet's wetting area remains constant until droplet's contact angle decreases to 80° due to pinning. Such phenomenon has been also observed for a passive micropump [9].

In contrast, in phase II, both the droplet's wetting area and contact angle decrease as the droplet is driven into the channel. The further decrease in droplet's contact angle is due to WL velocity effect [71]. The reported variable droplet's contact angle on untreated PDMS surface is in agreement with the data reported in literature [9, 71]. These results are later incorporated in the flow rate analysis of the micropump.

In an experiment, this phenomenon was studied for droplets with advancing and receding WLs by measuring the droplet's contact angle, θ_D, with respect to its WL position. A syringe pump was connected to a microchannel leading to an open orifice formed in a PDMS layer (Fig. 14a). Pinning without EWOD was observed by injecting (drawing) liquid at a very low flow rate to form an advancing (receding) droplet on top of the orifice.

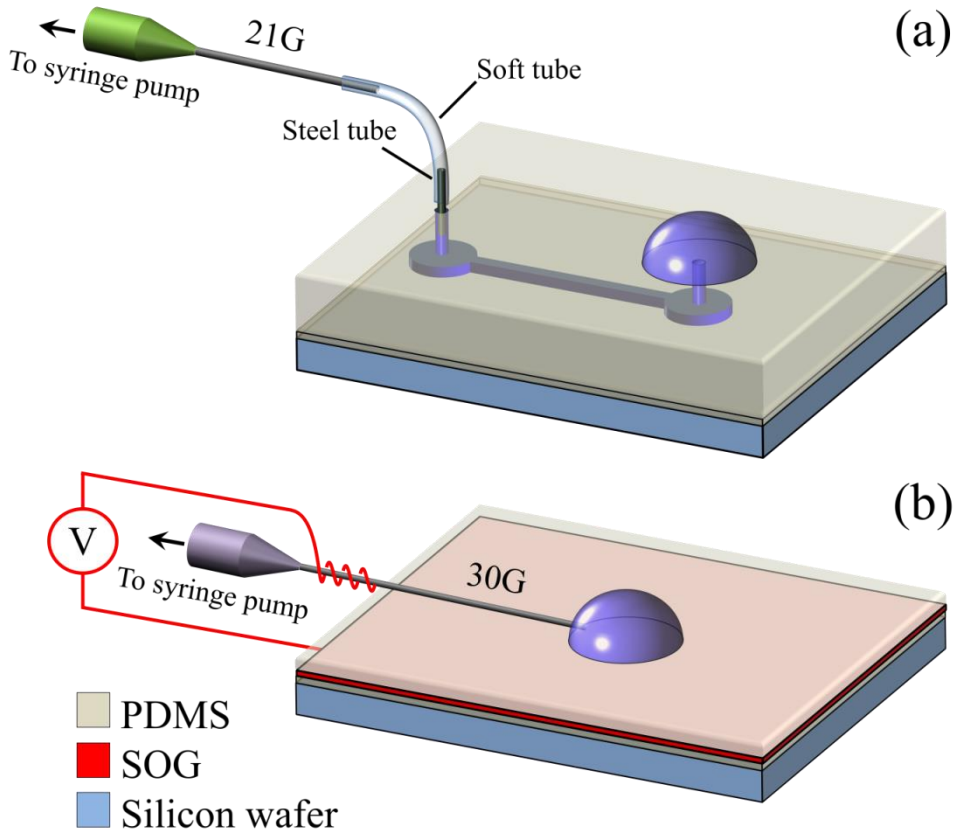

Fig. 14: Experimental setups for (a) contact angle hysteresis and WL velocity effect and (b) pinning effect with EWOD.

In stage 1 of the experiment, the liquid was pumped out of the orifice with a uniform and low flow rate of 0.1 µL/min (Fig. 15a). The contact angle remained constant at the advancing contact angle, θ_A, with an average of 86° as the WL was moving forward. In stage 2 the droplet from stage 1 was drawn back into the orifice using refilling mode of the syringe pump. The WL was pinned to the substrate as the contact angle was decreasing from θ_A to the receding contact angle, θ_R, with an average of 69°. In stage 3, the droplet was drawn further. The droplet contact angle remained constant at θ_R as the WL was receding. Then liquid was pumped out again (stage 4) and the droplet contact angle increased from θ_R to θ_A while the WL was pinned to the surface.

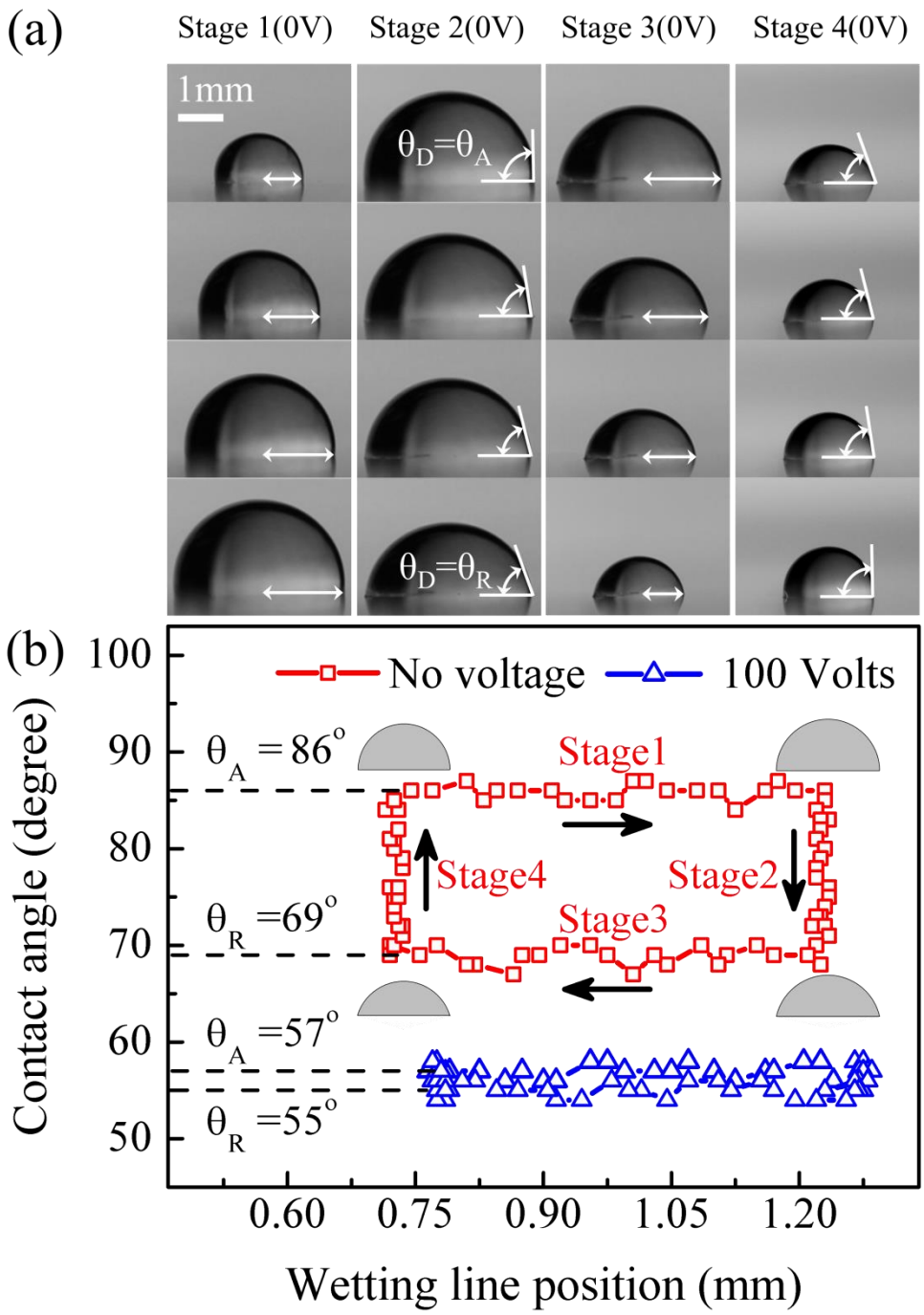

Fig. 15: Contact angle hysteresis and the mode switch (a) A droplet (on top of an orifice formed in PDMS) with advancing (stage 1), receding (stage 3), and pinned (stages 2 and 4) WLs when no voltage is applied. Droplet contact angle, θ_D, decreases in stage 2 and increases in stage 4 due to pinning (b) Droplet contact angle versus its WL position, measured from the center of the droplet. Contact angle hysteresis loops for 0V and 100V.

The contact angle hysteresis with four stages is shown as a closed loop by plotting the contact angle versus WL position (Fig. 15b). Droplet's WL position was measured from the center of the droplet. Interestingly, when EWOD is performed the droplet exhibits a similar behavior, only the contact angle hysteresis loop is shifted toward lower contact angles (Fig. 15b).

A high gauge needle connected to a syringe pump was placed close to EWOD substrate (Si as lower electrode/ Dielectric SOG/ Hydrophobic PDMS) and used for injecting (drawing) liquid (Fig. 14b). The needle was also used as the upper electrode. A power supply was connected between the needle and the silicon substrate. Liquid was injected (drawn) through the needle at a very low flow rate, to form an advancing (receding) droplet on EWOD substrate. Contact angle hysteresis is reduced by increasing the DC voltage, as evidenced by the smaller area occupied by the hysteresis loop. This is discussed in more details in next section.

3.3 Wetting line velocity effect

The advancing (receding) contact angles are further changed by the direction and the magnitude of the droplet's WL velocity [27, 78]. In next experiment this effect was shown for positive (advancing), zero, and negative (receding) velocities (Fig. 16a, b). The setup depicted in Fig. 14a, was used to observe the effect of WL velocity on droplet's contact angle by increasing the injecting (drawing) flow rate (dynamic contact angles). The contact angle was measured versus the WL velocity using frame by frame video analysis.

In stage A, a droplet is pumped out of the orifice (positive WL velocities). For a constant pumping rate, the droplet's WL velocity is higher when it is small and becomes

lower for larger size of the droplet. A higher value for contact angle is observed for higher velocities. In stage B, the droplet is drawn back into the orifice without giving time to the droplet for relaxation. The contact angle is reduced to 80° while the wetted area remains constant. The contact angle change at zero velocity (vertical line) represents the pinning or the hysteresis in contact angle (Fig. 16b, stage B). In stage C, the droplet is drawn further resulting in negative WL velocity. Here, a smaller contact angle is observed for higher magnitude of the WL negative velocity.

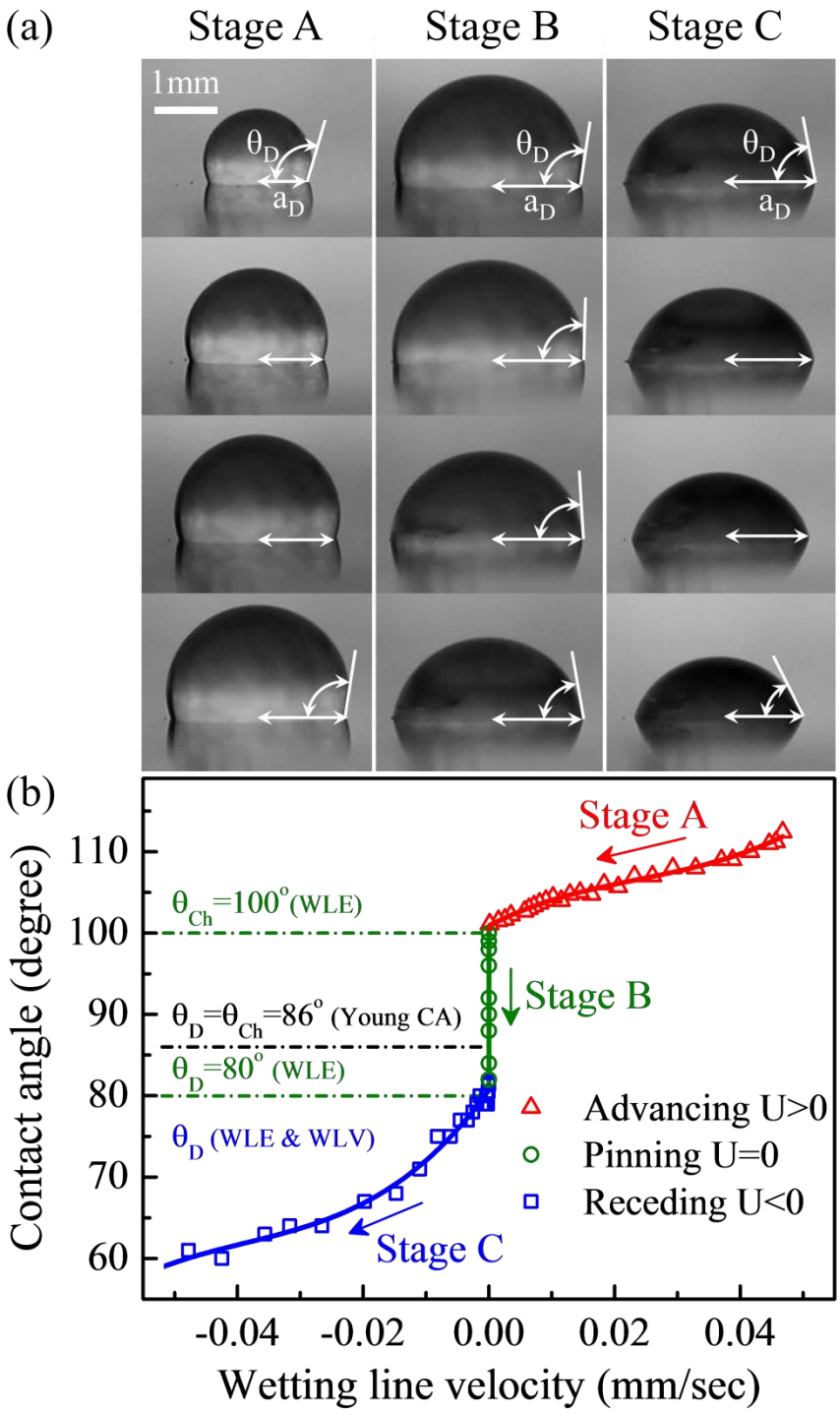

Fig. 16: WL velocity effect on the contact angle (a) A droplet is pumped out (stage A) and drawn into (stages B and C) an orifice on PDMS surface. (b) Droplet's dynamic contact angle versus its WL velocity. The values of the droplet and channel contact angles (for a pinned WL in Stage B), θ_D and θ_{Ch} respectively, are estimated and labeled.

In summary, a significant change in contact angle as large as 50° could be induced by WL velocity and pinning effects for the range of WL velocities studied here. The measured data for the receding WL (Fig. 16b, stage C) is used to describe the variable contact angle of the shrinking droplet versus its WL velocity during the phase II of the micropump operation [71].

For an initial input droplet diameter of 1 mm a meniscus velocity of 0.5 mm/sec was measured in the microchannel using frame by frame video analysis of the top view of an advancing meniscus in the channel. The liquid velocity was obtained from the slope of the measured meniscus position versus time. The meniscus velocity is much larger than the velocity of the droplet WL in Fig. 4b (<0.05 mm/sec). For such high velocities the method used in Fig. 16a, b is not feasible due to limitation in flow rate of the syringe pump and the droplet instability and deformation. Fortunately, without applying any voltage to the setup depicted in Fig. 6, all four walls of the channel have the same contact angle and θ_{Ch} could be directly measured from top view images. Meniscus velocities, U_{Ch}, as high as 2 mm/sec, could be easily achieved inside the channel. Experimental data depicted in Fig. 17 are used for the contact angle on the side and top walls of the channel in the flow rate analysis.

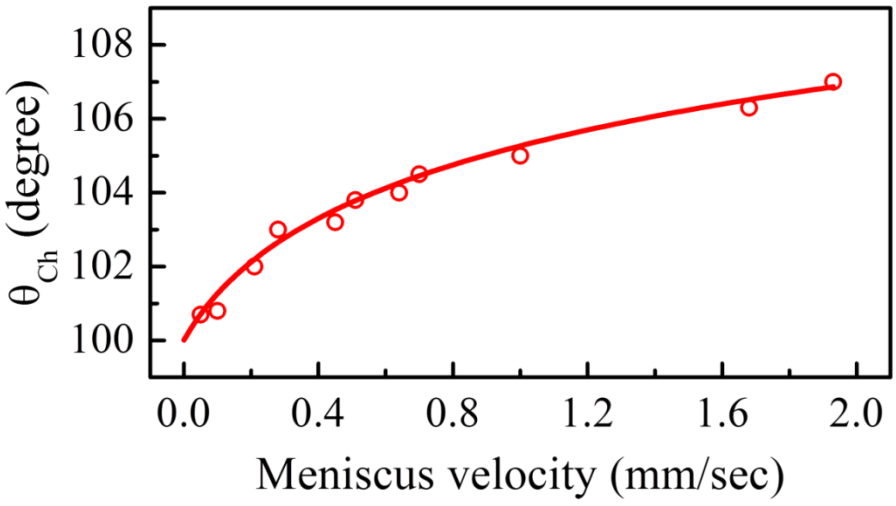

Fig. 17 Dynamic contact angle in the channel, θ_{Ch}, versus meniscus velocity.

The last data needed is the liquid contact angle on the bottom of the channel, θ_{EW}, upon applying a DC voltage of 100V. However, the direct observation of θ_{EW} from the side view of the PDMS channel is not feasible unlike the observation of θ_{Ch} from the top view. This is due to non-smooth and opaque surfaces when PDMS was cut on the sides. Moreover the contact angle calculated by Young–Lippmann's equation for a voltage of 100V could not be used since the pinning and WL velocity effect are present at the bottom of the channel (dynamic θ_{EW} at the advancing WL in the channel). Instead, θ_{EW} was considered as a fitting parameter and the validity of values obtained for θ_{EW} were justified by comparing with other experimental data, i.e. the contact angle should be smaller in the presence of EWOD as compared to θ_{Ch}.

3.4 EWOD effect on wetting line pinning

Micrographs of a droplet with advancing and receding WLs show the EWOD voltage effect on the WL pinning and the contact angle hysteresis (Fig. 18a). DI water

was injected (drawn) through a needle, at a very low flow rate to form a droplet with advancing (receding) WL. A high gauge needle (30G) was used to minimize the distortion in the droplet shape. The needle was also used to apply a DC voltage to the droplet Fig. 14b). To avoid the WL velocity effect, ample time was given to the droplet for relaxation.

The advancing (receding) θ_D was measured for different DC voltages between 0V to 120V (Fig. 18b). For voltages less than 40V the advancing contact angle is not affected by EWOD (θ_A ~86 º), while above that, the contact angle is decreased. However, for voltages above 90V, the contact angle reaches its lowest value and saturates at θ_A ~ 56º [69]. A very similar pattern was observed for the receding contact angle, only with a larger onset voltage for EWOD to affect the contact angle (70V). Such transition region between the highest and lowest contact angles by increasing the applied voltage has been also reported previously [46]. Interestingly, the WL pinning effect (the difference between the advancing and receding contact angles, $\theta_A - \theta_R$), is noticeable at voltages below 40V (region I in Fig. 18b), while at voltages above 70V there is no significant pinning effect (region III in Fig. 18b). There is also a transition region in which the pinning effect decreases gradually since only θ_A is affected by EWOD (region II in Fig. 18b).

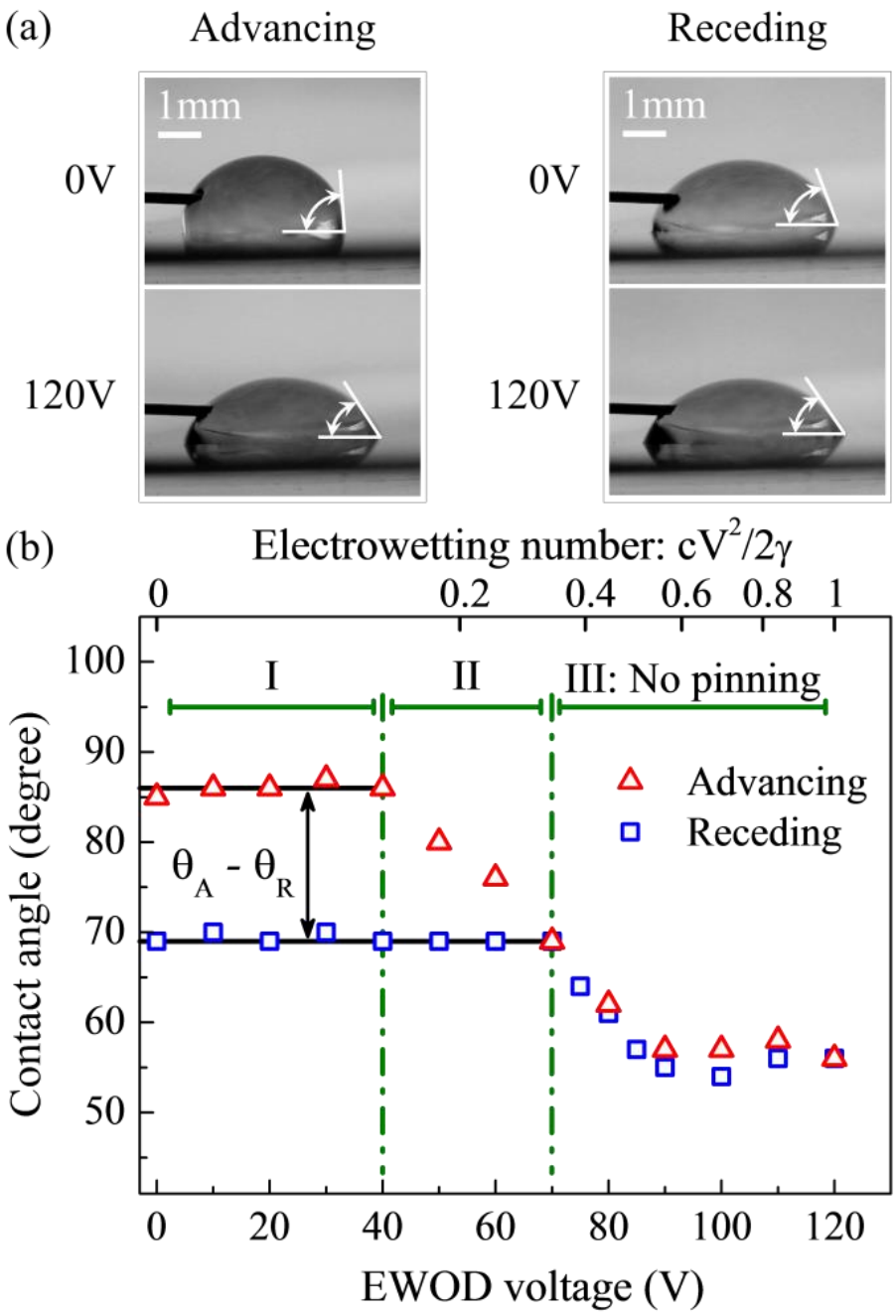

Fig. 18: WLE effect competing with EWOD (a) Droplet's advancing and receding contact angles decrease by increasing the voltage from 0V to 120V. Also the difference between advancing and receding contact angles decreases at higher voltages. (b) Advancing and receding contact angles at different voltages (EW numbers).

It has been reported that for a DC voltage, the hysteresis is essentially voltage independent [79], while in this study a decrease in the pinning effect was observed for voltages above 40V (region II and III in Fig. 18b). This is due to the fact that there are several major differences between the experimental setups used in these two studies, such as the working liquid, insulating material and its thickness and also different range of EW numbers (Fig. 18b).

CHAPTER 4: DYNAMIC WETTING LINE EFFECT ON MICROPUMP

Some of the materials used in this chapter have been previously published by The Royal Society of Chemistry and Springer: R. Shabani and H. J. Cho, “A micropump controlled by EWOD: wetting line energy and velocity effects”, Lab on a Chip 11 (20), 3401-3403, 2011.

R. Shabani and H. J. Cho, “Flow rate analysis of an EWOD based device: how important are wetting line pinning and velocity effects?”, Microfluidics and Nanofluidics, 2013, DOI: 10.1007/s10404-013-1184-y.

4.1 Introduction

In this chapter, the WLE effect on static contact angle (Fig. 15), and the WL velocity effect on dynamic contact angle (Fig. 16 and Fig. 17), investigated in chapter 3, are investigated as to dominant parameters influencing the operation of the micropump discussed in chapter 2 (Fig. 6). Walker et al. reported that considering the effect of the WLE on contact angle is crucial to predict the accurate time scale of the liquid motion; otherwise the calculated flow rate will be much higher than the experiments [29]. Dussan V. reported the relationship between dynamic contact angle and WL velocity in a forced wetting [27].

4.2 Micropump switch in operation

The liquid was supplied into the channel to form a droplet above the orifice. Once voltage is applied, the droplet begins flowing and the liquid moves forward in the channel (Fig. 19a-d). The meniscus position in the channel was measured versus time

for various droplet volumes using the similar initial liquid length in the channel and a voltage of 100V (Fig. 19e).

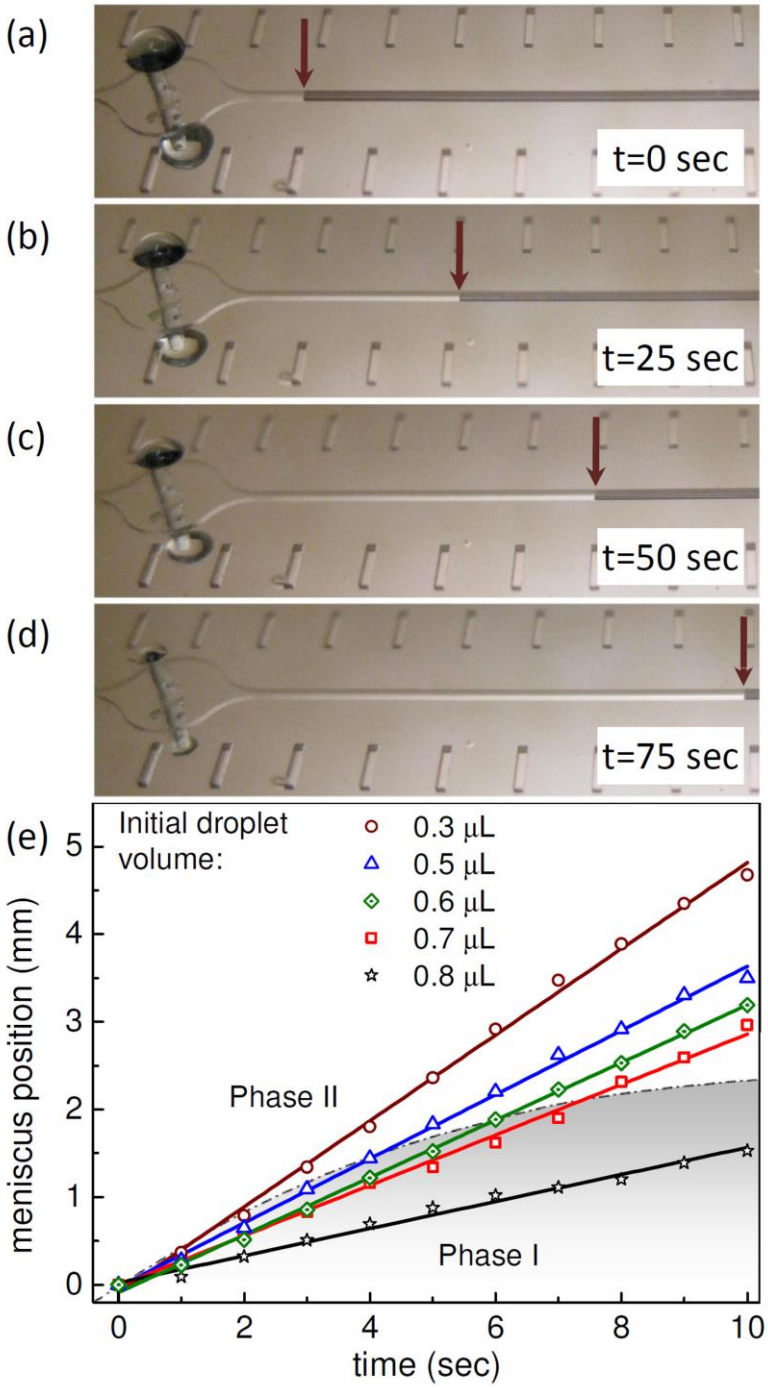

Fig. 19 (a- d) Time lapse sequences of the micropump in action. (e) Micropump flow rate for different droplet volumes. The phase I and phase II domains are shown as highlighted grey and white regions.

In a schematic of the setup, droplet and channel contact angles are shown as θ_D and θ_{Ch} respectively (Fig. 20a). Before applying the voltage between the electrodes, the liquid is stable with θ_D of 86º. The micropump operation can be divided into two phases. In phase I, the droplet's wetting diameter, a, remains constant until θ_D decreases to 80º (Fig. 20b and phase I in Fig. 20d). In contrast, in phase II, both the wetting diameter and the θ_D decrease as the liquid length in the channel, L_{Ch}, increases (Fig. 20c and phase II in Fig. 20d). In phase II the droplet has a θ_D of less than 80° and a wetting diameter, a, larger than the orifice size (500µm). Interestingly, the micropump flow rate remains almost constant despite the transition from phase I to phase II (Fig. 19e). The depicted transition was calculated from the initial droplet volumes and the transition droplet contact angle of 80°. The flow stops in the channel when the drop reaches the orifice edge.

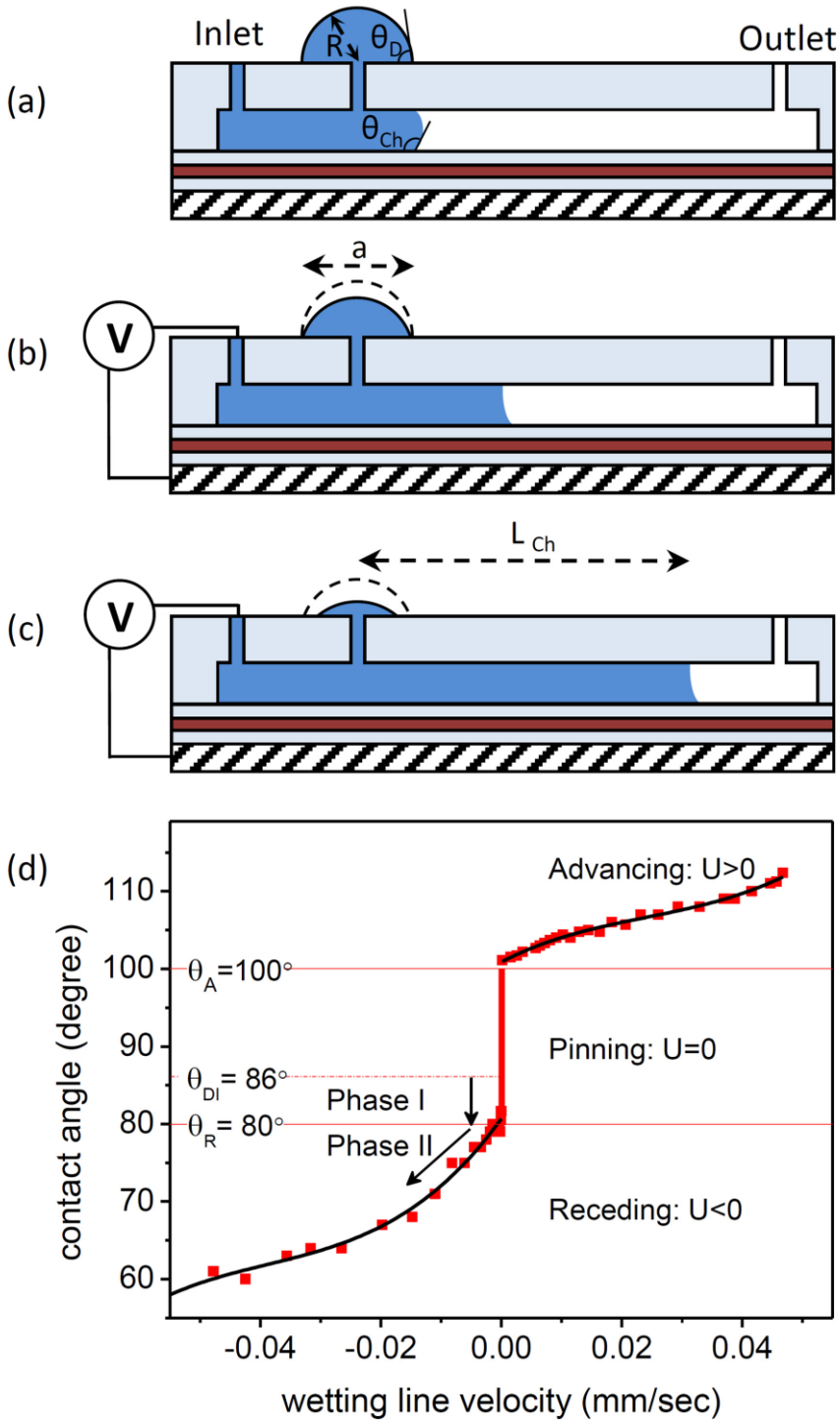

Fig. 20 Micropump operation: (a) the droplet is stable on top of the channel with the initial contact angle, θ_{DI}, of 86º. (b and c) By applying a constant voltage of 100V, the droplet is driven into the channel in phase I and phase II. (d) Droplet contact angle, θ_D, vs. its WL velocity, U.

The pressure gradient which is developed between the droplet and the liquid in the channel is utilized for driving the flow. The liquid velocity in the channel V is obtained from:

$$V = (P_D - P_{LM}) / C\mu L_{eff} \quad (8)$$

, where P_D and P_{LM} are the Laplace pressures of the droplet and the liquid meniscus in the channel, respectively, C is a geometrical constant, L_{eff} is the effective length (the sum of L_{ch} , orifice length, and other head losses) and μ is the liquid viscosity. By applying the voltage to the EWOD substrate, an electrical double layer is formed at the liquid-substrate interface. Similar to a capacitor the fringing electric field at the edge of the double layer has a component parallel to the substrate which could pull the double layer forward and therefore reduces θ_{Ch} and increases the meniscus radius of curvature. Since the other three channel walls are hydrophobic the decrease in θ_{Ch} is not enough to change the meniscus from convex to concave. However the Laplace pressure in the channel, P_{LM}, will be lower which results in a positive pumping pressure (Eq. (8)), and the liquid is driven through the microchannel.

The Young-Lippmann's equation predicts static contact angles of both θ_{Ch} and θ_D [24, 34, 70]. However, a constant value of contact angles θ_{Ch} and θ_D results in an unstable situation in which a slight difference between the channel pressure, P_{LM}, and the droplet pressure, P_D, may drive the droplet into the channel or vice versa (Eq. (8)). The stable formation of the droplet before applying the voltage in a wide range of droplet volumes and L_{Ch} is not in agreement with the static contact angle predicted in Young-Lippmann's equation. The direct observation of contact angles shows that the contact angle between the liquid, air, and the PDMS surface could change between a

highest and a lowest limit (advancing, θ_A, and receding, θ_R, contact angles respectively) due to the surface pinning induced by the defects on the surface [26] (Fig. 20d). In fact, the contact angle adjusts itself to resist the motion until it reaches either the lower or the higher limit. The pinning effect could explain the stability of the droplet before actuation. In order to accommodate this effect to justify the observations, the three-phase WLE should also be considered in Young-Lippmann's equation [26].

4.3 Wetting line velocity effect on micropump

In addition to the WLE, which explains the contact angle variation for a constant wetted area (phase I, Fig. 20b), the contact angle also depends on the velocity of the WL [27], when the wetted area is changing (phase II, Fig. 20c). The WL velocity is the rate at which the liquid WL with the substrate (in the case of the droplet, the circular line of the droplet's outer edge) moves on the solid surface.

When the drop is formed on top of the orifice its WL is advancing and θ_D is on the advancing region of Fig. 20d. As it becomes larger its WL velocity, U, decreases and θ_D is reduced to θ_A, which in this case is 100°. Ample time is given to the droplet for relaxation before starting the micropump (applying the voltage) during which θ_D decreases from 100° to 86°. By applying the voltage, the droplet flows into the channel and θ_D decreases from 86 to θ_R which in this case is 80° (phase I in Fig. 20d).

The pinning effect is also present inside the channel, evident by repeated short stops of the flow when the voltage is low. However, by increasing the voltage the pinning effect inside the channel decreases. The pinning effect becomes negligible at a working voltage of 100V, and the flow rate is stabilized.

Phase I ends when θ_D reaches 80° and for smaller contact angles, the droplet wetted area starts to shrink. In phase II the droplet wetted area is decreasing and θ_D is below θ_R. The magnitude of U increases as the droplet shrinks and the higher velocity results in a lower θ_D (phase II in Fig. 20d).

For a shrinking droplet with a constant θ_D the radius of curvature, R, is shrinking. However for a shrinking droplet with a constant wetted diameter, a, and decreasing θ_D, R increases. In phase II both the wetted diameter and θ_D are decreasing which have opposite effects on R. We have observed that in overall R in phase II is decreasing. The flow stops at the end of phase II when the droplet reaches the orifice.

4.4 EWOD voltage effect on micropump flow rate

In a second set of experiments, the low pinning regime (region III in Fig. 18b) was more closely studied by changing the micropump working voltage from 60V to 100V. The EWOD based micropump depicted in Fig. 6 was used as the test setup. An input droplet with an initial size of 1 mm was used for the measurements at different voltages. By applying the voltage the droplet was driven into the channel. The liquid meniscus position in the channel was measured versus time for each voltage (Fig. 21a, b).

Interestingly, the flow rate at low voltages (60V<V<100V) is completely nonlinear (Fig. 21b) and it changes drastically at different meniscus position inside the channel. This behavior is due to surface defects (located randomly inside the channel) which increase the contact angle and therefore reduce the flow rate. The influence of such defects seems to be lessened for higher voltages (e.g. at 100V) and hence such voltages are needed as the working voltage of the micropump, if a constant flow rate is desired. The meniscus position inside the channel versus time for different voltages are

calculated by a model based on WLE and WLV effects. This is discussed in more details in chapter 5.

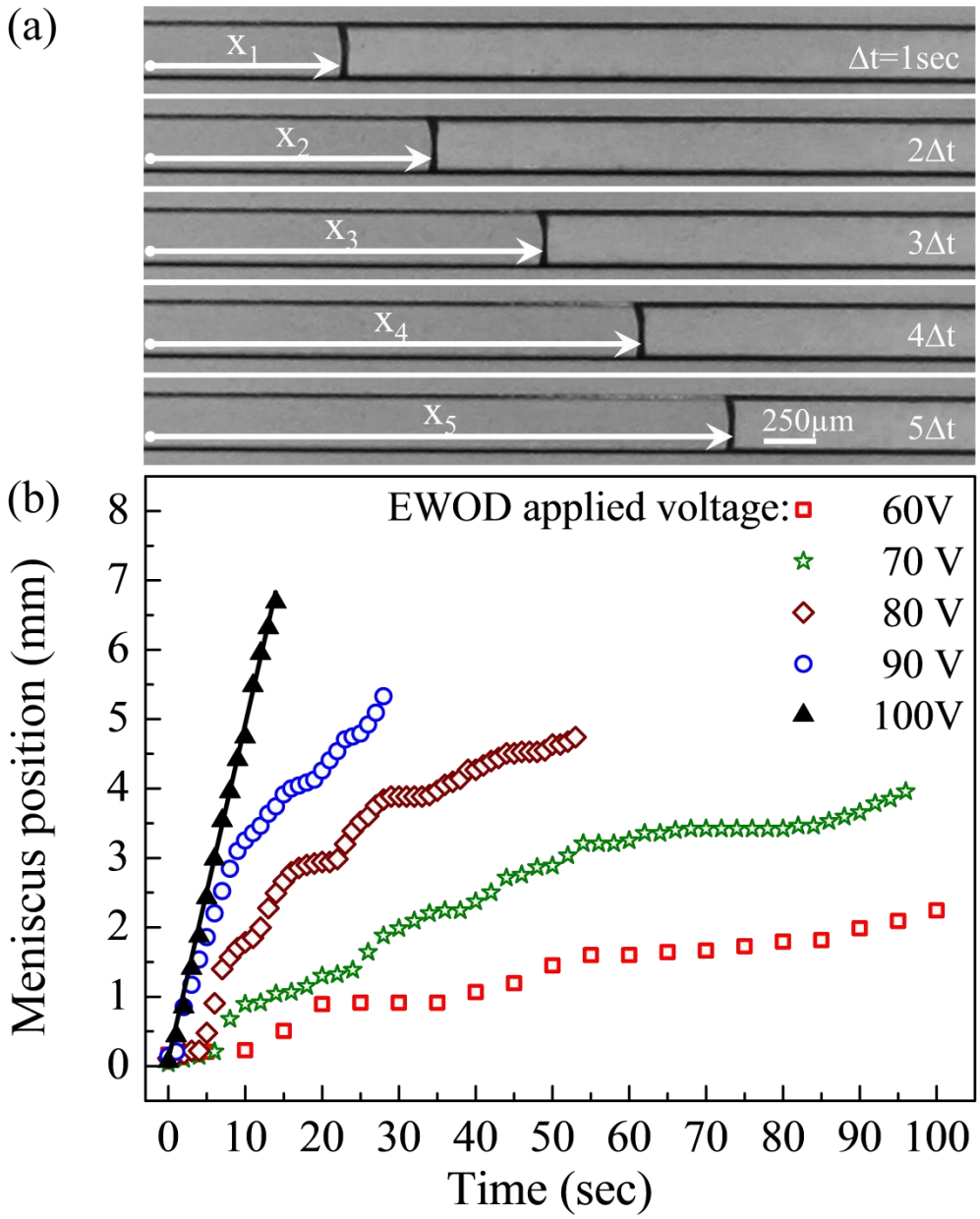

Fig. 21 EWOD voltage effect on flow rate (a) Top view pictures of the micropump's channel taken in every second show the advancing meniscus at 100V. (b) The micropump's meniscus position versus time for different voltages.

CHAPTER 5: MICROPUMP FLOW RATE ANALYSIS

Some of the materials used in this chapter have been previously published by Springer: R. Shabani and H. J. Cho, “Flow rate analysis of an EWOD based device: how important are wetting line pinning and velocity effects?”, Microfluidics and Nanofluidics, 2013, DOI: 10.1007/s10404-013-1184-y.

5.1 Introduction

In this chapter, a combined theoretical/experimental approach based on continuity and energy equations is developed to study a continuous flow induced by EWOD micropump demonstrated in chapter 2. An input droplet was used as a positive pressure source. By applying the voltage the contact angle is reduced at the bottom of the channel which results in a lower Laplace pressure inside the channel. Therefore, a positive pressure gradient is produced between the droplet and the meniscus. The droplet’s WL recedes as it shrinks into an orifice leading to the channel. The WL pinning and the WL velocity effects, discussed in chapter 3, need to be taken into account to describe the dynamic contact angles at the WLs: (i) the droplet’s receding WL, (ii) the advancing WLs of the liquid meniscus on the upper and side walls of the channel, and (iii) the advancing WL at the bottom of the channel with a reduced contact angle due to EWOD. These two effects are crucial to developing a physically-relevant model for the flow rate analysis (for more details see the discussion in chapter 4). This is due to the fact that the accurate estimation of the contact angles is necessary to calculate the induced droplet/meniscus pressure gradient [37], and subsequently the micropump’s flow rate.

5.2 Experimental assumptions

The EWOD substrate of the micropump consists of a silicon wafer spin-coated with a stack of three thin films of (i) polydimethylsiloxane (PDMS), (ii) spin on glass (SOG) and (iii) a second layer of PDMS, (Fig. 6). Silicon wafer is a conductive layer. SOG is an insulating layer with a thickness of 0.2μm and a dielectric constant of 3.9 (Pai 1987; Wang et al. 1997). The first PDMS layer (on silicon) was found to improve the quality of the insulating layer by covering the surface defects. The second PDMS layer is used as a hydrophobic layer with a thickness of 1.1μm. SU-8 mold on a different silicon wafer was used to cast a microchannel in a PDMS slab (soft lithography). The PDMS slab was bonded to the EWOD substrate to form a closed channel. A syringe pump was connected to the microchannel as shown in Fig. 6. The liquid flowed through the channel and then through a via-hole which has a bigger cross-section compared to the channel, forming a droplet on top of the orifice. The micropump's input droplet is stable with a contact angle of 86°. Only after applying a DC voltage between the silicon wafer and the steel pin (electrodes) the liquid will flow through the channel.

The input droplet is driven into the channel in two phases. In phase I, the droplet's wetting area remains constant until droplet's contact angle decreases to 80° due to pinning. Such phenomenon has been also observed for a passive micropump [9]. In contrast, in phase II, both the droplet's wetting area and contact angle decrease as the droplet is driven into the channel. The further decrease in droplet's contact angle is due to WL velocity effect [71]. The reported variable droplet's contact angle on untreated PDMS surface in chapter 3 is in agreement with the data reported in literature [9, 71]. These results are incorporated in this chapter for the analysis of the micropump constant flow rate.

The measured data for the receding WL (Stage C in Fig. 16b) is used to describe the variable contact angle of the shrinking droplet versus its WL velocity during the phase II of the micropump operation [71]. Also the experimental data depicted in Fig. 16c are used for the contact angle on the side and top walls of the channel, θ_{Ch} in the flow rate analysis.

The last data needed is the liquid contact angle on the bottom of the channel, θ_{EW}, upon applying a DC voltage of 100V. However, the direct observation of θ_{EW} from the side view of the PDMS channel is not feasible unlike the observation of θ_{Ch} from the top view. This is due to non-smooth and opaque surfaces when PDMS was cut on the sides. Moreover the contact angle calculated by Young–Lippmann's equation for a voltage of 100V could not be used since the pinning and WL velocity effect are present at the bottom of the channel (dynamic θ_{EW} at the advancing WL in the channel). Instead, θ_{EW} was considered as a fitting parameter and the validity of values obtained for θ_{EW} were justified by comparing with other experimental data, i.e. the contact angle should be smaller in the presence of EWOD as compared to θ_{Ch}.

5.3 Derivation of governing equations

A novel approach for flow rate analysis is introduced by taking a dynamic contact angle into account in writing energy equation for the system. This is an improvement over sophisticated commercial software, limited only to equilibrium Young contact angle [36], based on Young's equation.

Here we need to highlight that (a) the flow rate inside the channel is a function of the meniscus contact angle and (b) the contact angles themselves are a function of the flow rate. Therefore, a self-consistent solution could be obtained only using implicit

computational methods. The algorithm for this approach is developed following the continuity and energy equations and its physical implications are demonstrated. The proposed algorithm could be fitted to various microfluidic systems with different geometries for flow rate estimation. A numerical calculation was carried out using MATLAB. Some of the parameters used in the analysis are shown in the side and top views of the micropump schematic (Fig. 9a, and b). The micropump driving pressure, P_{MP}, derived in chapter 2 (Eq. (6)) is repeated below for the readers:

$$P_{MP} = \gamma_{wa}\left(\frac{2}{R_D} + \frac{\left((2h + w)\cos\theta_{Ch} + w\cos\theta_{EW}\right)}{wh}\right)$$

The total driving pressure in Eq. (6) should be equal to the viscous pressure loss in the channel, $h_f \rho_w g$. The channel head loss, h_f, is obtained from the Darcy-Weisbach equation to be $f\ L_{eff}\ U_{Ch}^2/(2D_H g)$, in which f is the friction factor, L_{eff} is the effective liquid length in the channel (the sum of L_{Ch}, orifice length, and other head losses), U_{Ch} is the liquid velocity in the channel, and D_H is the hydrodynamic diameter. The D_H of the rectangular channel with a width, w, and a height, h, is equal to $2wh/(w + h)$. The Reynolds number for the flow in the channel with an order of 1mm/s is calculated to be ~0.1 using D_H. Thus assuming a laminar flow in the microchannel, the friction factor will be $64/Re_{D_H}$. The relation between the micropump pressure, P_{MP}, and the liquid velocity in the channel, U_{Ch}, is expressed by:

$$U_{Ch} = P_{MP}/\left(8\mu_w L_{eff}(1/w + 1/h)^2\right) \quad (9)$$

Bond number measures the relative strength of gravity with respect to surface tension and is defined as $g\rho_w L^2/\gamma_{wa}$, where L is the characteristic length scale e.g. the

droplet's radius or the height of the microchannel. The bond number for the droplet with an order of size of 1mm is small (~0.1) and hence the gravity is neglected throughout the rest of the analysis.

The capillary number is the ratio of viscous force to the surface tension force acting across the WL and is defined as $\mu_w U_{Ch}/\gamma_{wa}$, where μ_w is the liquid's viscosity, and U_{Ch} is the WL velocity. The capillary number is calculated to be much smaller than unity (~ 10^{-5}) for water's viscosity of 1mPa.s and surface tension of 72mN/m and an order of WL velocity of 1mm/s. Thus the surface tension force dominates the inertial force.

The dimensionless EW number represents the ratio of the electrostatic energy to the surface tension and is defined as $cV^2/2\gamma_{wa}$, where c is the capacitance of the EWOD substrate and is calculated to be 10 μF/m^2 [80], and V is the applied DC voltage. The EW number for the EWOD setup is calculated to be 1 for the applied DC voltage of 120V. Therefore for the range of the applied voltages, a substantial contact angle decrease could be achieved at the WL in the channel.

5.4 Model 1 based on wetting line energy and velocity effects

Eqs. **(6**) and (9) were implemented to develop an algorithm for flow rate analysis based on the WLE and WLV effects (Model 1 WLE & WLV). The continuity equation implies that the rate of the shrinkage of the input droplet is equal to the liquid flow rate in the channel. The initial θ_D for the input droplet was assumed to be equal to the relaxed advancing contact angle at zero voltage which is 86° (Fig. 15b).

In phase I of the micropump, θ_D changes from 86° to 80° with a constant droplet wetted area due to the pinning. In Phase II, in which droplet's WL is receding, the data

from Fig. 16b is used to estimate θ_D for the receding WL of the droplet. The data in Fig. 17 is used to find $\theta_{Ch,}$ in phases I and II for the advancing WL in the channel. The liquid contact angle on the bottom of the channel, θ_{EW}, was obtained by flow rate analysis.

Since in one hand θ_{Ch} is a function of U_{Ch} (Fig. 17) and in the other hand U_{Ch} is a function of θ_{Ch} (Eqs. (6) and (9)), an implicit approach was used here to calculate θ_{Ch} based on the self-consistency of the results. In each time step a guess value for θ_{Ch} was chosen, and then U_{Ch} was calculated from Eqs. (6) and (9). However, it should be noted that the assumed θ_{Ch} and the value obtained for U_{Ch} should be in agreement with the data shown in Fig. 17. Therefore, the initial value for θ_{Ch} was modified until the calculated U_{Ch} shows a good agreement with the experimental data.

Fig. 22 shows an excellent agreement between the measurement and numerical values obtained by model 1 (WLE and WLV), using θ_{EW} of 82° for an initial droplet size ($2a_D$) of 1.06 mm. Fig. 22a shows the experimental and calculated values for the radius of droplet wetted area, a_D and droplet contact angle, θ_D and also calculated values for droplet radius of curvature, R_D, versus time. The transition from phase I to phase II is marked with vertical dashed line at 4.8 sec. In Fig. 22b, P_D and P_M are shown as the droplet is driven into the channel. The droplet pressure decreases in phase I from 271 Pa to a minimum of 267.3 Pa and increases again in phase II. However, the driving pressure which is the difference between the P_D and P_M increases monotonically to overcome the increasing viscous loss. In Fig. 22c the estimated liquid meniscus position versus time is compared to the measurement data. The calculated data exhibits the linear behavior as the experimental data.

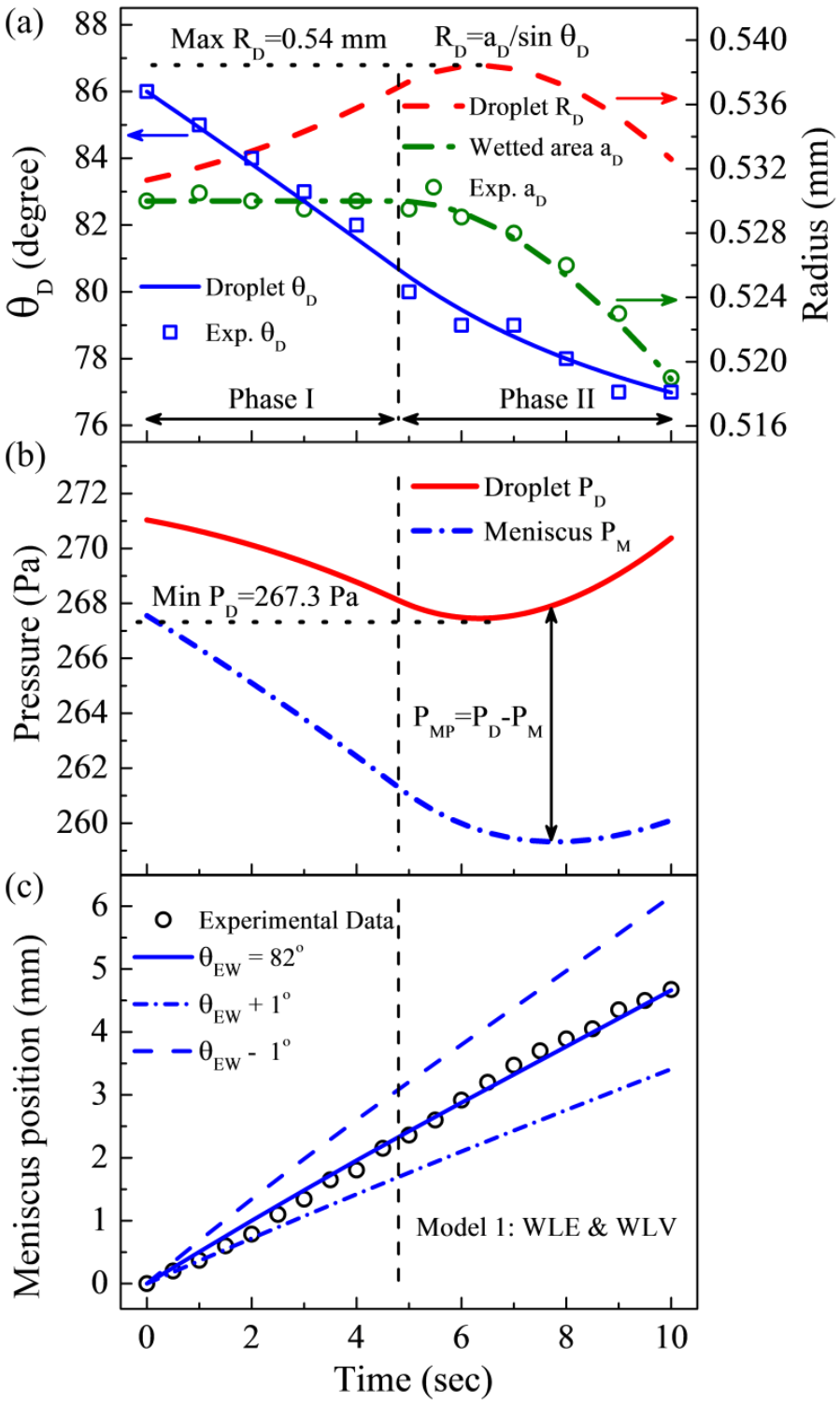

Fig. 22 Model 1 WLE and WLV numerical values for (a) Droplet's θ_D, a_D, and R_D versus time. Measurement data for θ_D and a_D are plotted. (b) P_D and P_M vs. time. (c) Meniscus position versus time. Circles are the data and solid line is the best fit to the data. Dashed line and dot-dashed line show the effect of a small change in θ_{EW} (±1°) on the convergence of the fit.

In phase I of micropump operation, θ_D is reduced (Fig. 22a), resulting in an increase in R_D and subsequently a decrease in the droplet pressure (Fig. 22b). However, phase II is more complex since both a_D and θ_D are changing (Fig. 22a). Therefore the change in P_D and P_M is non-monotonic in phase II. Interestingly, the meniscus pressure seems to follow the droplet pressure and therefore the driving pressure of the pump (the difference between P_D and P_M) remains small over time (Fig. 22b).

This phenomenon is the underlying reason for the constant flow reported for this micropump. Since the size of the meniscus in the *micro-scale* channel is much smaller than the droplet's free surface, small changes in θ_{Ch} (±0.1°) could change P_M sufficiently to compensate for the change in P_D (Fig. 22b). Therefore, the variation in micropump's pressure induced by the shrinking input droplet would result in small variation of meniscus contact angle. Since θ_{Ch} and U_{Ch} are linked through WL velocity effect, such small changes in θ_{Ch}, also imply negligible changes in the liquid velocity in the channel which explains why the liquid velocity and therefore the flow rate remain nearly constant. The dynamic contact angle of the meniscus in the channel is the dominant factor determining the flow rate according to this analysis.

5.4.1 Droplet size effect

The meniscus velocity in the channel is higher for smaller sizes of the droplet [71]. The numerical values obtained by model 1 WLE and WLV are in good agreement with the experimental data for the meniscus position in the micropump's channel for different

sizes of the droplet (Fig. 23). The analytical fits to the data follow a similar linear behavior as the experimental data.

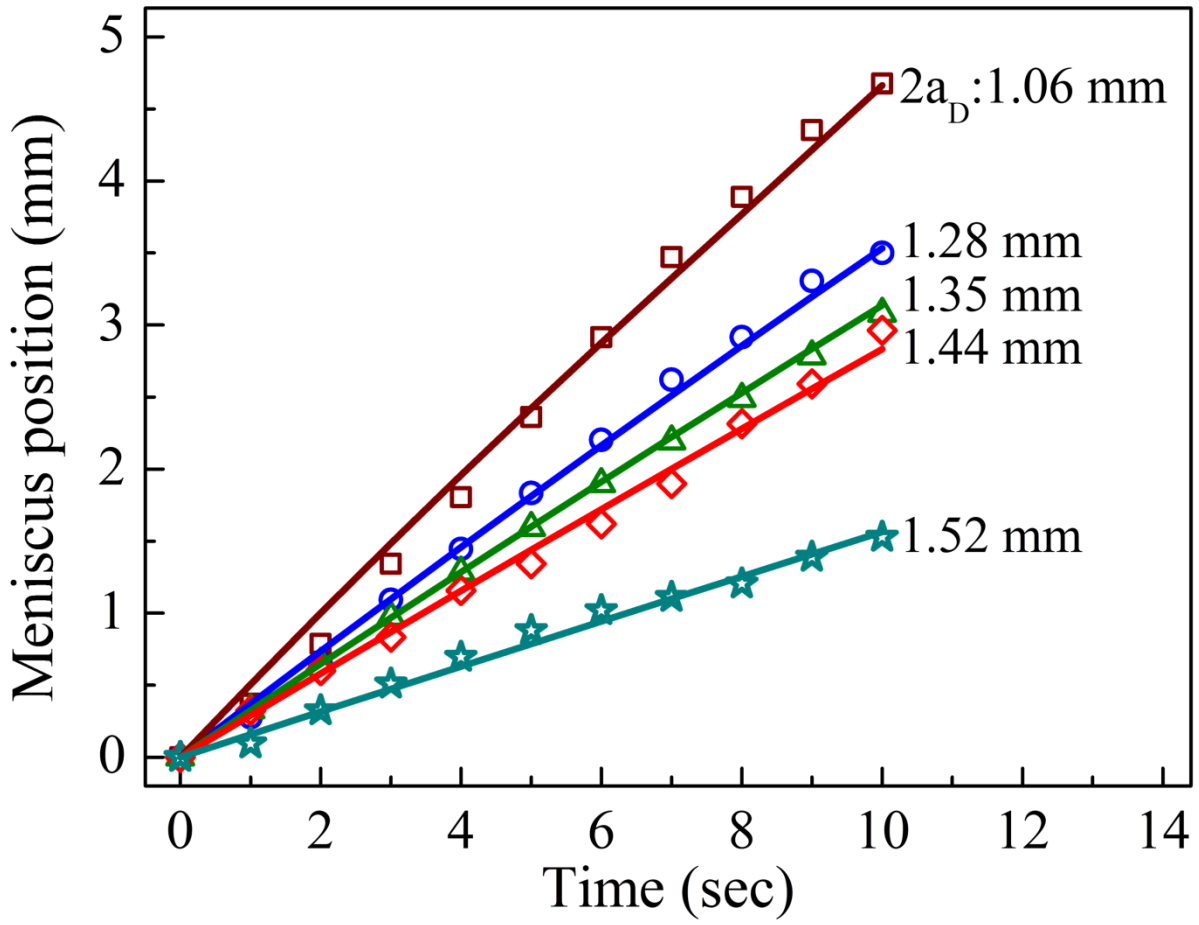

Fig. 23 Model 1 WLE and WLV predicting the meniscus position versus time for different diameter of the droplet wetted area, $2a_D$. Markers are measurement data and solid lines are the best fits to the data.

5.4.2 EWOD voltage effect

In a second set of experiments, the low pinning regime (region III in Fig. 18b) was more closely studied by changing the micropump working voltage from 60V to 100V. By applying the voltage the droplet was driven into the channel. The liquid meniscus

position in the channel was measured versus time for each voltage (Fig. 24). Since the location of surface defects cannot be measured inside the channel, any attempt to model such a complex system could only aim to obtain the effective average flow rates but not the local values. Fig. 24 shows the experimental and calculated meniscus positions versus time at different voltages. A better agreement is obtained between the calculated and the measured data when the EWOD voltage is high enough to suppress the effect of local surface defects on dynamic contact angle.

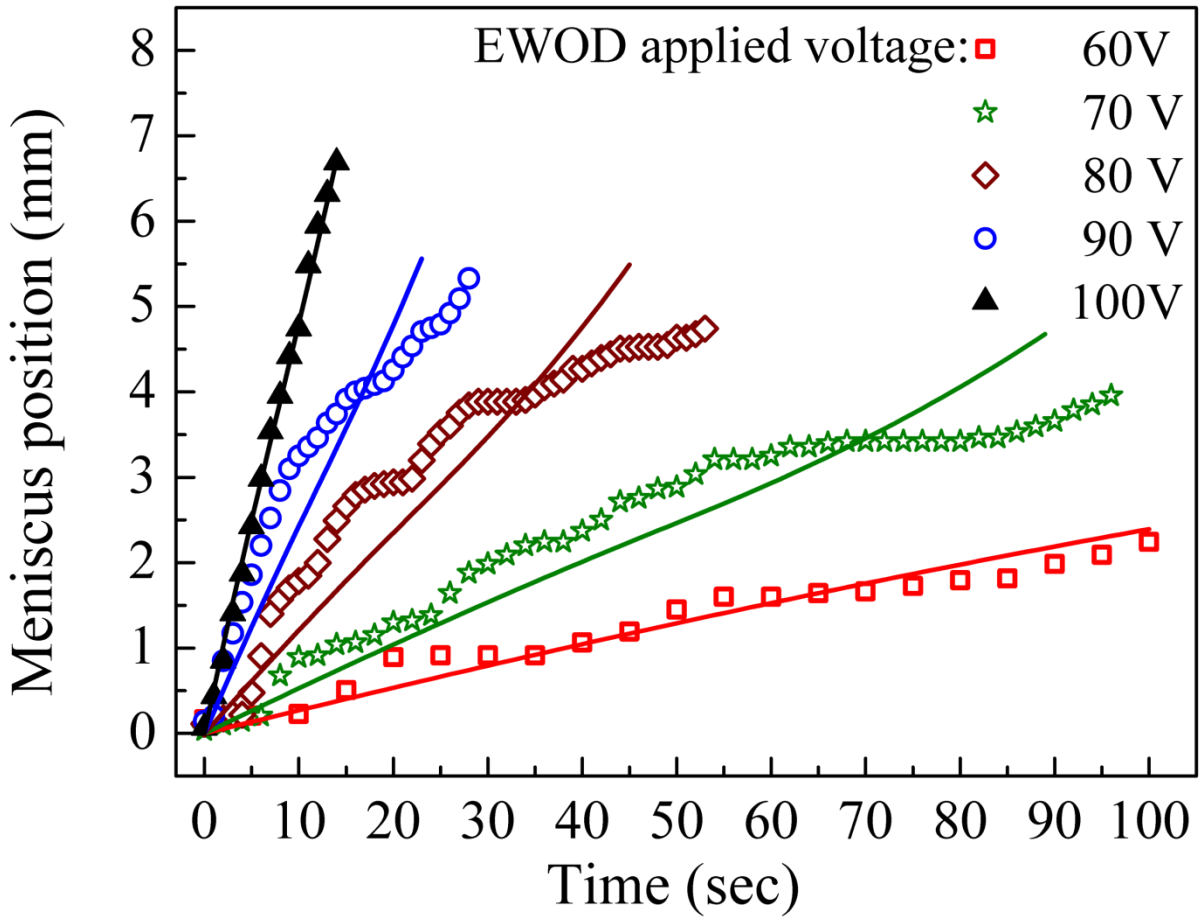

Fig. 24 Model 1 WLE and WLV predicting meniscus position versus time for different voltages. Markers are measured data and solid lines are the best fits to data.

The calculated θ_{EW} for different voltages (Fig. 25) is higher than the relaxed advancing contact angle at a similar voltage (Fig. 18b). This is in agreement with the concept of dynamic contact angle which shows larger values for larger advancing meniscus velocities.

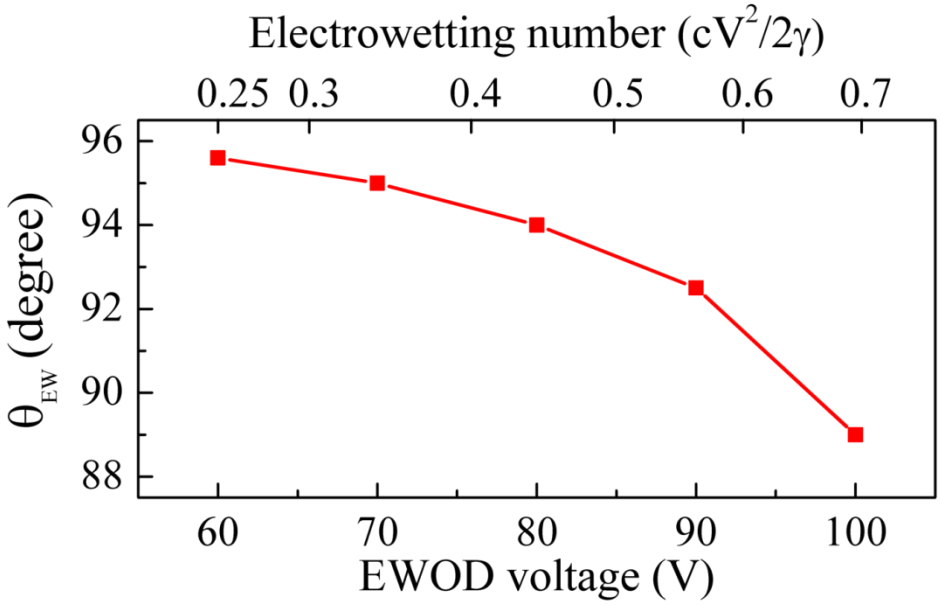

Fig. 25 Numerical values for θ_{EW} versus EWOD voltage, calculated by model 1 WLE & WLV.

5.5 Comparison with wetting line energy model and Young contact angle model

In order to highlight the importance of considering the WLE and WLV effects on the moving WL, two further models (models 2 and 3) were developed and compared to the comprehensive model 1 shown in the previous section.

The model 2 is based on the WLE effect [26], and does not include the WL velocity effect on contact angle (Model 2: Young-Tadmor). In model 3, neither the pinning effect

nor the WL velocity effect was considered and the contact angle was assumed to be equal to the equilibrium Young contact angle (Model 3: Young). The assumptions and the contact angle values for each model are reported in Table 2 for comparison.

Table 2 Experimental assumptions and dynamic contact angles for models

	Assumptions	θ_D (Phase I)	θ_D (Phase II)	θ_{Ch}	θ_{EW}
Model 1	Comprehensive (WLE & WLV)	86°→80° (a_D CONST)	Fig. 16b	Fig. 17	82°
Model 2	Young-Tadmor (only WLE)	86°→80° (a_D CONST)	80°	100°	88°
Model 3	Young equation (Young contact angle)	86°	86°	86°	109°

The numerical values for the liquid meniscus position in the channel for an initial diameter of the droplet wetted area, $2a_D$, of 1.06 mm are plotted for model 1(Fig. 22c) and for models 2 and 3 (Fig. 26a and b respectively). The values obtained for the θ_{EW}, for models 1 to 3, are tabulated in Table 2. In model 3 based on equilibrium Young contact angle (Fig. 26b), a large gap exists between the measured and the predicted flow rate [29, 39]. Model 2 provides a better fit to measured data (Fig. 26a) as compared to the model 3 by taking to account the pinning effect. The predicted flow is significantly improved by including the WL velocity effect in model 1 (Fig. 22c). The sensitivity of the calculations to θ_{EW} is also investigated. In model 1, if θ_{EW} is changed by 1°, the estimated flow in the channel will slightly vary, while maintaining its linear behavior (Fig. 22c), unlike models 2 and 3 which are very sensitive to small changes in θ_{EW} (Fig. 26b, c). This also shows the accuracy of the estimated θ_{EW} by model 1. It is expected that the

contact angle is reduced at the bottom of the channel due to EWOD [70]. The value obtained for θ_{EW} (82°) is reasonable since it should be smaller than, θ_{Ch}, with a value of 104°, due to EWOD.

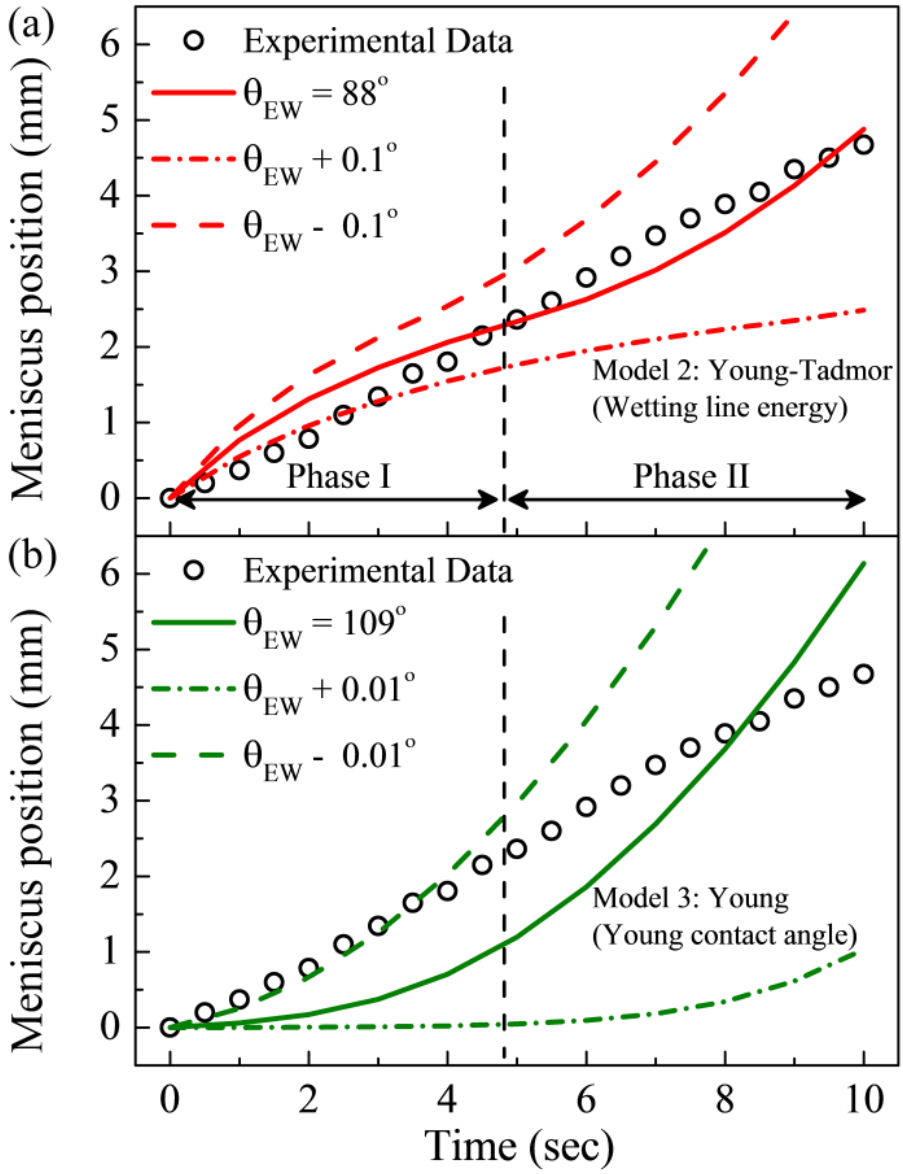

Fig. 26 Meniscus position versus time for (a) Model 2 (Young-Tadmor) and (b) Model 3 (Young). Circles are measurement data and solid lines are the best fits to the data. Dashed lines and dot-dashed lines show the effect of a small change in θ_{EW} on the convergence of the fit.

Although the comprehensive model 1 utilizes several nonlinear experimental equations, its estimation of flow rate provides an excellent agreement with the observed constant flow rate. Such comparison shows the importance of taking both the WLE and the WLV effects into account for an accurate and realistic flow rate analysis.

CHAPTER 6: DROPLETS ON LIQUID SURFACES AND TRIPLE CONTACT LINE

Some of the materials used in this chapter have been previously published by American Institute of Physics: R. Shabani, R. Kumar, and H. J. Cho, “Droplets on liquid surfaces: dual equilibrium states and their energy barrier”, Applied physics Letters, 102, 184101, 20132013.

6.1 Introduction

The formation of floating aqueous droplets on the free surface of immiscible liquids has application in digital microfluidic devices [49], as well as material transportation and mixing in lab on a chip [50, 51]. The floating non-coalescent (NC) water droplets were first observed by Reynolds on the water’s free surface [55]. Although describing the floating droplet has been of interest, to our knowledge a general solution has not been provided for the dual equilibrium states [51, 59, 60]. Further, while the non-coalescence of a droplet on the free surface of the same liquid is widely studied, the studies using immiscible liquids are scarce.

6.2 Stable configurations of floating droplets

An oil phase (FC-43, 3M) at 25^{o}C with a surface tension, γ_{oa}, of 16 mN/m and a density, ρ_o, of 1860 kg/m^3 was used as a base medium for formation of floating droplets. A droplet of water at room temperature (25^{o}C) with a density, ρ_w, of 997 kg/m^3 was released on the free oil surface using a high precision needle connected to a syringe

pump. The water droplets are released due to a gravity driven pinch-off from the tip of the needle [60]. The stable configuration of the droplet at the air-oil interface depends on the height from which the droplet is released and the surface tension of the three phases. If the droplet is released from within a range of height, it will not rupture the free surface as it does not have sufficient momentum. Instead, it will rest on the stretched free surface which is deformed by the weight of the NC droplet (Fig. 27a, c).

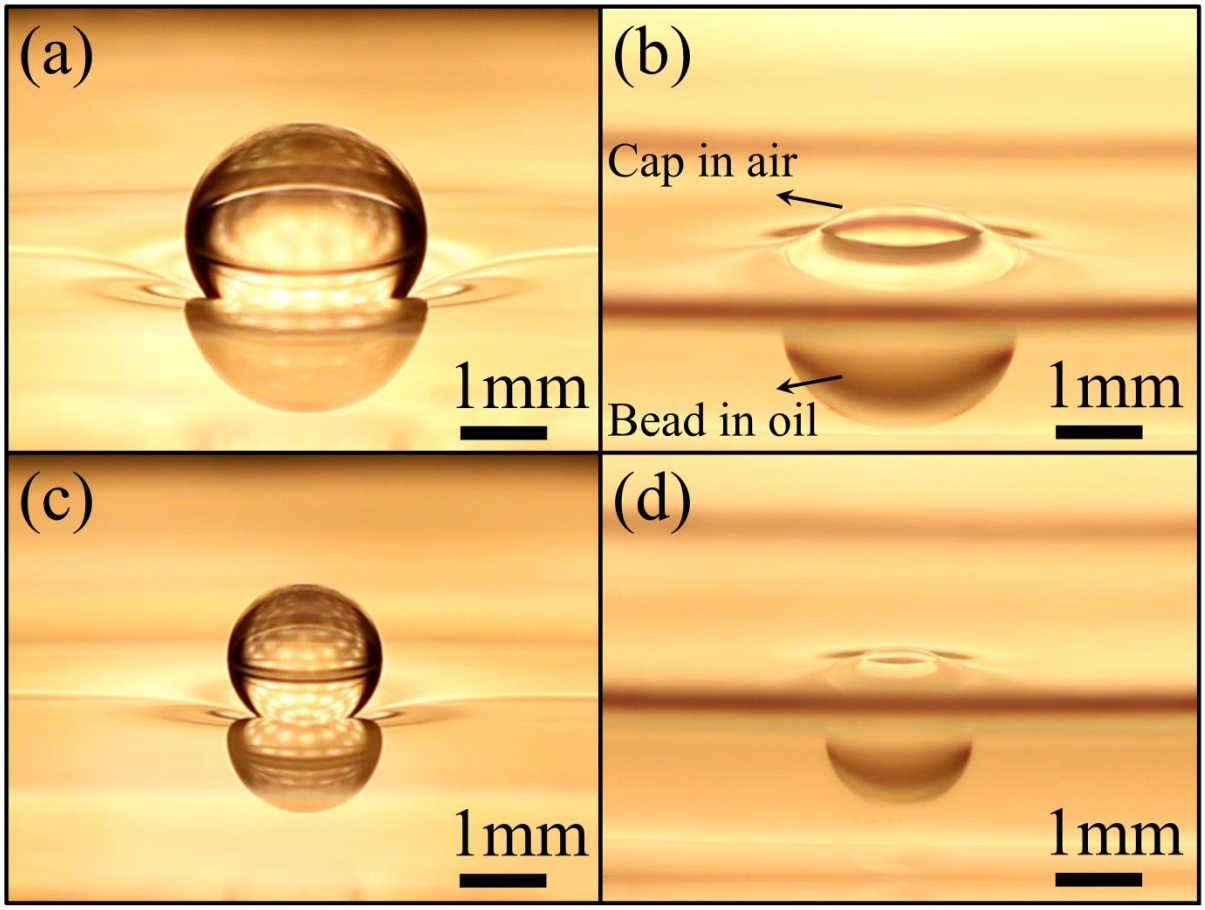

Fig. 27 Stable configurations of aqueous droplets at oil-air interface: (a) NC droplet resting on a stretched and deformed free surface (b) C/B droplet with TCL (c, d) the effect of the droplet size on the deformation of the free surfaces.

Bond number (defined as $g\rho_w R_D^2/\gamma_{oa}$) for a droplet radius, R_D, with an order of 1mm is small (~0.1) and hence a uniform pressure is assumed inside the droplet. The droplet is assumed to be spherical from Laplace pressure equation [51]. By increasing the droplet release height, H_R, it gains more energy to rupture the free surface and becomes submerged. However the droplet is held up by the buoyancy force ($\rho_o > \rho_w$) and becomes stable at the oil-air interface. The water droplets shown in Fig. 27b and d have two parts of cap in air and bead in oil (C/B droplet). A triple contact line (TCL) is formed at the circular perimeter of the intersection of the spherical cap and bead.

6.2.1 Probability of formation of non-coalescent droplets versus Weber number

The probability of formation of NC droplets was studied as a function of the droplet's H_R. Different gauge needles (35G to 23G) were used to release droplets of different sizes. A hundred droplets were released from each needle and weighed to calculate the equivalent droplet radius, R_D, for each needle [54]. The probability of formation of the NC droplets (percentage of the observed NC droplets to the total droplets released) is measured as a function of H_R for different droplet sizes. Since it is more appropriate to use dimensionless parameters [54], Fig. 28 shows the results as a function of Weber number which is the ratio of the droplet kinetic energy to the base medium surface energy, ($4\rho_w g H_R R_D)/\gamma_{oa}$. It could be used to show whether the released droplet from a specific HR, has sufficient kinetic momentum to overcome the liquid surface energy and break up its free surface. As Weber number increases, breaking up the free surface becomes easier for the droplets, and the probability of formation of NC droplets becomes zero. However, the complexity of NC droplet

formation could not be captured by We number only. Fig. 2 shows that for a similar Weber number the probability increases as RD decreases. This is due to the fact that Weber number compares the droplet kinetic energy with the surface energy of the base medium, which is not the only obstacle that a falling droplet faces to break the surface. Other energy terms such as the gravitational potential energy of the displaced base medium and energy used for wave formation should be taken into account as discussed in the next section.

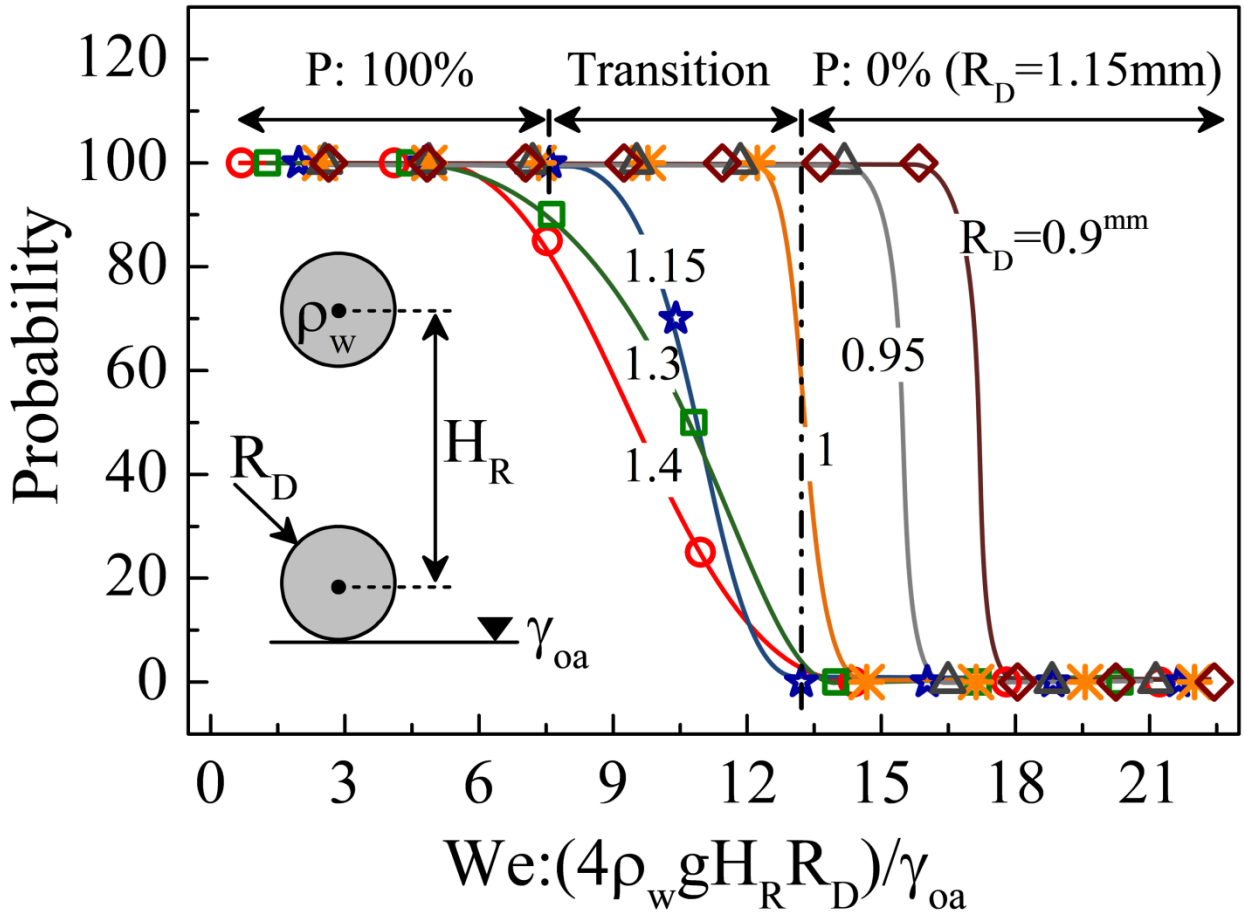

Fig. 28 The probability of formation of NC droplets versus Weber number obtained for different droplet's radii, R_D.

For each droplet size there is a transition region, in which the probability of forming NC droplets changes from 100% to 0% by increasing H_R (Fig. 28). This transition region

is wider for higher R_D and becomes sharper as R_D decreases. NC droplet formation in transition region shows a statistical nature which is more pronounced for larger droplets. This might be understood in terms of wave energy dissipation and the time required for damping the initial oscillation of droplet surface upon pinching off from the needle. While a small droplet quickly attains its stable shape (spherical) the lager droplet may not have enough time to dissipate the facial waves which may affect the NC to C/B transition.

Here it should be mentioned that even the droplets that survive the first impact and stay on the surface (NC droplets), will at some point coalesce with the oil surface and sink down to C/B configuration [54, 55]. This observation demonstrates that the latter has a lower energy and thus is more favorable while the NC configuration is metastable.

6.2.2 Non-coalescence of droplets due to thin film of air

Several studies have been focused on the physical origin of NC droplets in different experimental setups with inclined or horizontal free surfaces of base mediums and also various surrounding mediums with different surface tensions, densities and viscosities [51, 54-58, 81]. A thin film of air between the droplet and the free surface is believed to be responsible for the formation of NC droplets by preventing the two liquids to wet [54, 81-84].

The existence of such film has been confirmed in literature using different methods such as the mirror-like reflection, an infinite electrical resistance [85], and no material transfer between the droplet and the base medium [54]. This is also obvious in the case of miscible liquids in which the droplet should make contact and mix with the base

medium if there was no air gap between them. The air layer thickness was reported to be about 10μm [51, 85], much larger than the van der Waals attraction range (10nm)[54]. The air film's slow drainage postpones droplet coalescence [82], due to the lift generated by the lubrication effect of the flowing air film [57]. However, the effect of the air film is merely limited to separating the two surfaces and it does not bring any external forces into the system. At last the purity of the base liquid's free surface and the surrounding medium from dust particles is essential in stability of the NC droplets [55, 56].

6.3 Energy analysis and prediction of stable equilibrium states

Energy analysis was done separately for two observed configurations, since the transition from NC to C/B is not continious and the energy is not a well behaved function during the transition. Therefore, two different sets of parameters were defined to describe the geometries of the two observed configurations (Fig. 29a, b).

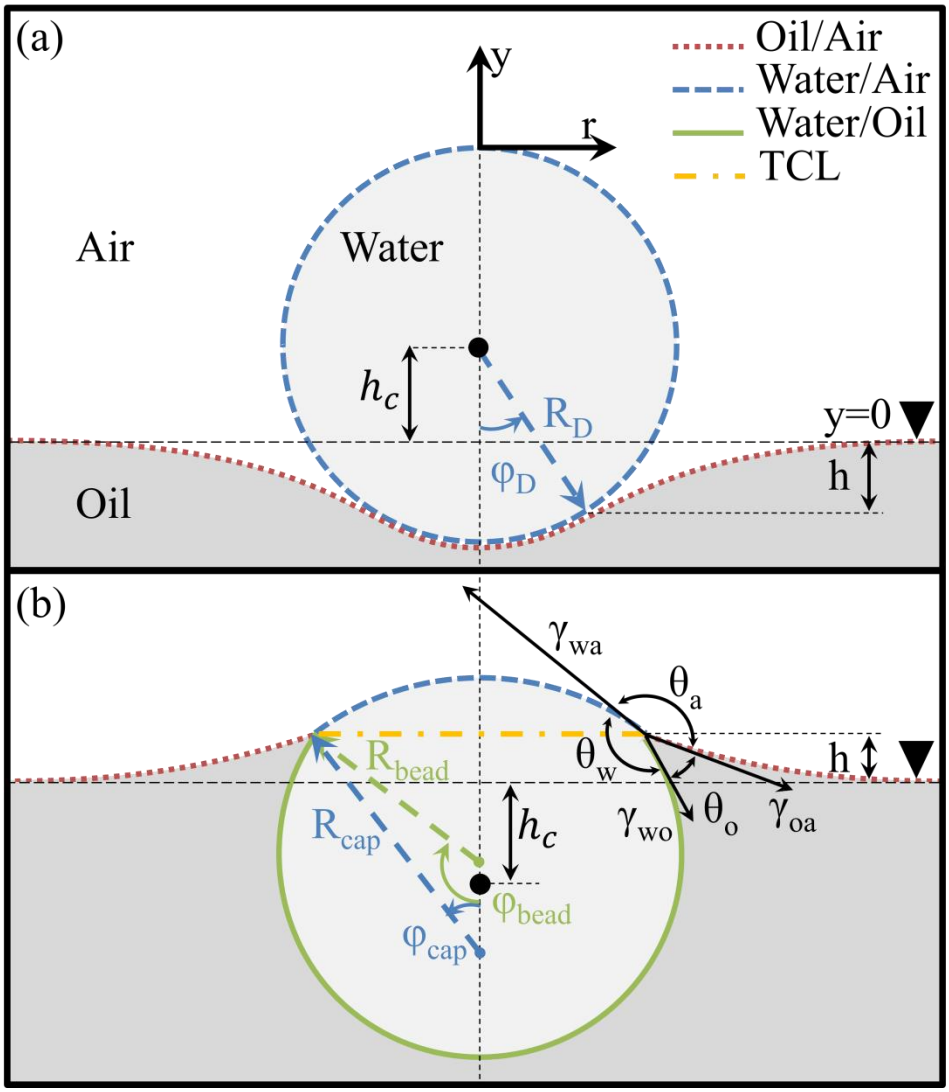

Fig. 29 Physical and geometrical parameters used in energy analysis of (a) NC droplet and (b) C/B droplet configurations.

The ratio of the radii of curvature of the cap and bead (R_{cap} and R_{bead} respectively) is proportional to the ratio of surface tension of water in contact with air and oil (γ_{wa} and γ_{wo} respectively) due to uniform Laplace pressure in the droplet [49]. γ_{wa} and γ_{oa} are known to be 72mN/m and 16mN/m respectively at 25°C. The Interfacial tension between water and FC-43, γ_{wo} was estimated to be $56.5 \pm 0.5\ mN/m$ using a method shown by Fox [86]. The three surface tension satisfy the Neumann's inequalities, which

means none of the surface tension between any pair of fluids exceed the sum of the other two [87]. If the Neumann's inequalities are not satisfied, a TCL will not be formed between the three phases [87]; and one of the phases will be fully submerged in one of the two other phases (fully submerged configuration) [49, 87]. The radius of the cap's circular base area, $R_{cap} \sin \varphi_{cap}$, is equal to the radius of the bead's base area, $R_{bead} \sin \varphi_{bead}$. The droplet volume is constant and is equal to the sum of the cap and the bead volumes. The net force per unit length of TCL has to be zero in a stable configuration and therefore knowing the three surface energies, and using Neumann's triangle concept, three contact angles of θ_a, θ_o, and θ_w (defined inside air, oil, and water respectively) are found.

The total energy of both floating droplet configurations, E_{net}, is the sum of the gravitational potential energy of (i) the water droplet, U_D, and (ii) the displaced liquid volume of the base medium, U_{DL}, as well as (iii) the total of the surface energies of the interfaces between each two phases, E_S:

$$E_{net} = U_D + U_{DL} + E_S \quad (10)$$

For the NC droplet, φ_D and for the C/B droplet, φ_{cap} were changed as the independent variables. The droplet's vertical position varies as φ_D for NC droplet (φ_{cap} for C/B droplet) changes. Assuming that the pool of the base medium is large, the Young-Laplace equation for an axisymmetric problem (in the cylindrical coordinates) was used to describe the free surface profiles of the base medium, in both configurations [51, 60, 87, 88]. The Young-Laplace equation is a relation between the hydrostatic pressure difference across the oil-air interface and its local mean curvature:

$$\rho_o g y = \gamma_{oa}\left[\frac{d^2y/dr^2}{(1+(dy/dr)^2)^{3/2}} + \frac{dy/dr}{r(1+(dy/dr)^2)^{1/2}}\right] \quad (11)$$

,where y and r are the height and the radial distance of a point on the free surface profile in cylindrical coordinates (Fig. 29a, b).

6.3.1 Calculation of liquid free surface profile

In the NC droplet configuration, an inflection point on the free surface profile exists in which its second derivative, $\ddot{y}$, changes its sign from positive to negative as *r* increases. Since the lower part of the droplet's profile with a radius of R_D, has a positive $\ddot{y}$, it starts to loose contact with the free surface's profile at this point (Fig. 30a). The droplet's inflection angle, φ_D measures the angle between the bottom of the droplet and the inflection point (Fig. 30a). The depth of the inflection point from the height of the free surface (far from the droplet) is *h*. In the C/B droplet configuration, the TCL's height from the height of the free surface is *h* (Fig. 30b). The cap angle, φ_{cap}, is the angle measured from the cap's top point to TCL. An iterative procedure in a MATLAB code was utilized to find the key parameter of *h* for both configurations using Eq. (11) with the boundary conditions shown in Fig. 30.

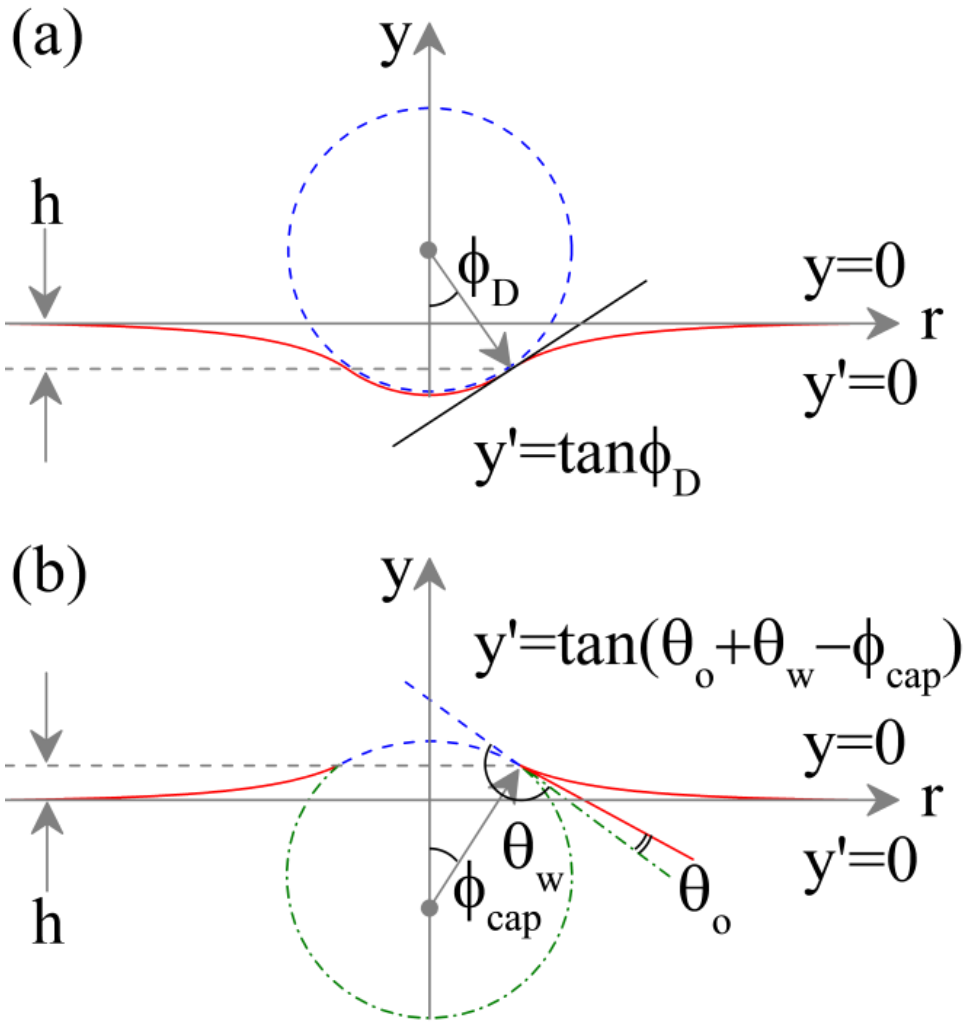

Fig. 30 The calculated oil's free surface profiles and the boundary conditions used in *h* estimation in (a) NC droplet configuration and (b) C/B droplet configuration.

In NC droplet configuration, φ_D was changed from 0 to 90 degrees to find the equilibrium state, thus the first derivative of the free surface profile, dy/dr equal to $\tan\varphi_D$ was changed from zero to infinity. Therefore dy/dr and d^2y/dr^2 were substituted with dr/dy and d^2r/dy^2 respectively in Eq. (11) and a similar algorithm was implemented to find h, for higher values of dy/dr.

6.3.2 Droplet's size effect on liquid surface deformation

Using the calculated profile of the free surface, the area of the deformed oil-air interface and the volume of the displaced base medium and finally E_{net} are calculated. As expected, the energy analysis predicted a minimum of E_{net} (equilibrium state) for each configuration. The MATLAB code outputs were imported to Pro/E to generate the three-dimensional images of a floating droplet at the oil-air interface in both equilibrium configurations. These images depicted in Fig. 31 show good agreement with the pictures taken from floating droplets with similar sizes, for both configurations in Fig. 27. As expected, smaller droplets deform the surface to a less extent as compared to larger ones (Fig. 31c, d). φ_D for NC droplets and φ_{cap} for C/B droplets were measured for R_D of 0.9mm to 1.4mm (needle gauges of 35G to 23G). A good agreement between the experimental data and the values predicted by energy analysis were obtained (Fig. 31e). The gravity contribution as compared to that of the surface tension force becomes negligible at small droplet size limit ($R_D \rightarrow 0$), due to the scaling effect. Therefore the energy analysis results in $\varphi_D=0$, for a NC droplet but a non-zero φ_{cap}, for a C/B droplet $(\pi-\theta_a)$ when R_D approaches zero.

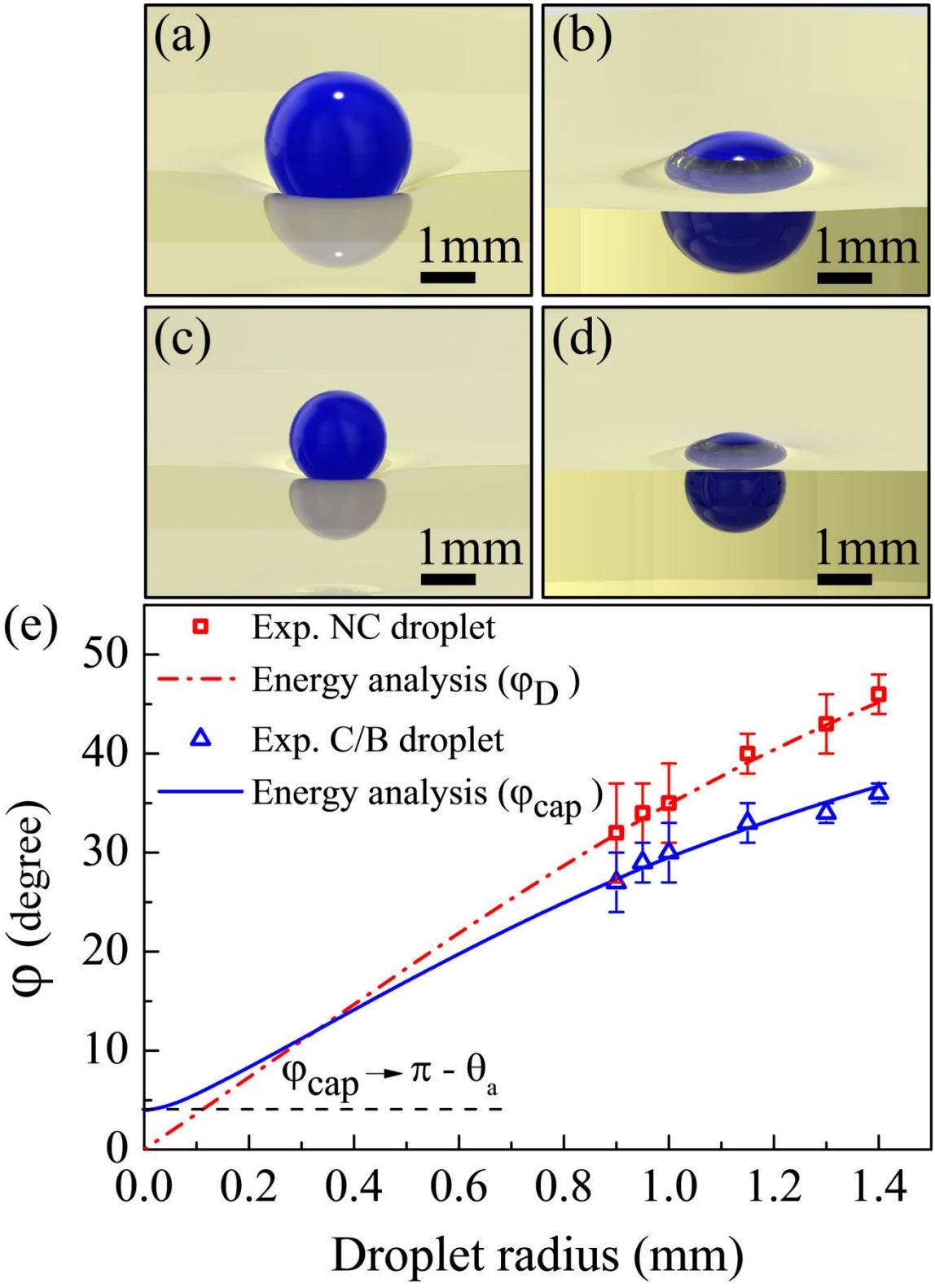

Fig. 31 Energy analysis simulation of both equilibrium states: (a) NC droplet and (b) C/B droplet (c, d) the effect of droplet size on the deformation of the free surface (e) φ_D for NC droplets and φ_{cap} for C/B droplets versus droplet radius.

6.3.3 Force analysis

To further confirm the results obtained by energy analysis, force analysis was also conducted [89, 90]. The states of the droplet in different vertical positions are called the mechanically enforced stationary states and could be achieved by using a hypothetical external force which could compensate for the net vertical force acting on the droplet [89, 90]. A mechanically enforced state is an equilibrium state only when the external force needed to achieve a stationary state is zero. For a floating droplet in a stable equilibrium state with the minimum E_{net}, the net force exerted on the droplet, F_{net} must be zero. F_{net} consists of the weight of the droplet, F_W, the buoyancy force, F_B, and the surface tension force, F_S.

$$\vec{F}_{net} = \vec{F}_B + \vec{F}_W + \vec{F}_S \quad (12)$$

The surface tension force is exerted on a NC droplet from the stretched free surface along a circular line passing through the inflection point (Fig. 32a). In case of C/B droplet the surface tension force is exerted on the droplet from the deformed free surface along the TCL (Fig. 32b). The buoyancy forces for NC and C/B droplets were obtained by calculating the displaced oil volumes (grey parts of the droplets in Fig. 32a and b respectively).

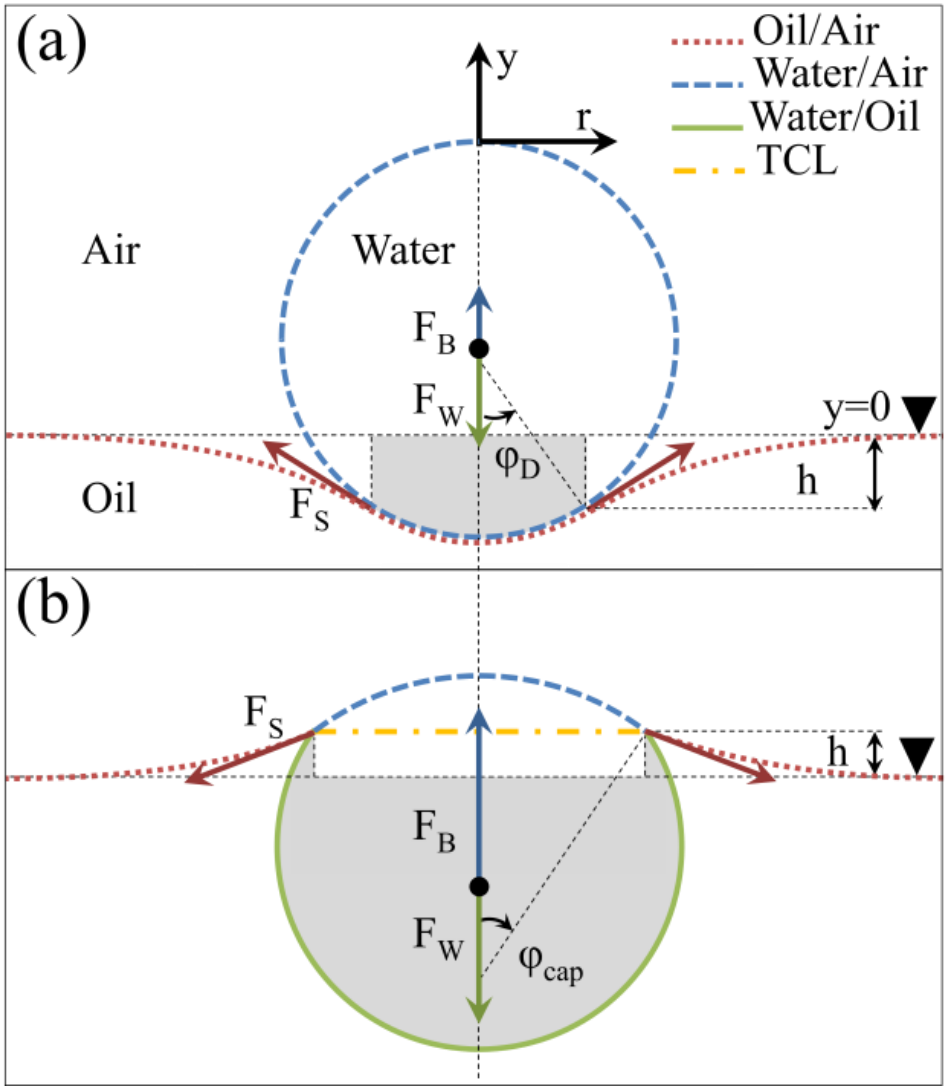

Fig. 32 The free body diagrams of (a) NC droplet and (b) C/B droplet. Arrows show the surface tension force, F_S, the buoyancy force, F_B and the droplet's weight, F_W.

A perfect agreement was obtained between the two methods and similar values for equilibrium states were found (Fig. 33a, b). In NC droplet configuration, an equilibrium state was predicted in which F_{net} was calculated to be zero (Eq. (12)) for a φ_D of 35° and E_{net} (Eq. (10)) was obtained to be minimum. In C/B droplet configuration, similar results were shown for a φ_{cap} of 30°.

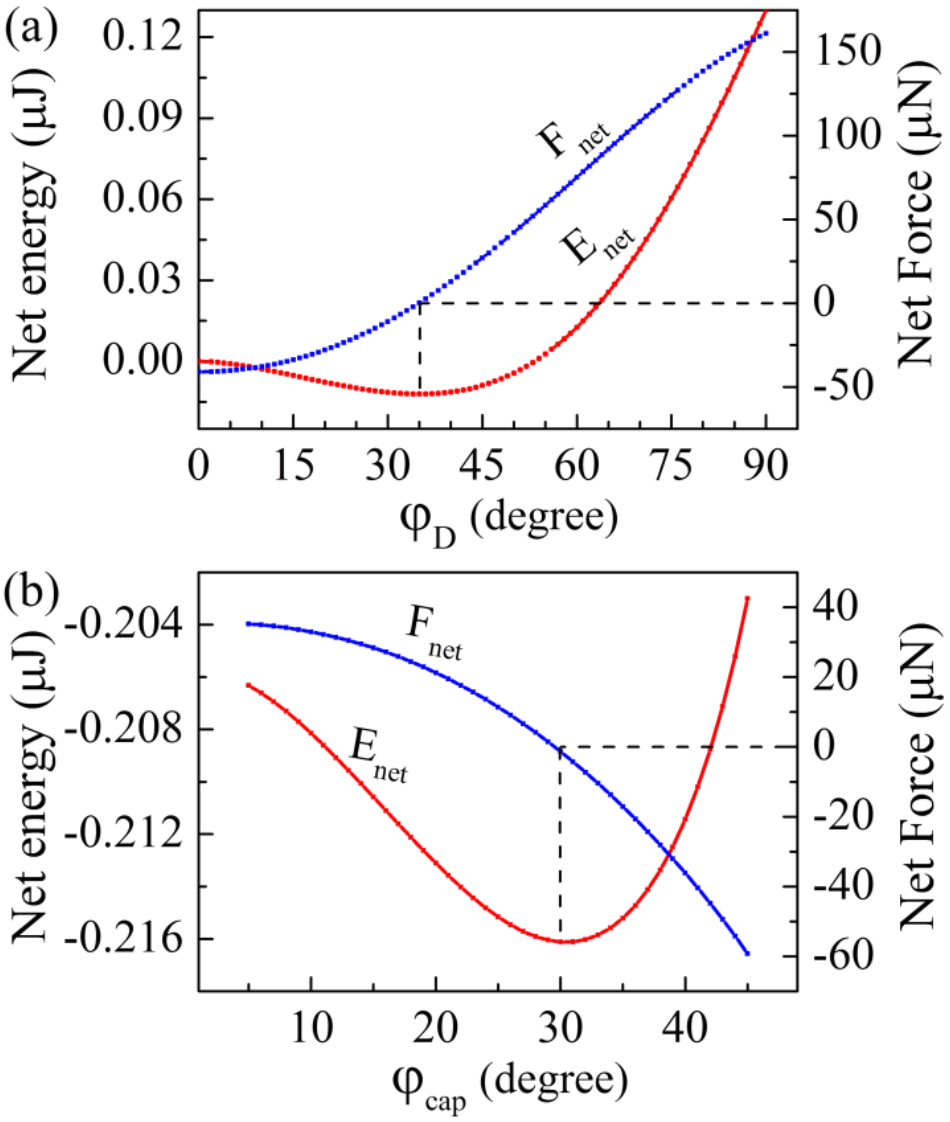

Fig. 33 E_{net} and F_{net} for a droplet with R_D of 1mm plotted for (a) φ_D for NC droplet and (b) φ_{cap} for C/B droplet.

6.4 Estimation of energy barrier between dual equilibrium states

As it was mentioned before if the droplet's kinetic energy is not enough to puncture the oil surface it will form the NC configuration. Interestingly, the energy analysis could be utilized to estimate the energy barrier that the droplet should

overcome to puncture the surface and reach the more stable C/B configuration. E_{net} divided by droplet's weight, w_D was plotted versus the height of the center of the mass of the droplet from the free surface, h_c (Fig. 34a). The energy reference point was chosen as state I in which the droplet is right on top of the free surface without deforming the oil-air interface. If the droplet has enough kinetic energy it will pass the first equilibrium point (state II) and reach the largest possible surface deflection (state III in Fig. 34b) where φ_D is 90^o (supporting surface tension force, F_S, is vertical).

After this point the droplet breaks the oil surface and sinks to state IV in C/B configuration. Finally by dissipating the extra energy in a damped oscillation between states IV and VI, it will settle down in the more stable state V (Fig. 34c). Therefore the energy barrier to achieve C/B configuration is the energy difference between state III and state I. The highest release height for which the NC droplets are formed with a probability of 100%, $H_{R,1}$, should be equal to E_{net} of state III divided by w_D (Fig. 34a).

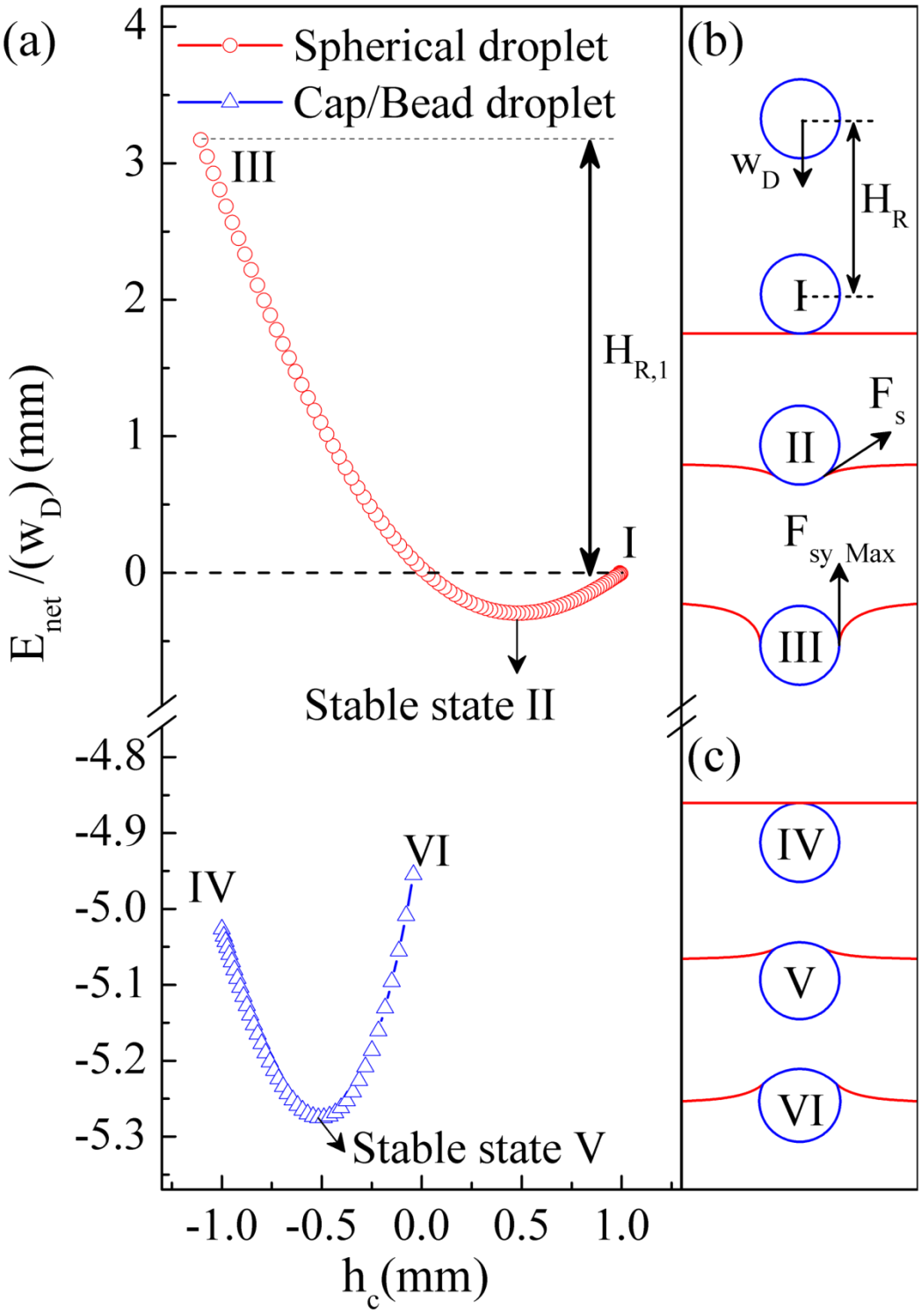

Fig. 34 The transition between the floating droplet's stable equilibrium states with a R_D of 1mm (a) E_{net} divided by w_D versus h_c (b) NC droplet in states I to III (c) C/B droplet in states IV to VI.

However, by correlating the calculated $H_{R,1}$ with the measured $H_{R,1}$ for different R_D (Fig. 35), it was found that consistently a lower value is obtained as compared to the experiment. Since the calculated value is the theoretical upper limit, the higher value obtained in experiment shows that other phenomena resulting in energy dissipation should be considered [84]. The formation of capillary waves at the oil surface, and also the longitudinal waves inside the base medium created by the droplet impact could carry away part of the droplet's kinetic energy [81, 85].

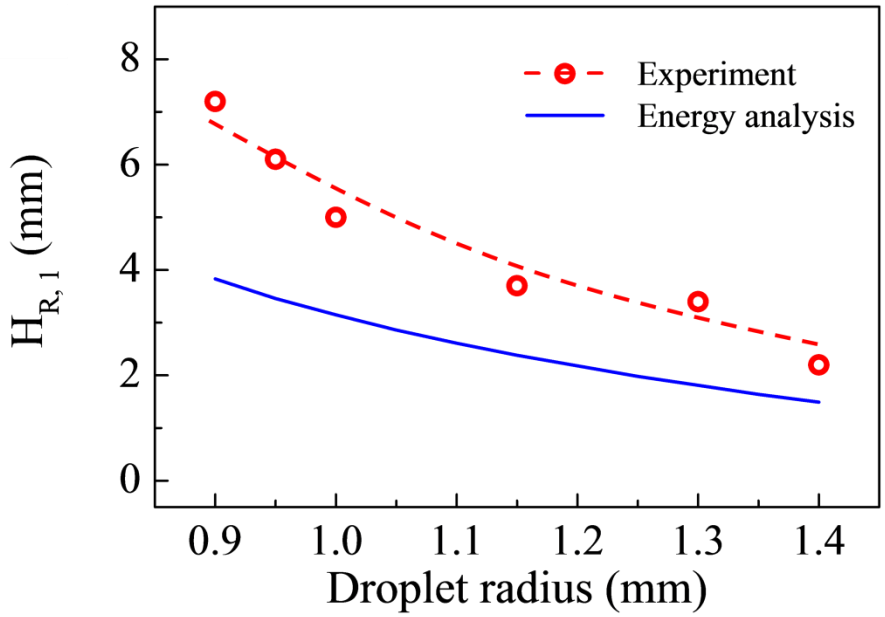

Fig. 35 Highest release height to form NC droplets with a probability of 100%, $H_{R,1}$, for different droplet's radius, R_D.

Interestingly, it was found that the thickness of the oil base affects $H_{R,1}$ which not only confirms the creation of waves but also shows that the reflection from the bottom of the container may affect $H_{R,1}$. Therefore in this study a thick layer of oil was used where the reflected wave has no effect on the stability of the droplets. Further study is required to investigate the wave reflection phenomena.

6.5 Non-dimensional analysis of liquid surface deformation

Further the effect of the droplet size on its stability was studied by calculating E_{net} for different R_D of NC and C/B droplets. For the NC droplet, E_{net} has a minimum at a particular φ_D for all the droplet's R_D (dot-dash line in Fig. 36a). The minimum E_{net} decreases as the droplet size increases, thus a bigger NC droplet is stable with a lower energy. A similar size effect is shown for a C/B droplet (Fig. 36b).

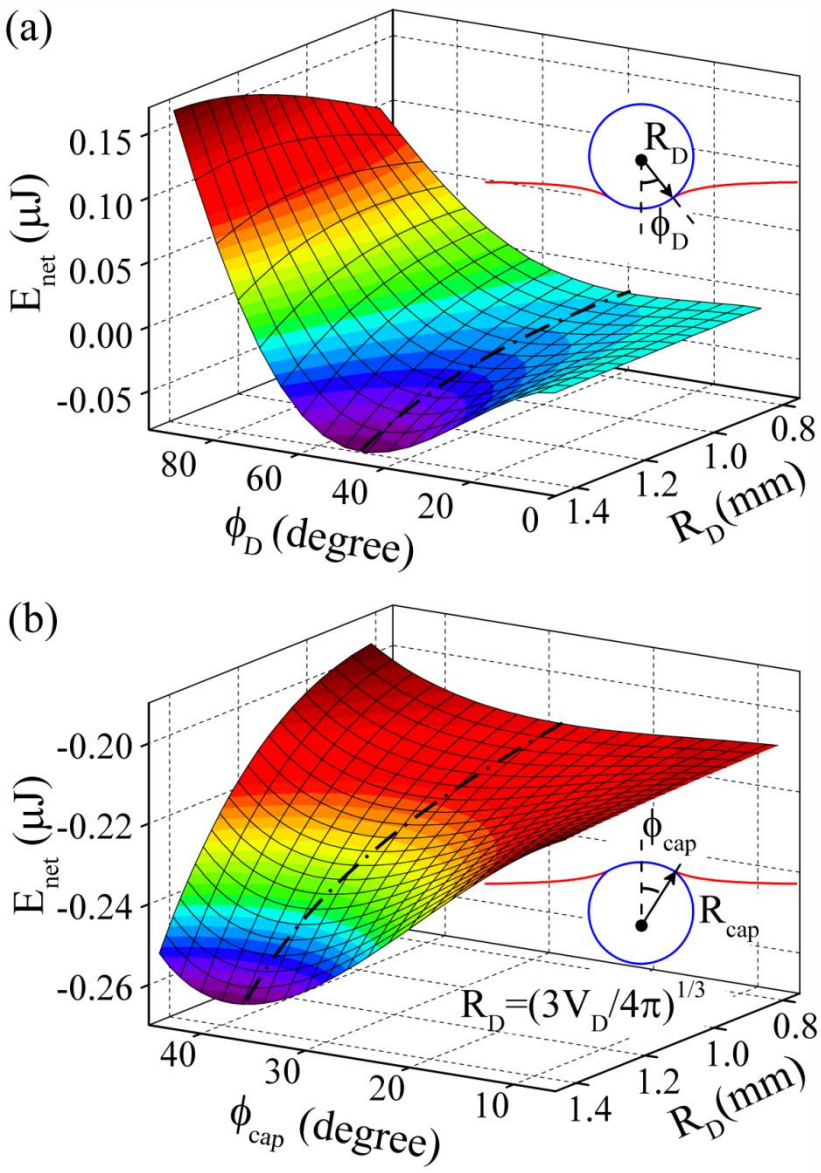

Fig. 36 E_{net} versus R_D and (a) φ_D for a NC droplet and (b) φ_{cap} for a C/B droplet. The dot-dash lines show the minimum E_{net} decreases by increasing R_D.

Based on the force and the energy equations (Eq. (10) and (12)) two non-dimensional parameters of ρ_o/ρ_w and the inverse of Bond number, Bo^{-1}, were introduced. The non-dimensional h_c/R_D, is calculated by the energy analysis and plotted versus the two non-dimensional groups of parameters (Fig. 36c). This parameter represents the deformation of the free surface, which as expected is less for larger Bo^{-1} andρ_o/ρ_w.

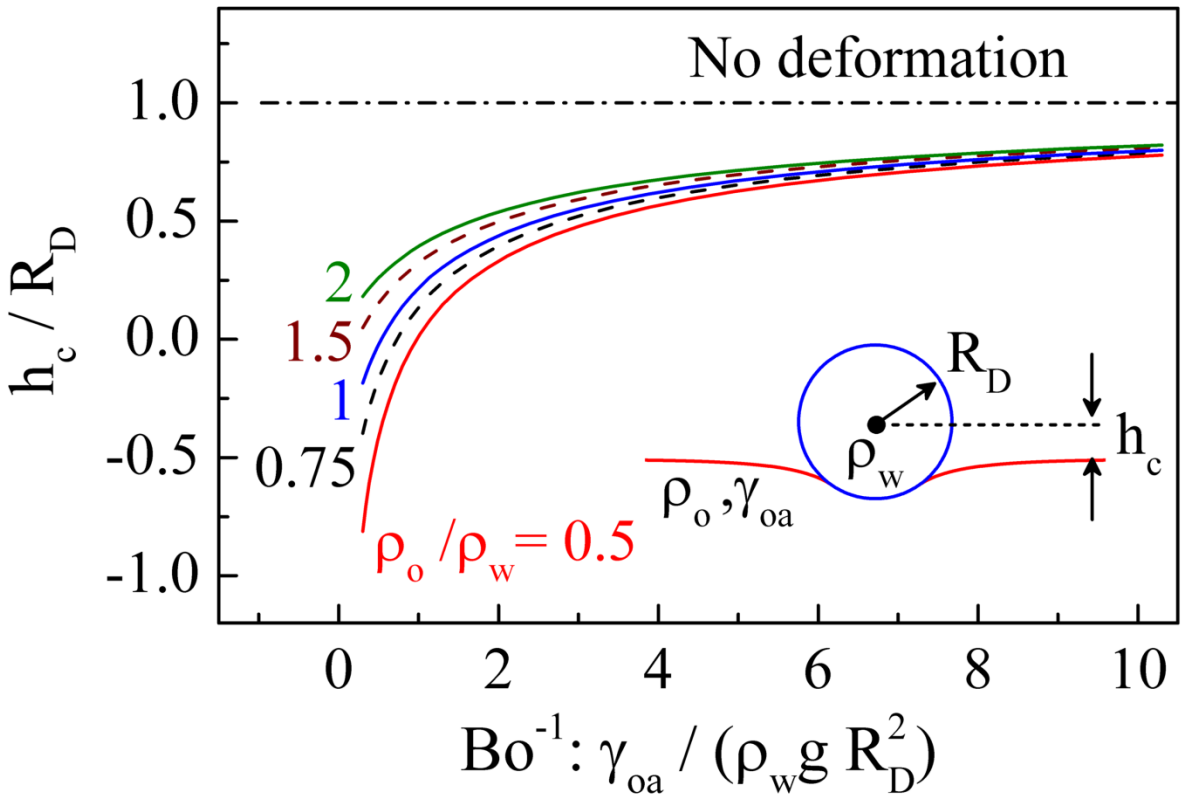

Fig. 37 Oil's free surface deformation factor, h_c/R_D, versus the non-dimensional parameters of Bo^{-1} and ρ_o/ρ_w obtained from the force balance and energy equations.

CHAPTER 7: CONCLUSIONS

In this dissertation, both experimental and theoretical studies were conducted to explain physical phenomena observed at an interface formed between two fluids and a solid phase (wetting line), and an interface between three fluids (triple contact line).

In the first part of this dissertation, the pressure gradient induced between the droplet and the meniscus in the channel was used to design a micropump with no moving parts and the fabricated device itself was used as a test platform to study various interfacial phenomena. Altering the surface tension by changing the electric potential in EWOD (electrowetting on dielectric) was introduced as an efficient method for flow regulation, which provides on demand flow on/off capability. The micropump was made using one mask fabrication process and could be operated at preset voltages. The EWOD substrate was evaluated using four parameters: capacitance, hysteresis contact angle, saturation contact angle, and onset voltage. The non-mechanical valving method based on switching EWOD voltages and the on-demand pumping method with respect to various droplet sizes were proposed and explained. The predicted driving pressure from the EWOD valve model was correlated to the measured data for the liquid flow rate in the channel. The developed micropump is simple in its design and fabrication and yet provides the on-demand supply function with much desired features such as short response time, low power consumption, no fluid leakage, no dead volume, disposability and biocompatibility.

A model based on the forced wetting was developed for explaining the behavior of the actuated input droplet. In the first phase the droplet wetting area is constant while contact angle is decreasing and in the second phase the droplet contact angle and the

wetting area are decreasing simultaneously. A systematic approach was utilized to show the importance of taking account of the dynamic contact angle and explain the behavior of microfluidic devices that involve a moving WL. Dynamic contact angles observed in both the source droplet and the meniscus inside the microchannel of the EWOD pump were studied. Further, the WL-related phenomena were comprehensively studied, since the device performance was strongly affected by contact angle hysteresis, WLV effect, and EWOD.

Some of the major experimental findings were as follows: (1) a mode switch in micropump operation originates from the contact angle hysteresis; (2) the dynamic contact angle based on the magnitude and direction of WLV in a microscale channel is responsible for constant flow rate; (3) EWOD reduces the contact angle for voltages larger than an onset voltage and its effect saturates at higher voltages, and (4) EWOD could reduce the pinning effect using DC voltages.

A flow rate analysis of the EWOD micropump, based on the continuity and energy equations by implementing the aforementioned experimental observations, was conducted. The predicted flow rate was in excellent agreement with the measured constant flow rate of the micropump.

The lower pinning effect at higher working voltages leads to a relatively higher and constant flow measured in the channel. The effect of EWOD voltage on the flow rate was modeled, and the numerical values obtained by comprehensive model, based on WLE and WLV effects, for the dynamic θ_{EW} were verified against the relaxed advancing contact angles at a similar voltage.

Simpler models, based on Young's equation (equilibrium Young contact angle) and Young–Tadmor equation (incorporating the pinning effect on contact angle) were developed for comparison. They showed disagreement between the numerical and measured flow rates, and resulted in an unphysical behavior for the system. Such examples demonstrate the importance of inclusion of the aforementioned wetting-line energy and wetting-line velocity effects to accurately model the flow rate, in particular for the micropump investigated in our study, and in general for any devices utilizing the Laplace pressure gradient.

In the second part of this dissertation, the interface between three fluids was studied, by forming floating droplets on liquid free surfaces, and the relevant physical phenomena are described.

Floating aqueous droplets were formed at oil-air interface and two stable configurations of (i) non-coalescent droplet and (ii) cap/bead droplet were observed. General solutions for energy and force analysis were obtained for both configurations, and were shown to be in good agreements with the experimental observations. The energy barrier obtained for transition from configuration (i) to (ii) was correlated to the droplet release height and the probability of non-coalescent droplet formation. It was shown that energy dissipation through wave phenomena should be taken into account.

Based on the force and the energy equations two non-dimensional parameters of ρ_o / ρ_w and the inverse of Bond number, Bo^{-1}, were introduced. A general solution was developed for the dual equilibrium states of the floating droplets. Also the transition region for the probability of formation of non-coalescent droplets as a function of Weber

number was shown. A dimensionless parameter was defined to represent the oil free surface deformation and was calculated by the energy analysis.

The data represented by non-dimensional groups of parameters could be used as a guideline to design experiments to form various sizes of floating droplets for the effective droplet manipulation.

Future work

The EWOD micropump devised in this work, could be used as a key component in handling small amount of aqueous samples. Its ability to work with small input droplets makes it suitable for application in the field of analytical chemistry, biology and medicine in which a limited amount of dose needs to be supplied with good accuracy. In some of the applications, small amounts of biological samples or chemical reagents are introduced into the chip in the form of an input droplet, for chemical reactions and biochemical processes such as immobilization, labeling and detection. The features of the fabricated EWOD based micropump such as low fabrication cost and minimal mechanical complexity makes it suitable for disposable biochips.

Other techniques for controlling the surface tension could be proposed as a driving method in droplet based devices for continuous flow in the microchannel due to its favorable scaling effect. In designing such devices the wetting line phenomena which were comprehensively studied in this work could work as a guideline to find the appropriate range of the change in surface tension for inducing the flow. Such methods for controlling the surface tension include a temperature gradient in thermocapillary and an electric potential gradient in electrocapillary. The ability to control the surface

wettability could be useful to design various types of flow-on-demand devices for practical applications.

In one application the EWOD micropump, with its simple design, could be used as a sample loading component in a disposable biochip. For example, it could be used to substitute syringe pumps for injecting samples into the plasma separators. Syringe pump is commonly used to fill the plasma separators with a sample [17-23]. Substituting it with a small scale disposable micropump is especially important when only limited amount of samples are available. The EWOD micropump could be easily integrated with the reported blood plasma separators in literature. The separators based on the Zweifach–Fung effect [17-19], geometric singularities [20], or large output channel [21, 22], indicate the modular integration with the proposed pump is possible.

Thermocapillary is also used for manipulating floating droplets of biochemical samples on a liquid substrate for chemical reactions. In this way the temperature gradient induced in the base medium could be used to drive floating aqueous droplets formed on the free surface of immiscible liquids for application in digital microfluidic devices[49], as well as material transportation and mixing in lab on a chip [50, 51]. Thus the floating aqueous droplets studied in this work, could serve as containers for encapsulating reagents in biochemical reactions [52]. These micro chemical reactors have the desired features of low consumption of the analytes, direct access to reaction products [52], and reduced contamination as compared to the droplets on solid surfaces. The floating droplets could also be used in sensor application due to direct contact with the ambient air [53].

The general solution obtained in this work, by taking advantage of non-dimension groups of parameters does not depend on the values of the fluids properties such as density and surface tension or the droplet size and thus could be applied to different experimental setups. The data could be used as a guideline to select a combination of three fluids to form different sizes of floating droplets for droplet manipulation.

APPENDIX A: EWOD MICROPUMP FABRICATION

This appendix contains the detailed process steps for the fabrication of EWOD-based micropump. The device was fabricated in a cleanroom class 1000.

EWOD substrate

1. A 3 inch <100> silicon wafer single side polished was cut in four parts using a diamond cutter on the direction of the crystal.
2. A quarter of the silicon wafer was rinsed with acetone, then methanol, and finally with isopropyl alcohol.
3. The wafer was dried using a nitrogen gun and examined under the microscope to make sure the small fragments of silicon that might have been remained on the wafer after it was cut are removed.
4. Make an uncured polydimethylsiloxane (PDMS) mixture with a weight ratio of 10:1, by mixing 2 grams of SYLGARD® 184 SILICONE ELASTOMER base with 0.2 grams of its curing agent in a petri dish for several minutes to form a uniform mixture. The curing agent solidifies the PDMS which is a viscous liquid at room temperature. Special attention should be given to the corners of the petri dish, since they will remain liquid after PDMS is cured if the base part was not thoroughly mixed with curing agent.
5. Air bubbles are formed in the PDMS mixture while stirring.
6. Toluene which is a good solvent for PDMS is used to dilute PDMS with a volumetric ratio of 3:1 in a small glass beaker. Later toluene could be used again to clean the beaker.

7. A spin-coater with a maximum spin rate of 6000 RPM was used for spin coating the diluted PDMS on the quarter wafer. The spin-coater chamber is covered with aluminum foil to avoid contamination of its wall with PDMS (Cleaning PDMS off the spin-coater could be cumbersome!)

8. The spin-coater is programmed for 6000RPM for 10 minutes.

9. The optional step of two minutes baking on hot plate at 200^{o}C is used to completely remove water from the wafer.

10. The quarter wafer is placed on the stage of a spin coater after it is cooled down and it's centered on the stage to have a relatively balanced rotation.

11. The vacuum is turned on to hold the quarter wafer in its place.

12. The Diluted PDMS is poured on the wafer and the spin-coating is run.

13. The sample is placed on the hot plate for baking at 90C for 10 minutes.

14. The sample is placed on the spin-coater after it's cooled down.

15. Spin-on glass (SOG) is coated on the sample at 3000 RPM for 40 seconds.

16. Sample is baked on hotplate at 200^{o}C for 1 minute to remove the solvents from SOG.

17. Repeat steps 10 to 13 to form a second PDMS thin film.

SU-8 2050 mold fabrication

18. A 3 inch <100> silicon wafer single side polished was rinsed with acetone, then methanol, and finally with isopropyl alcohol (IPA).

19. The wafer was dried using a nitrogen gun

20. Five minutes baking on hot plate at 200^{o}C is used to dehydrate the wafer surface.

21. Cover the spin-coater chamber with aluminum foil before spin coating.

22. Center the silicon wafer on spin-coater stage and turn on the vacuum.

23. Pure small amount of SU-8 2050 photoresist on the center of the wafer. 1 mL of resist per inch of wafer diameter.

24. Run a two-step spin-coating:

500RPM for 13 seconds with an 85 rpm/sec ramp (Resist spreading)

1500RPM for 41 seconds with a ramp of 340 rpm/sec (Resist coating)

The resist thickness will be 100μm based on the manufacturer data sheet.

25. Remove the SU_8 resist from the edge of the wafer using a sharp blade (Edge bead removal).

26. Two step soft baking the resist on hot plate:

T=65^{o}C for 25 minutes

T=95^{o}C for 35 minutes

Cool down 20 minutes.

27. UV exposure for 40 seconds.

28. Post exposure bake:

T=65^{o}C for 1 minutes

T=95^{o}C for 35 minutes

29. Using a Pyrex dish, develop the resist in Propylene Gycol Methylether Acetate, 99%, AIDRICH Co. until all the unexposed area is solved in developer (about 5

minutes). Use less agitation and longer developing time, to prevent overdeveloping of smaller features.

30. Rinse the wafer using IPA. Dry with nitrogen gun.

31. Hard bake the resist after developing:

T=70C for 5 minutes

T=100 for 5min

T=150 for 3min

Use different hot plates for the three-step baking, since hot plates will not reach to the desired temperature in a few minutes. Leave on hot plate to cool down.

PDMS casting

32. Repeat step 4 but use 20 grams of SYLGARD® 184 SILICONE ELASTOMER base with 2 grams of the curing agent.

33. Put the SU-8 mold on silicon wafer which was fabricated in steps 18 to 31 in a petri dish. Pour PDMS from step 32 on it.

34. Leave at room temperature for 30 minutes to remove the air bubbles. Examine under the microscope to check all the air bubbles have escaped from the uncured resin. If not, allow more time for air bubble removal before proceeding to next step.

35. Put the petri dish on the hot plate and bake for one hour at 95^{o}C.

36. Cut the PDMS using sharp surgical blade and peel it off the SU_8 mold. Punch inlets using a blunt needle gauge 21.

Bonding, fluidic interconnections and electrical contacts

37. Bond the PDMS slab with microchannel from step 35 to the EWOD substrate prepared in steps 1 to 17 using corona discharge method. Hold each bonding surfaces under the corona for 15 seconds. Put the bonding surfaces together and press the top PDMS layer on the bottom EWOD substrate using tweezers to remove any air bubbles between them.

38. Use hollow high precision stainless steel tubes and transparent highly flexible plastic tubes for microfluidic connections. Attach a wire to the steel tube and the silicon wafer of the EWOD substrate for electrical connections.

APPENDIX B: FORCE ANALYSIS EQUATIONS FOR CHAPTER 6

NC droplet configuration

$$F_G = \frac{4}{3}\pi g \rho_w R_D^3$$

$$F_{Sy} = 2\gamma_{oa}\pi R_D \sin {\varphi_D}^2$$

$$F_B = \rho_o g \left(-h\pi (R_D \sin \varphi_D)^2 + \pi R_D^3 \left(\frac{2}{3} - \frac{\cos \varphi_D}{3} (2 + \sin {\varphi_D}^2) \right) \right)$$

$$F_{net,y} = F_B - F_G + F_{Sy} = 0$$

C/B droplet configuration

$$A = \begin{bmatrix} \gamma_{wa} & \gamma_{ow} & 0 \\ \gamma_{oa} & 0 & \gamma_{ow} \\ 0 & \gamma_{oa} & \gamma_{wa} \end{bmatrix}$$

$$C = \begin{bmatrix} -\gamma_{oa} \\ -\gamma_{wa} \\ -\gamma_{ow} \end{bmatrix}$$

$$X = \begin{bmatrix} \theta_a \\ \theta_o \\ \theta_w \end{bmatrix} = inv(A) \times C$$

$$\varphi_{bead} = \pi - \sin^{-1}\left(\sin \varphi_{cap} \left(\frac{\gamma_{wa}}{\gamma_{ow}} \right) \right)$$

$$R_{cap} =$$

$$\left(V_D \Big/ \left(\pi \left(\left(\frac{2}{3} - \frac{\cos \varphi_{cap}}{3} \left(2 + \sin {\varphi_{cap}}^2 \right) \right) + \left(\frac{\gamma_{ow}}{\gamma_{wa}} \right)^3 \left(\frac{2}{3} - \frac{\cos \varphi_{bead}}{3} (2 + \sin {\varphi_{bead}}^2) \right) \right) \right) \right)^{1/3}$$

$$R_{bead} = R_{cap}\left(\frac{\gamma_{ow}}{\gamma_{wa}}\right)$$

$$F_G = g\varphi_w V_D$$

$$F_{Sy} = 2\pi\gamma_{oa}R_{cap}\sin\varphi_{cap}\sin\left(\theta_a + \varphi_{cap} - \pi\right)$$

$$F_B = \rho_o g\left(\pi R_{bead}^3\left(\frac{2}{3} - \frac{\cos\varphi_{bead}}{3}\left(2 + \sin{\varphi_{bead}}^2\right)\right) - h\pi\left(R_{bead}\sin\varphi_{bead}\right)^2\right)$$

$$F_{net,y} = F_B - F_G - F_{Sy}$$

APPENDIX C: ENERGY ANALYSIS EQUATIONS FOR CHAPTER 6

NC droplet configuration

- Surface energy:

$$E_S = \gamma_{oa}(A_{DS} - \pi 0.015^2)$$

,where area of the deformed free surface is:

$$A_{DS} = 2\pi R_D^2(1 - \cos\varphi_D) + \sum_{-h}^{0} \sum_{R_D \sin\varphi_D}^{15^{mm}} 2\pi r(dr^2 + dy^2)^{0.5}$$

It is assumed for r larger than 15mm the free surface deflection is negligible.

- Droplet's gravitational potential energy:

$$U_D = \frac{4}{3} g\rho_w \pi R_D^3 \left(h_{c,w} - R_D\right)$$

,where geometric centroid of the water droplet is:

$$h_{c,w} = R_D \cos\varphi_D + h$$

- Displaced base medium gravitational potential energy:

$$U_{DL} = \rho_f g V_{DL} h_{c,o}$$

,where volume of the displaced base medium is:

$$V_{DL} = V_{cap} + V_{ry} = \frac{\pi}{3} R_D^3 (2 - \cos\varphi_D (2 + \sin\varphi_D{}^2)) + \sum_{-h}^{0} \pi r^2 dy$$

And geometric centroid of the displaced base medium is:

$$h_{c,o} = \frac{h_{c,cap} V_{cap} + h_{c,ry} V_{ry}}{V_{DL}}$$

Where,

$$h_{c,cap} = \frac{(3R_D(1+\cos\varphi_D)^2)}{4(2+\cos\varphi_D)} - (R_D\cos\varphi_D + h)$$

$$h_{c,ry}V_{ry} = \sum_{-h}^{0} -y\pi r^2 dy$$

- The net energy of the NC droplet configuration is:

$$E_{net} = U_D + U_{DL} + E_S$$

C/B droplet configuration

- Surface energy:

$$E_S = \gamma_{oa}A_{DS} + \gamma_{wa}A_{cap} + \gamma_{wo}A_{bead} - (\gamma_{oa}\pi 0.015^2 + \gamma_{wo}A_D)$$

,where

$$A_{DS} = \sum_{h}^{0} \sum_{R_{cap}\sin\varphi_{cap}}^{15^{mm}} 2\pi r(dr^2 + dy^2)^{0.5}$$

$$A_D = 4\pi\left(\frac{3V_D}{4\pi}\right)^{2/3}$$

$$A_{cap} = 2\pi R_{cap}^2\left(1-\cos\varphi_{cap}\right)$$

$$A_{bead} = 2\pi R_{bead}^2(1-\cos\varphi_{bead})$$

- Droplet gravitational potential energy:

$$U_D = g\rho_w\left(V_{cap}h_{c,cap} - V_{bead}h_{c,bead}\right) - g\rho_w V_D(-R_D)$$

,where

$$V_{cap} = \frac{\pi}{3}R_{cap}^3\left(2 - \cos\varphi_{cap}\left(2 + \sin{\varphi_{cap}}^2\right)\right)$$

$$h_{c,cap} = \frac{\left(3R_{cap}\left(1 + \cos\varphi_{cap}\right)^2\right)}{4\left(2 + \cos\varphi_{cap}\right)} - \left(R_{cap}\cos\varphi_{cap} + h\right)$$

$$R_D = \left(\frac{3V_D}{4\pi}\right)^{1/3}$$

$$V_{bead} = \frac{\pi}{3}R_{bead}^3(2 - \cos\varphi_{bead}(2 + \sin{\varphi_{bead}}^2))$$

$$h_{c,bead} = \frac{(3R_{bead}(1 + \cos\varphi_{bead})^2)}{4(2 + \cos\varphi_{bead})} - (R_{bead}\cos\varphi_{bead} + h)$$

- Displaced base medium gravitational potential energy:

$$U_{DL} = \rho_o g V_{DS}h_{c,o} + (-\rho_o g)\left(V_{bead}\left(-h_{c,bead}\right) - V_{cyl}h_{c,cyl}\right) - (-\rho_o)gV_D(-R_D)$$

,where the volume of the base liquid below the deformed free surface, V_{DS} is:

$$V_{DS} = -(V_{bead} - V_{bead0}) + \sum_{h}^{0}\pi r^2 dy$$

,where V_{bead0} is:

$$V_{bead0} = \frac{\pi}{3}R_{bead}^3\left(2 - \cos\varphi_{bead0}\left(2 + \sin{\varphi_{bead0}}^2\right)\right)$$

φ_{bead0} is defined from the bottom point of the bead to y=0 and is equal to:

$$\varphi_{bead0} = \cos^{-1}\left(\frac{R_{bead}\cos\varphi_{bead} + h}{R_{bead}}\right)$$

The geometric centroid of the displaced base medium is derived as below:

$$h_{c,o} = \frac{h_{c,DS}V_{DS} - \left(-h_{c,bead}V_{bead} - \left(-h_{c,bead0}\right)V_{bead0}\right)}{V_{DS}}$$

$$h_{c,DS}V_{DS} = \sum_{h}^{0} y\pi r^2 dy$$

$$h_{c,bead0} = \frac{(3R_{bead}(1+\cos\varphi_{bead0})^2)}{4(2+\cos\varphi_{bead0})} - (R_{bead}\cos\varphi_{bead0})$$

$$V_{cyl} = \pi h(R_{bead}\sin\varphi_{bead})^2$$

$$h_{c,cyl} = \frac{h}{2}$$

- The net energy of the C/B droplet configuration is :

$$E_{net} = U_D + U_{DL} + E_S$$

APPENDIX D: COPYRIGHT PERMISSION LETTERS

A micropump controlled by EWOD: wetting line energy and velocity effects

R. Shabani and H. J. Cho, Lab Chip, 2011, 11, 3401

DOI: 10.1039/C1LC20440H

If you are the author of this article you do not need to formally request permission to reproduce figures, diagrams etc. contained in this article in third party publications or in a thesis or dissertation provided that the correct acknowledgement is given with the reproduced material.

Reproduced material should be attributed as follows:

For reproduction of material from NJC:

[Original citation] - Reproduced by permission of The Royal Society of Chemistry (RSC) on behalf of the Centre National de la Recherche Scientifique (CNRS) and the RSC

For reproduction of material from PCCP:

[Original citation] - Reproduced by permission of the PCCP Owner Societies

For reproduction of material from PPS:

[Original citation] - Reproduced by permission of The Royal Society of Chemistry (RSC) on behalf of the European Society for Photobiology, the European Photochemistry Association, and RSC

For reproduction of material from all other RSC journals:

[Original citation] - Reproduced by permission of The Royal Society of Chemistry

If you are the author of this article you still need to obtain permission to reproduce the whole article in a third party publication with the exception of reproduction of the whole article in a thesis or dissertation.

ELSEVIER LICENSE
TERMS AND CONDITIONS

Jun 03, 2013

This is a License Agreement between Roxana shabani ("You") and Elsevier ("Elsevier") provided by Copyright Clearance Center ("CCC"). The license consists of your order details, the terms and conditions provided by Elsevier, and the payment terms and conditions.

All payments must be made in full to CCC. For payment instructions, please see information listed at the bottom of this form.

Supplier	Elsevier Limited The Boulevard,Langford Lane Kidlington,Oxford,OX5 1GB,UK
Registered Company Number	1982084
Customer name	Roxana shabani
Customer address	Univ. of Central Florida, Dept. of MMAE Orlando, FL 32816
License number	3161561480239
License date	Jun 03, 2013
Licensed content publisher	Elsevier
Licensed content publication	Sensors and Actuators B: Chemical
Licensed content title	Active surface tension driven micropump using droplet/meniscus pressure gradient
Licensed content author	Roxana Shabani,Hyoung J. Cho
Licensed content date	April 2013
Licensed content volume number	180
Licensed content issue number	
Number of pages	8
Start Page	114
End Page	121
Type of Use	reuse in a thesis/dissertation
Portion	full article
Format	both print and electronic
Are you the author of this Elsevier article?	Yes
Will you be translating?	No
Order reference number	

Title of your thesis/dissertation	THREE-PHASE CONTACT LINE PHENOMENA IN DROPLETS ON SOLID AND LIQUID SURFACES: ELECTROCAPILLARY, PINNING, WETTING LINE VELOCITY EFFECT, AND FREE LIQUID SURFACE DEFORMATION
Expected completion date	Aug 2013
Estimated size (number of pages)	130
Elsevier VAT number	GB 494 6272 12
Permissions price	0.00 USD
VAT/Local Sales Tax	0.0 USD / 0.0 GBP
Total	0.00 USD
Terms and Conditions	

INTRODUCTION

1. The publisher for this copyrighted material is Elsevier. By clicking "accept" in connection with completing this licensing transaction, you agree that the following terms and conditions apply to this transaction (along with the Billing and Payment terms and conditions established by Copyright Clearance Center, Inc. ("CCC"), at the time that you opened your Rightslink account and that are available at any time at http://myaccount.copyright.com).

GENERAL TERMS

2. Elsevier hereby grants you permission to reproduce the aforementioned material subject to the terms and conditions indicated.

3. Acknowledgement: If any part of the material to be used (for example, figures) has appeared in our publication with credit or acknowledgement to another source, permission must also be sought from that source. If such permission is not obtained then that material may not be included in your publication/copies. Suitable acknowledgement to the source must be made, either as a footnote or in a reference list at the end of your publication, as follows:

"Reprinted from Publication title, Vol /edition number, Author(s), Title of article / title of chapter, Pages No., Copyright (Year), with permission from Elsevier [OR APPLICABLE SOCIETY COPYRIGHT OWNER]." Also Lancet special credit - "Reprinted from The Lancet, Vol. number, Author(s), Title of article, Pages No., Copyright (Year), with permission from Elsevier."

4. Reproduction of this material is confined to the purpose and/or media for which permission is hereby given.

5. Altering/Modifying Material: Not Permitted. However figures and illustrations may be altered/adapted minimally to serve your work. Any other abbreviations, additions, deletions and/or any other alterations shall be made only with prior written authorization of Elsevier Ltd. (Please contact Elsevier at permissions@elsevier.com)

6. If the permission fee for the requested use of our material is waived in this instance, please be advised that your future requests for Elsevier materials may attract a fee.

7. Reservation of Rights: Publisher reserves all rights not specifically granted in the combination of (i) the license details provided by you and accepted in the course of this licensing transaction, (ii) these terms and conditions and (iii) CCC's Billing and Payment terms and conditions.

8. License Contingent Upon Payment: While you may exercise the rights licensed immediately upon issuance of the license at the end of the licensing process for the transaction, provided that you have disclosed complete and accurate details of your proposed use, no license is finally effective unless and until full payment is received from you (either by publisher or by CCC) as provided in CCC's Billing and Payment terms and conditions. If full payment is not received on a timely basis, then any license preliminarily granted shall be deemed automatically revoked and shall be void as if never granted. Further, in the event that you breach any of these terms and conditions or any of CCC's Billing and Payment terms and conditions, the license is automatically revoked and shall be void as if never granted. Use of materials as described in a revoked license, as well as any use of the materials beyond the scope of an unrevoked license, may constitute copyright infringement and publisher reserves the right to take any and all action to protect its copyright in the materials.

9. Warranties: Publisher makes no representations or warranties with respect to the licensed material.

10. Indemnity: You hereby indemnify and agree to hold harmless publisher and CCC, and their respective officers, directors, employees and agents, from and against any and all claims arising out of your use of the licensed material other than as specifically authorized pursuant to this license.

11. No Transfer of License: This license is personal to you and may not be sublicensed, assigned, or transferred by you to any other person without publisher's written permission.

12. No Amendment Except in Writing: This license may not be amended except in a writing signed by both parties (or, in the case of publisher, by CCC on publisher's behalf).

13. Objection to Contrary Terms: Publisher hereby objects to any terms contained in any purchase order, acknowledgment, check endorsement or other writing prepared by you, which terms are inconsistent with these terms and conditions or CCC's Billing and Payment terms and conditions. These terms and conditions, together with CCC's Billing and Payment terms and conditions (which are incorporated herein), comprise the entire agreement between you and publisher (and CCC) concerning this licensing transaction. In the event of any conflict between your obligations established by these terms and conditions and those established by CCC's Billing and Payment terms and conditions, these terms and conditions shall control.

14. Revocation: Elsevier or Copyright Clearance Center may deny the permissions described in this License at their sole discretion, for any reason or no reason, with a full refund payable to you. Notice of such denial will be made using the contact information provided by you. Failure to receive such notice will not alter or invalidate the denial. In no event will Elsevier or Copyright Clearance Center be responsible or liable for any costs, expenses or damage incurred by you as a result of a denial of your permission request, other than a refund of the amount(s) paid by you to Elsevier and/or Copyright Clearance Center for denied permissions.

LIMITED LICENSE

The following terms and conditions apply only to specific license types:

15. **Translation**: This permission is granted for non-exclusive world **English** rights only unless your license was granted for translation rights. If you licensed translation rights you may only translate this content into the languages you requested. A professional translator must perform all translations and reproduce the content word for word preserving the integrity of the article. If this license is to re-use 1 or 2 figures then permission is granted for non-exclusive world rights in all languages.

16. **Website**: The following terms and conditions apply to electronic reserve and author websites:
Electronic reserve: If licensed material is to be posted to website, the web site is to be password-protected and made available only to bona fide students registered on a relevant course if:
This license was made in connection with a course,
This permission is granted for 1 year only. You may obtain a license for future website posting,
All content posted to the web site must maintain the copyright information line on the bottom of each image,
A hyper-text must be included to the Homepage of the journal from which you are licensing at http://www.sciencedirect.com/science/journal/xxxxx or the Elsevier homepage for books at http://www.elsevier.com , and
Central Storage: This license does not include permission for a scanned version of the material to be stored in a central repository such as that provided by Heron/XanEdu.

17. **Author website** for journals with the following additional clauses:

All content posted to the web site must maintain the copyright information line on the bottom of each image, and the permission granted is limited to the personal version of your paper. You are not allowed to download and post the published electronic version of your article (whether PDF or HTML, proof or final version), nor may you scan the printed edition to create an electronic version.
A hyper-text must be included to the Homepage of the journal from which you are licensing at http://www.sciencedirect.com/science/journal/xxxxx . As part of our normal production process, you will receive an e-mail notice when your article appears on Elsevier's online service ScienceDirect (www.sciencedirect.com). That e-mail will include the article's Digital Object Identifier (DOI). This number provides the electronic link to the published article and should be included in the posting of your personal version. We ask that you wait until you receive this e-mail and have the DOI to do any posting.

Central Storage: This license does not include permission for a scanned version of the material to be stored in a central repository such as that provided by Heron/XanEdu.

18. **Author website** for books with the following additional clauses:
Authors are permitted to place a brief summary of their work online only.
A hyper-text must be included to the Elsevier homepage at http://www.elsevier.com . All content posted to the web site must maintain the copyright information line on the bottom of each image.
You are not allowed to download and post the published electronic version of your chapter, nor may you scan the printed edition to create an electronic version.

Central Storage: This license does not include permission for a scanned version of the material to be stored in a central repository such as that provided by Heron/XanEdu.

19. **Website** (regular and for author): A hyper-text must be included to the Homepage of the journal from which you are licensing at http://www.sciencedirect.com/science/journal/xxxxx. or for books to the Elsevier homepage at http://www.elsevier.com

20. **Thesis/Dissertation**: If your license is for use in a thesis/dissertation your thesis may be submitted to your institution in either print or electronic form. Should your thesis be published commercially, please reapply for permission. These requirements include permission for the Library and Archives of Canada to supply single copies, on demand, of the complete thesis and include permission for UMI to supply single copies, on demand, of the complete thesis. Should your thesis be published commercially, please reapply for permission.

21. **Other Conditions**:

v1.6

If you would like to pay for this license now, please remit this license along with your payment made payable to "COPYRIGHT CLEARANCE CENTER" otherwise you will be invoiced within 48 hours of the license date. Payment should be in the form of a check or money order referencing your account number and this invoice number RLNK501035136. Once you receive your invoice for this order, you may pay your invoice by credit card. Please follow instructions provided at that time.

Make Payment To:
Copyright Clearance Center
Dept 001
P.O. Box 843006
Boston, MA 02284-3006

For suggestions or comments regarding this order, contact RightsLink Customer Support: customercare@copyright.com or +1-877-622-5543 (toll free in the US) or +1-978-646-2777.

Gratis licenses (referencing $0 in the Total field) are free. Please retain this printable license for your reference. No payment is required.

SPRINGER LICENSE
TERMS AND CONDITIONS

Jun 03, 2013

This is a License Agreement between Roxana shabani ("You") and Springer ("Springer") provided by Copyright Clearance Center ("CCC"). The license consists of your order details, the terms and conditions provided by Springer, and the payment terms and conditions.

All payments must be made in full to CCC. For payment instructions, please see information listed at the bottom of this form.

License Number	3161570306758
License date	Jun 03, 2013
Licensed content publisher	Springer
Licensed content publication	Microfluids and Nanofluids
Licensed content title	Flow rate analysis of an EWOD-based device: how important are wetting-line pinning and velocity effects?
Licensed content author	Roxana Shabani
Licensed content date	Jan 1, 2013
Type of Use	Thesis/Dissertation
Portion	Full text
Number of copies	1
Author of this Springer article	Yes and you are the sole author of the new work
Order reference number	
Title of your thesis / dissertation	THREE-PHASE CONTACT LINE PHENOMENA IN DROPLETS ON SOLID AND LIQUID SURFACES: ELECTROCAPILLARY, PINNING, WETTING LINE VELOCITY EFFECT, AND FREE LIQUID SURFACE DEFORMATION
Expected completion date	Aug 2013
Estimated size(pages)	130
Total	0.00 USD
Terms and Conditions	

Introduction

The publisher for this copyrighted material is Springer Science + Business Media. By clicking "accept" in connection with completing this licensing transaction, you agree that the following terms and conditions apply to this transaction (along with the Billing and Payment terms and conditions established by Copyright Clearance Center, Inc. ("CCC"), at the time that you opened your Rightslink account and that are available at any time at http://myaccount.copyright.com).

Limited License

With reference to your request to reprint in your thesis material on which Springer Science and Business Media control the copyright, permission is granted, free of charge, for the use indicated in your enquiry.

Licenses are for one-time use only with a maximum distribution equal to the number that you identified in the licensing process.

This License includes use in an electronic form, provided its password protected or on the university's intranet or repository, including UMI (according to the definition at the Sherpa website: http://www.sherpa.ac.uk/romeo/). For any other electronic use, please contact Springer at (permissions.dordrecht@springer.com or permissions.heidelberg@springer.com).

The material can only be used for the purpose of defending your thesis, and with a maximum of 100 extra copies in paper.

Although Springer holds copyright to the material and is entitled to negotiate on rights, this license is only valid, subject to a courtesy information to the author (address is given with the article/chapter) and provided it concerns original material which does not carry references to other sources (if material in question appears with credit to another source, authorization from that source is required as well).

Permission free of charge on this occasion does not prejudice any rights we might have to charge for reproduction of our copyrighted material in the future.

Altering/Modifying Material: Not Permitted

You may not alter or modify the material in any manner. Abbreviations, additions, deletions and/or any other alterations shall be made only with prior written authorization of the author(s) and/or Springer Science + Business Media. (Please contact Springer at (permissions.dordrecht@springer.com or permissions.heidelberg@springer.com)

Reservation of Rights

Springer Science + Business Media reserves all rights not specifically granted in the combination of (i) the license details provided by you and accepted in the course of this licensing transaction, (ii) these terms and conditions and (iii) CCC's Billing and Payment terms and conditions.

Copyright Notice:Disclaimer

You must include the following copyright and permission notice in connection with any reproduction of the licensed material: "Springer and the original publisher /journal title, volume, year of publication, page, chapter/article title, name(s) of author(s), figure number(s), original copyright notice) is given to the publication in which the material was originally published, by adding; with kind permission from Springer Science and Business Media"

Warranties: None

Example 1: Springer Science + Business Media makes no representations or warranties with respect to the licensed material.

Example 2: Springer Science + Business Media makes no representations or warranties with respect to the licensed material and adopts on its own behalf the limitations and disclaimers established by CCC on its behalf in its Billing and Payment terms and conditions for this licensing transaction.

Indemnity
You hereby indemnify and agree to hold harmless Springer Science + Business Media and CCC, and their respective officers, directors, employees and agents, from and against any and all claims arising out of your use of the licensed material other than as specifically authorized pursuant to this license.

No Transfer of License
This license is personal to you and may not be sublicensed, assigned, or transferred by you to any other person without Springer Science + Business Media's written permission.

No Amendment Except in Writing
This license may not be amended except in a writing signed by both parties (or, in the case of Springer Science + Business Media, by CCC on Springer Science + Business Media's behalf).

Objection to Contrary Terms
Springer Science + Business Media hereby objects to any terms contained in any purchase order, acknowledgment, check endorsement or other writing prepared by you, which terms are inconsistent with these terms and conditions or CCC's Billing and Payment terms and conditions. These terms and conditions, together with CCC's Billing and Payment terms and conditions (which are incorporated herein), comprise the entire agreement between you and Springer Science + Business Media (and CCC) concerning this licensing transaction. In the event of any conflict between your obligations established by these terms and conditions and those established by CCC's Billing and Payment terms and conditions, these terms and conditions shall control.

Jurisdiction
All disputes that may arise in connection with this present License, or the breach thereof, shall be settled exclusively by arbitration, to be held in The Netherlands, in accordance with Dutch law, and to be conducted under the Rules of the 'Netherlands Arbitrage Instituut' (Netherlands Institute of Arbitration).***OR:***

All disputes that may arise in connection with this present License, or the breach thereof, shall be settled exclusively by arbitration, to be held in the Federal Republic of Germany, in accordance with German law.

Other terms and conditions:

v1.3

If you would like to pay for this license now, please remit this license along with your payment made payable to "COPYRIGHT CLEARANCE CENTER" otherwise you will be invoiced within 48 hours of the license date. Payment should be in the form of a check or money order referencing your account number and this invoice number RLNK501035141. Once you receive your invoice for this order, you may pay your invoice by credit card. Please follow instructions provided at that time.

Make Payment To:
Copyright Clearance Center
Dept 001
P.O. Box 843006
Boston, MA 02284-3006

For suggestions or comments regarding this order, contact RightsLink Customer Support: customercare@copyright.com or +1-877-622-5543 (toll free in the US) or +1-978-646-2777.

Gratis licenses (referencing $0 in the Total field) are free. Please retain this printable license for your reference. No payment is required.

AMERICAN INSTITUTE OF PHYSICS LICENSE TERMS AND CONDITIONS

Jun 03, 2013

All payments must be made in full to CCC. For payment instructions, please see information listed at the bottom of this form.

License Number	3161570645893
Order Date	Jun 03, 2013
Publisher	American Institute of Physics
Publication	Applied Physics Letters
Article Title	Droplets on liquid surfaces: Dual equilibrium states and their energy barrier
Author	Roxana Shabani, Ranganathan Kumar, Hyoung J. Cho
Online Publication Date	May 7, 2013
Volume number	102
Issue number	18
Type of Use	Thesis/Dissertation
Requestor type	Author (original article)
Format	Print and electronic
Portion	Excerpt (> 800 words)
Will you be translating?	No
Title of your thesis / dissertation	THREE-PHASE CONTACT LINE PHENOMENA IN DROPLETS ON SOLID AND LIQUID SURFACES: ELECTROCAPILLARY, PINNING, WETTING LINE VELOCITY EFFECT, AND FREE LIQUID SURFACE DEFORMATION
Expected completion date	Aug 2013
Estimated size (number of pages)	130
Total	0.00 USD

Terms and Conditions

American Institute of Physics -- Terms and Conditions: Permissions Uses

American Institute of Physics ("AIP") hereby grants to you the non-exclusive right and license to use and/or distribute the Material according to the use specified in your order, on a one-time basis, for the specified term, with a maximum distribution equal to the number that you have ordered. Any links or other content accompanying the Material are not the subject of this license.

1. You agree to include the following copyright and permission notice with the reproduction of the Material: "Reprinted with permission from [FULL CITATION]. Copyright [PUBLICATION YEAR], American Institute of Physics." For an article, the copyright and permission notice must be printed on the first page of the article or book chapter. For photographs, covers, or tables, the copyright and permission notice may appear with the Material, in a footnote, or in the reference list.
2. If you have licensed reuse of a figure, photograph, cover, or table, it is your responsibility to ensure that the material is original to AIP and does not contain the copyright of another entity, and that the copyright notice of the figure, photograph, cover, or table does not

indicate that it was reprinted by AIP, with permission, from another source. Under no circumstances does AIP, purport or intend to grant permission to reuse material to which it does not hold copyright.

3. You may not alter or modify the Material in any manner. You may translate the Material into another language only if you have licensed translation rights. You may not use the Material for promotional purposes. AIP reserves all rights not specifically granted herein.
4. The foregoing license shall not take effect unless and until AIP or its agent, Copyright Clearance Center, receives the Payment in accordance with Copyright Clearance Center Billing and Payment Terms and Conditions, which are incorporated herein by reference.
5. AIP or the Copyright Clearance Center may, within two business days of granting this license, revoke the license for any reason whatsoever, with a full refund payable to you. Should you violate the terms of this license at any time, AIP, American Institute of Physics, or Copyright Clearance Center may revoke the license with no refund to you. Notice of such revocation will be made using the contact information provided by you. Failure to receive such notice will not nullify the revocation.
6. AIP makes no representations or warranties with respect to the Material. You agree to indemnify and hold harmless AIP, American Institute of Physics, and their officers, directors, employees or agents from and against any and all claims arising out of your use of the Material other than as specifically authorized herein.
7. The permission granted herein is personal to you and is not transferable or assignable without the prior written permission of AIP. This license may not be amended except in a writing signed by the party to be charged.
8. If purchase orders, acknowledgments or check endorsements are issued on any forms containing terms and conditions which are inconsistent with these provisions, such inconsistent terms and conditions shall be of no force and effect. This document, including the CCC Billing and Payment Terms and Conditions, shall be the entire agreement between the parties relating to the subject matter hereof.

This Agreement shall be governed by and construed in accordance with the laws of the State of New York. Both parties hereby submit to the jurisdiction of the courts of New York County for purposes of resolving any disputes that may arise hereunder.

If you would like to pay for this license now, please remit this license along with your payment made payable to "COPYRIGHT CLEARANCE CENTER" otherwise you will be invoiced within 48 hours of the license date. Payment should be in the form of a check or money order referencing your account number and this invoice number RLNK501035144. Once you receive your invoice for this order, you may pay your invoice by credit card. Please follow instructions provided at that time.

Make Payment To:
Copyright Clearance Center
Dept 001
P.O. Box 843006
Boston, MA 02284-3006

For suggestions or comments regarding this order, contact RightsLink Customer Support: customercare@copyright.com or +1-877-622-5543 (toll free in the US) or +1-978-646-2777.

Gratis licenses (referencing $0 in the Total field) are free. Please retain this printable

license for your reference. No payment is required.

REFERENCES

[1] K. W. Oh and C. H. Ahn, "A review of microvalves," *J. Micromech. Microeng. ,* vol. 16, pp. R13-R39, 2006.

[2] D. J. Laser and J. G. Santiago, "A review of micropumps," *J. Micromech. Microeng. ,* vol. 14, pp. R35-R64, 2004.

[3] B. Iverson and S. Garimella, "Recent advances in microscale pumping technologies: a review and evaluation," *Microfluidics and Nanofluidics,* vol. 5, pp. 145-174, 2008.

[4] A. Nisar, N. Afzulpurkar, B. Mahaisavariya, and A. Tuantranont, "MEMS-based micropumps in drug delivery and biomedical applications," *Sensors and Actuators B: Chemical,* vol. 130, pp. 917-942, 2008.

[5] F. Amirouche, Y. Zhou, and T. Johnson, "Current micropump technologies and their biomedical applications," *Microsystem Technologies,* vol. 15, pp. 647-666, 2009.

[6] N. C. Tsai and C. Y. Sue, "Review of MEMS-based drug delivery and dosing systems," *Sensors and Actuators A: Physical* vol. 134, pp. 555-564, Mar 15 2007.

[7] J. K. Luo, Y. Q. Fu, Y. Li, X. Y. Du, A. J. Flewitt, A. J. Walton*, et al.*, "Moving-part-free microfluidic systems for lab-on-a-chip," *JOURNAL OF MICROMECHANICS AND MICROENGINEERING,* vol. 19, p. 054001, 2009.

[8] S. Y. Xing, R. S. Harake, and T. R. Pan, "Droplet-driven transports on superhydrophobic-patterned surface microfluidics," *Lab on a Chip,* vol. 11, pp. 3642-3648, 2011.

[9] E. Berthier and D. J. Beebe, "Flow rate analysis of a surface tension driven passive micropump," *Lab on a Chip,* vol. 7, pp. 1475-1478, 2007.

[10] J. Lee and C. J. Kim, "Surface-tension-driven microactuation based on continuous electrowetting," *JOURNAL OF MICROELECTROMECHANICAL SYSTEMS,* vol. 9, pp. 171-180, Jun 2000.

[11] S. K. Cho, H. Moon, and C.-J. Kim, "Creating, Transporting, Cutting, and Merging Liquid Droplets by Electrowetting-Based Actuation for Digital Microfluidic Circuits," *JOURNAL OF MICROELECTROMECHANICAL SYSTEMS,* vol. 12, pp. 70-80, 2003.

[12] H. Ren, R. B. Fair, M. G. Pollack, and E. J. Shaughnessy, "Dynamics of electro-wetting droplet transport," *Sensors and Actuators B: Chemical,* vol. 87, pp. 201-206, Nov 15 2002.

[13] H. Ren, R. B. Fair, and M. G. Pollack, "Automated on-chip droplet dispensing with volume control by electro-wetting actuation and capacitance metering," *Sensors and Actuators B: Chemical,* vol. 98, pp. 319-327, Mar 15 2004.

[14] J. Lee, H. Moon, J. Fowler, T. Schoellhammer, and C.-J. Kim, "Electrowetting and electrowetting-on-dielectric for microscale liquid handling," *Sensors and Actuators A: Physical,* vol. 95, pp. 259-268, 2002.

[15] T. Pan, S. J. McDonald, E. M. Kai, and B. Ziaie, "A magnetically driven PDMS micropump with ball check-valves," *J. Micromech. Microeng. ,* vol. 15, pp. 1021-1026, 2005.

[16] K.-S. Yun, I.-J. Cho, J.-U. Bu, G.-H. Kim, Y.-S. Jeon, C.-J. Kim*, et al.*, "A micropump driven by continuous electrowetting actuation for low voltage and low power operations," in *Micro Electro Mechanical Systems, 2001. MEMS 2001. The 14th IEEE International Conference on*, 2001, pp. 487-490.

[17] Z. Fekete, P. Nagy, G. Huszka, F. Tolner, A. Pongrácz, and P. Fürjes, "Performance characterization of micromachined particle separation system based on Zweifach–Fung effect," *Sensors and Actuators B: Chemical,* vol. 162, pp. 89-94, 2012.

[18] M. Kersaudy-Kerhoas, R. Dhariwal, M. P. Y. Desmulliez, and L. Jouvet, "Hydrodynamic blood plasma separation in microfluidic channels," *Microfluidics and Nanofluidics,* vol. 8, pp. 105-114, Jan 2010.

[19] S. Yang, A. Undar, and J. D. Zahn, "A microfluidic device for continuous, real time blood plasma separation," *Lab on a Chip,* vol. 6, pp. 871-880, 2006.

[20] E. Sollier, M. Cubizolles, Y. Fouillet, and J. L. Achard, "Fast and continuous plasma extraction from whole human blood based on expanding cell-free layer devices," *Biomedical Microdevices,* vol. 12, pp. 485-497, Jun 2010.

[21] A. I. Rodriguez-Villarreal, M. Arundell, M. Carmona, and J. Samitier, "High flow rate microfluidic device for blood plasma separation using a range of temperatures," *Lab on a Chip,* vol. 10, pp. 211-219, 2010.

[22] M. Kersaudy-Kerhoas, D. M. Kavanagh, R. S. Dhariwal, C. J. Campbell, and M. P. Y. Desmulliez, "Validation of a blood plasma separation system by biomarker detection," *Lab on a Chip,* vol. 10, pp. 1587-1595, 2010.

[23] A. Lenshof, A. Ahmad-Tajudin, K. Jaras, A. M. Sward-Nilsson, L. Aberg, G. Marko-Varga*, et al.*, "Acoustic Whole Blood Plasmapheresis Chip for Prostate Specific Antigen Microarray Diagnostics," *Analytical Chemistry,* vol. 81, pp. 6030-6037, Aug 1 2009.

[24] T. Young, "An Essay on the Cohesion of Fluids," *Philosophical Transactions of the Royal Society of London,* vol. 95, pp. 65-87, 1805.

[25] R. Baviere, J. Boutet, and Y. Fouillet, "Dynamics of droplet transport induced by electrowetting actuation," *Microfluidics and Nanofluidics,* vol. 4, pp. 287-294, Apr 2008.

[26] R. Tadmor, "Line Energy and the Relation between Advancing, Receding, and Young Contact Angles," *Langmuir,* vol. 20, pp. 7659-7664, 2004.

[27] E. B. Dussan V., "On the Spreading of Liquids on Solid Surfaces: Static and Dynamic Contact Lines," *Annual Review of Fluid Mechanics,* vol. 11, pp. 371-400, 1979.

[28] W. C. Nelson, P. Sen, and C.-J. C. Kim, "Dynamic Contact Angles and Hysteresis under Electrowetting-on-Dielectric," *Langmuir,* vol. 27, pp. 10319-10326, 2011.

[29] S. W. Walker, B. Shapiro, and R. H. Nochetto, "Electrowetting with contact line pinning: Computational modeling and comparisons with experiments," *PHYSICS OF FLUIDS,* vol. 21, p. 102103, 2009.

[30] Y. D. Shikhmurzaev, "Singularities at the moving contact line. Mathematical, physical and computational aspects," *Physica D: Nonlinear Phenomena,* vol. 217, pp. 121-133, 2006.

[31] T. D. Blake and J. De Coninck, "The influence of solid–liquid interactions on dynamic wetting," *Advances in Colloid and Interface Science,* vol. 96, pp. 21-36, 2002.

[32] C. Huh and L. E. Scriven, "Hydrodynamic model of steady movement of a solid/liquid/fluid contact line," *Journal of Colloid and Interface Science,* vol. 35, pp. 85-101, 1971.

[33] L. H. Tanner, "The spreading of silicone oil drops on horizontal surfaces," *Journal of Physics D: Applied Physics,* vol. 12, pp. 1473-1484, 1979.

[34] A. Quinn, R. Sedev, and J. Ralston, "Contact Angle Saturation in Electrowetting," *The Journal of Physical Chemistry B,* vol. 109, pp. 6268-6275, 2005.

[35] F. Mugele and J. C. Baret, "Electrowetting: From basics to applications," *Journal of Physics-Condensed Matter,* vol. 17, pp. R705-R774, Jul 20 2005.

[36] J. Zeng and T. Korsmeyer, "Principles of droplet electrohydrodynamics for lab-on-a-chip," *Lab an a Chip,* vol. 4, pp. 265-277, 2004.

[37] H.-W. Lu, K. Glasner, A. L. Bertozzi, and C.-J. Kim, "A diffuse-interface model for electrowetting drops in a Hele-Shaw cell," *Journal of Fluid Mechanics,* vol. 590, pp. 411-435, Nov 10 2007.

[38] J. Lienemann, A. Greiner, and J. G. Korvink, "Modeling, simulation, and optimization of electrowetting," *IEEE Transactions on Computer-Aided Design of Integrated Circuits and Systems,* vol. 25, pp. 234-247, Feb 2006.

[39] S. W. Walker and B. Shapiro, "Modeling the Fluid Dynamics of Electrowetting on Dielectric (EWOD)," *JOURNAL OF MICROELECTROMECHANICAL SYSTEMS,* vol. 15, pp. 986-1000, 2006.

[40] L.-S. Jang, G.-H. Lin, Y.-L. Lin, C.-Y. Hsu, W.-H. Kan, and C.-H. Chen, "Simulation and experimentation of a microfluidic device based on electrowetting on dielectric," *Biomedical Microdevices,* vol. 9, pp. 777-786, 2007.

[41] A. Ahmadi, J. F. Holzman, H. Najjaran, and M. Hoorfar, "Electrohydrodynamic modeling of microdroplet transient dynamics in electrocapillary-based digital microfluidic devices," *Microfluidics and Nanofluidics,* vol. 10, pp. 1019-1032, 2010.

[42] V. Bahadur and S. V. Garimella, "An energy-based model for electrowetting-induced droplet actuation," *JOURNAL OF MICROMECHANICS AND MICROENGINEERING,* vol. 16, pp. 1494-1503, 2006.

[43] Z. Keshavarz-Motamed, L. Kadem, and A. Dolatabadi, "Effects of dynamic contact angle on numerical modeling of electrowetting in parallel plate microchannels," *Microfluidics and Nanofluidics,* vol. 8, pp. 47-56, 2009.

[44] J. H. Chen and W. H. Hsieh, "Electrowetting-induced capillary flow in a parallel-plate channel," *Journal of Colloid and Interface Science,* vol. 296, pp. 276-283, 2006.

[45] M. J. Schertzer, S. I. Gubarenko, R. Ben-Mrad, and P. E. Sullivan, "An Empirically Validated Analytical Model of Droplet Dynamics in Electrowetting on Dielectric Devices," *Langmuir,* vol. 26, pp. 19230-19238, Dec 21 2010.

[46] J. Berthier, P. Dubois, P. Clementz, P. Claustre, C. Peponnet, and Y. Fouillet, "Actuation potentials and capillary forces in electrowetting based microsystems," *Sensors and Actuators A: Physical* vol. 134, pp. 471-479, 2007.

[47] P. Sen and C. J. Kim, "Capillary Spreading Dynamics of Electrowetted Sessile Droplets in Air," *Langmuir,* vol. 25, pp. 4302-4305, Apr 21 2009.

[48] S. R. Annapragada, S. Dash, S. V. Garimella, and J. Y. Murthy, "Dynamics of Droplet Motion under Electrowetting Actuation," *Langmuir,* vol. 27, pp. 8198-8204, Jul 5 2011.

[49] E. F. Greco and R. O. Grigoriev, "Thermocapillary migration of interfacial droplets," *Physics of Fluids,* vol. 21, Apr 2009.

[50] E. Yakhshi-Tafti, H. J. Cho, and R. Kumar, "Droplet actuation on a liquid layer due to thermocapillary motion: Shape effect," *Applied Physics Letters,* vol. 96, Jun 28 2010.

[51] R. Savino, D. Paterna, and M. Lappa, "Marangoni flotation of liquid droplets," *J FLUID MECH,* vol. 479, pp. 307-326, 2003.

[52] A. S. Basu and Y. B. Gianchandani, "A Programmable Array for Contact-Free Manipulation of Floating Droplets on Featureless Substrates by the Modulation of Surface Tension," *Journal of Microelectromechanical Systems,* vol. 18, pp. 1163-1172, Dec 2009.

[53] A. A. Darhuber, J. P. Valentino, S. M. Troian, and S. Wagner, "Thermocapillary actuation of droplets on chemically patterned surfaces by programmable microheater arrays," *Journal of Microelectromechanical Systems,* vol. 12, pp. 873-879, Dec 2003.

[54] M. S. Khan, D. Kannangara, W. Shen, and G. Garnier, "Isothermal noncoalescence of liquid droplets at the air-liquid interface," *Langmuir,* vol. 24, pp. 3199-3204, Apr 1 2008.

[55] O. Reynolds, "On drops floating on the surface of water," *Chem. News,* vol. 44, p. 211, 1881.

[56] L. D. Mahajan, "Liquid Drops on the Same Liquid Surface," *Nature,* vol. 126, pp. 761-761, 1930.

[57] Y. Couder, E. Fort, C. H. Gautier, and A. Boudaoud, "From bouncing to floating: Noncoalescence of drops on a fluid bath," *Physical Review Letters,* vol. 94, May 6 2005.

[58] P. Aussillous and D. Quere, "Properties of liquid marbles," *Proceedings of the Royal Society a-Mathematical Physical and Engineering Sciences,* vol. 462, pp. 973-999, Mar 8 2006.

[59] E. Yakhshi-Tafti, H. J. Cho, and R. Kumar, "Impact of drops on the surface of immiscible liquids," *J COLLOID INTERF SCI,* vol. 350, pp. 373-376, Oct 1 2010.

[60] A. Elcrat, R. Neel, and D. Siegel, "Equilibrium Configurations for a Floating Drop," *J MATH FLUID MECH,* vol. 6, pp. 405-429, 2004.

[61] T. M. Squires and S. R. Quake, "Microfluidics: Fluid physics at the nanoliter scale," *REVIEWS OF MODERN PHYSICS,* vol. 77, p. 977, 2005.

[62] C. T. Leondes, K.-S. Yun, and E. Yoon, "Micropumps for MEMS/NEMS and Microfluidic Systems," in *MEMS/NEMS*, ed: Springer US, 2006, pp. 1112-1144.

[63] M. G. Pollack, A. D. Shenderov, and R. B. Fair, "Electrowetting-based actuation of droplets for integrated microfluidics," *Lab on a Chip,* vol. 2, pp. 96-101, 2002.

[64] J. S. Go and S. Shoji, "A disposable, dead volume-free and leak-free in-plane PDMS microvalve," *Sensors and Actuators A* vol. 114, pp. 438-444, 2004.

[65] J. H. Koschwanez, R. H. Carlson, and D. R. Meldrum, "Thin PDMS Films Using Long Spin Times or Tert-Butyl Alcohol as a Solvent," *PLoS ONE,* vol. 4, p. e4572, 2009.

[66] K. Haubert, T. Drier, and D. Beebe, "PDMS bonding by means of a portable, low-cost corona system," *Lab an a Chip,* vol. 6, pp. 1548-1549, 2006.

[67] H. Hillborg and U. W. Gedde, "Hydrophobicity recovery of polydimethylsiloxane after exposure to corona discharges," *Polymer,* vol. 39, pp. 1991-1998, May 1998.

[68] J. Kim and M. K. Chaudhury, "Corona-discharge-induced hydrophobicity loss and recovery of silicones," in *Electrical Insulation and Dielectric Phenomena, 1999 Annual Report Conference on*, 1999, pp. 703-706 vol.2.

[69] D. Brassard, L. Malic, F. Normandin, M. Tabrizian, and T. Veres, "Water-oil core-shell droplets for electrowetting-based digital microfluidic devices," *Lab an a Chip,* vol. 8, pp. 1342-1349, 2008.

[70] G. Lippmann, "Relation entre les phenomenes electriques et capillaires," *Ann. Chim. Phys. ,* vol. 5, pp. 494-549, 1875.

[71] R. Shabani and H. J. Cho, "A micropump controlled by EWOD: wetting line energy and velocity effects," *Lab on a Chip,* vol. 11, pp. 3401-3403, 2011.

[72] K. Hosokawa, T. Fujii, and I. Endo, "Droplet-based nano/picoliter mixer using hydrophobic microcapillary vent," in *Micro Electro Mechanical Systems, 1999. MEMS '99. Twelfth IEEE International Conference on*, 1999, pp. 388-393.

[73] M. J. Schertzer, S. I. Gubarenko, R. Ben Mrad, and P. E. Sullivan, "An empirically validated model of the pressure within a droplet confined between plates at equilibrium for low Bond numbers," *Experiments in Fluids,* vol. 48, pp. 851-862, 2009.

[74] R. G. Picknett and R. Bexon, "Evaporation of Sessile or Pendant Drops in Still Air," *Journal of Colloid and Interface Science,* vol. 61, pp. 336-350, 1977.

[75] K. S. Birdi and D. T. Vu, "Wettability and the Evaporation Rates of Fluids from Solid-Surfaces," *Journal of Adhesion Science and Technology,* vol. 7, pp. 485-493, 1993.

[76] G. McHale, S. M. Rowan, M. I. Newton, and M. K. Banerjee, "Evaporation and the Wetting of a Low-Energy Solid Surface," *The Journal of Physical Chemistry B,* vol. 102, pp. 1964-1967, 1998.

[77] H.-Z. Yu, D. M. Soolaman, A. W. Rowe, and J. T. Banks, "Evaporation of Water Microdroplets on Self-Assembled Monolayers: From Pinning to Shrinking," *ChemPhysChem,* vol. 5, pp. 1035-1038, 2004.

[78] T. D. Blake, "The physics of moving wetting lines," *Journal of Colloid and Interface Science,* vol. 299, pp. 1-13, 2006.

[79] F. Li and F. Mugele, "How to make sticky surfaces slippery: Contact angle hysteresis in electrowetting with alternating voltage," *Applied Physics Letters,* vol. 92, Jun 16 2008.

[80] R. Shabani and H. J. Cho, "Active surface tension driven micropump using droplet/meniscus pressure gradient," *Sensors and Actuators B: Chemical,* 2012.

[81] G. P. Neitzel and P. Dell'Aversana, "Noncoalescence and nonwetting behavior of liquids," *ANNU REV FLUID MECH,* vol. 34, pp. 267-289, 2002.

[82] O. W. Jayaratne and B. J. Mason, "The Coalescence and Bouncing of Water Drops at an Air/Water Interface," *P Roy Soc a-Math Phy,* vol. 280, pp. 545-565, 1964.

[83] G. E. Charles and S. G. Mason, "The mechanism of partial coalescence of liquid drops at liquid/liquid interfaces," *J COLL SCI IMP U TOK,* vol. 15, pp. 105-122, 1960.

[84] E. Honey and H. Kavehpour, "Astonishing life of a coalescing drop on a free surface," *PHYS REV E,* vol. 73, 2006.

[85] K. R. Sreenivas, P. K. De, and J. H. Arakeri, "Levitation of a drop over a film flow," *J FLUID MECH,* vol. 380, pp. 297-307, 1999.

[86] W. Fox, "Contact Angles at Liquid-Liquid-Air Interfaces," *J CHEM PHYS,* vol. 10, pp. 623-628, 1942.

[87] J. S. Rowlinson and B. Wisdom, *Molecular theory of capillarity*: oxford university press, 1982.

[88] C. Huh and L. E. Scriven, "Shapes of Axisymmetric Fluid Interfaces of Unbounded Extent," *J COLLOID INTERF SCI,* vol. 30, pp. 323-&, 1969.

[89] A. V. Rapacchietta and A. W. Neumann, "Force and Free-Energy Analyses of Small Particles at Fluid Interfaces .2. Spheres," *J COLLOID INTERF SCI,* vol. 59, pp. 555-567, 1977.

[90] A. V. Rapacchietta, A. W. Neumann, and S. N. Omenyi, "Force and Free-Energy Analyses of Small Particles at Fluid Interfaces .1. Cylinders," *J COLLOID INTERF SCI,* vol. 59, pp. 541-554, 1977.

LIST OF PUBLICATIONS

1- R. Shabani, R. Kumar, and H. J. Cho, “Droplets on liquid surfaces: dual equilibrium states and their energy barrier”, Applied physics Letters, 102, 184101, 20132013.

2- R. Shabani and H. J. Cho, “Flow rate analysis of an EWOD based device: how important are wetting line pinning and velocity effects?”, Microfluidics and Nanofluidics, 2013, DOI: 10.1007/s10404-013-1184-y.

3- R. Shabani and H.J. Cho, “Active surface tension driven micropump using droplet/meniscus pressure gradient”, Sensors and Actuators B: Chemical, 180, 114–121, 2013.

4- R. Shabani and H. J. Cho, “Nanomaterials in Actuators: A Review”, Reviews in Nanoscience and Nanotechnology, 1 (2), 85-102, 2012.

5- R. Shabani and H. J. Cho, “A micropump controlled by EWOD: wetting line energy and velocity effects”, Lab on a Chip 11 (20), 3401-3403, 2011.

6- S.-E. Zhu, R. Shabani, J. Rho, Y. Kim, B. H. Hong, J.-H. Ahn, and H. J. Cho, “Graphene-based bimorph microactuators”, Nano letters 11 (3), 977, 2011.

7- R. Shabani, L. Massi, L. Zhai, S. Seal, and H. J. Cho, “Classroom modules for nanotechnology undergraduate education: development, implementation and evaluation”, European Journal of Engineering Education, 36 (2), 199-210, 2011.